

Global Structures of Fluid Transport
in Perturbed Rayleigh-Bénard Convection

摂動を受けるレイリー・ベナール対流
における流体輸送の大域的構造

February, 2023

Masahito WATANABE
渡辺 昌仁

Global Structures of Fluid Transport in Perturbed Rayleigh-Bénard Convection

摂動を受けるレイリー・ベナール対流
における流体輸送の大域的構造

February, 2023

Waseda University
Graduate School of Fundamental Science and Engineering
Department of Applied Mechanics and Aerospace Engineering
Research on Applied Mathematics

Masahito WATANABE
渡辺 昌仁

Contents

1	Introduction	1
1.1	Background	1
1.2	Motivations of this study	8
1.3	Contributions and organization of this thesis	9
2	Structures of periodic orbits in a model	12
2.1	Model of perturbed Rayleigh-Bénard convection	12
2.2	Structures of periodic points	14
2.3	Structures of periodic orbits and KAM tori.	19
2.4	Resonances of periodic orbits	24
2.5	Symmetries of n/m -resonant orbits	29
2.6	Summary	34
3	Bifurcations of periodic orbits in a model	36
3.1	Structures of ε -parameter bifurcation	36
3.2	Numerical methods for detecting bifurcation points	41
3.3	Bifurcations associated with KAM island I_1	44
3.4	Bifurcations associated with KAM islands I_2, I_3, I_4	48
3.5	Bifurcations associated with other KAM islands	52
3.6	Summary	59
4	Experimental analysis on invariant structures	61
4.1	Dynamical systems theory	61
4.2	Experimental methods	64
4.3	Perturbations observed in velocity fields	65
4.4	Hyperbolic LCSs in experiments	69
4.5	Periodic points and elliptic LCSs in experiments	75
4.6	Summary	79
5	Perturbed Hamiltonian model for experiments	80
5.1	Model of perturbed Rayleigh-Bénard convection	80

5.2	Invariant structures in the model	89
5.3	Summary	95
6	Conclusions and future plans	96
6.1	Conclusions	96
6.2	Future plans	98
	References	99
	Acknowledgments	107
A	Model of Rayleigh-Bénard convection	108
A.1	Hamiltonian system of steady Rayleigh-Bénard convection . .	108
B	Experimental methods	114
B.1	Particle Image Velocimetry (PIV)	114

Chapter 1

Introduction

1.1 Background

Importance of studying fluid transport in Rayleigh-Benard convection. Clarifying the global structures and mechanisms of fluid transport is essential in many fields of science and engineering such as meteorology, oceanography, and chemical engineering, for instance, to understand the mechanisms of meteorological phenomena, or to predict and control the spread of chemical spills in the environment, or to mix high-viscosity liquid efficiently in a chemical reactor. In particular, analyzing the fluid transport in Rayleigh-Benard convection is important for two reasons. One is that this convection is typical natural convection that appears in a horizontal fluid layer with heated bottom and cooled top planes, as is shown in Fig.1.1.1. Especially, Rayleigh-Benard convection is known as a simple model of atmospheric circulation, since the ground or ocean on Earth is heated by sunlight and warm the atmosphere from below, as is illustrated in Fig.1.1.2. Thus, by analyzing fluid transport in Rayleigh-Benard convection we may be able to understand the mechanisms of meteorological phenomena such as typhoons and tornadoes or to predict and control the diffusion of air pollutant in the atmosphere. The other reason is that this convection can be modeled as a low-dimensional model, in particular

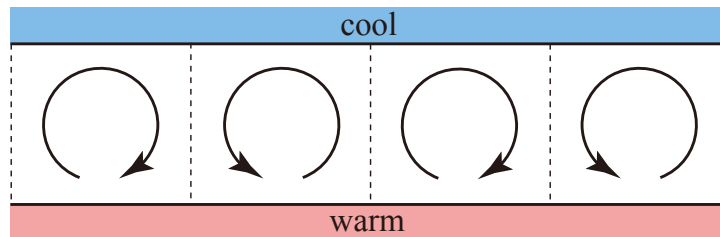


Figure 1.1.1: Two-dimensional Rayleigh-Bénard convection

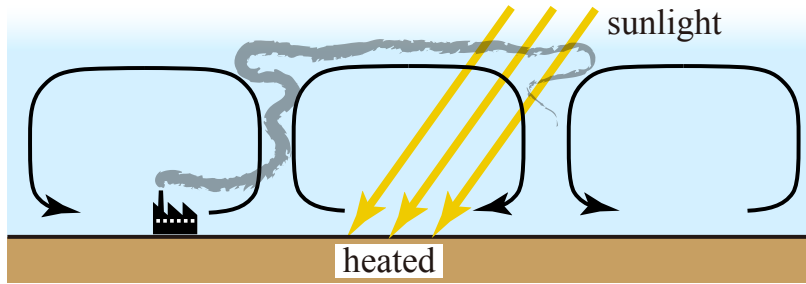


Figure 1.1.2: Atmospheric circulation

a perturbed Hamiltonian model. We can use dynamical systems theories to investigate the fluid transport in Rayleigh-Benard convection. This is crucial since fluid transport is a very complicated phenomenon.

Oscillatory instability of Rayleigh-Benard convection. The stability of Rayleigh-Benard convection is dominated by Rayleigh number Ra , which is proportional to the difference of the temperature of the bottom and top planes. When the temperature difference is relatively small, in other words, when Ra is relatively small, multiple convection rolls with steady velocity fields may appear in parallel in the layer. The flow can be considered as two-dimensional steady Rayleigh-Benard convection from the direction of roll axes, when the flow in that direction is negligible. On the other hand, it was clarified by Clever and Busse [12] and Bolton, Busse, and Clever [5] that parallel convection rolls may start to wave slightly by even oscillatory instability when Ra is set slightly above a critical number Ra_t by increasing the temperature difference. Since the wave propagates along the roll axes almost periodically, the flow may be considered as two-dimensional Rayleigh-Benard convection with perturbed velocity fields from the direction of roll axes. The amplitude of the oscillation enlarges when Ra is increased further by raising the temperature difference.

Chaotic fluid transport in perturbed Rayleigh-Bénard convection. One of the important remarks regarding such oscillatory convection is that some fluid particles may be transported chaotically in the Lagrangian description though the velocity fields seem to be stable in the Eulerian description; see Aref [1], Ottino [53], Wiggins and Ottino [77], and Grigoriev [23]. Fig.1.1.3 depicts the image of Poincaré section by Poincaré maps in the two-dimensional perturbed Hamiltonian model of Rayleigh-Benard convection, which was originally developed by Solomon and Gollub [63] and introduced by Camassa and

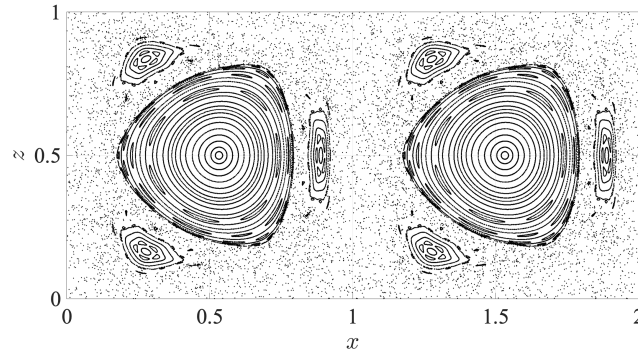


Figure 1.1.3: Poincaré section of the perturbed Hamiltonian model

Wiggins [8]; see §2.1 for details of the model. It is observed that not only KAM islands for stable fluid transport but also chaotic regions for chaotic transport appear in the convection. Many studies have been actively explored such rich dynamics in perturbed Rayleigh-Benard convection by theoretical, numerical, and experimental methods.

Previous works on fluid transport in perturbed Rayleigh-Benard convection. Among such past researches on the study of chaotic fluid transport in perturbed Rayleigh-Bénard convection, Solomon and Gollub [63] has been known as a pioneer work, where the diffusion of impurities was studied by optical absorption techniques and also where the convection was modeled as a two-dimensional perturbed Hamiltonian system following experimental results. It was clarified that fluid seems to be transported similarly as one-dimensional diffusion, where local effective diffusion constant grows linearly with the local amplitude of perturbation. In addition, it was numerically shown that the basic mechanism of fluid transport is chaotic advection around cell boundaries rather than molecular diffusion. Gollub and Solomon [22] also made some numerical analysis to show some evidence of chaotic transport in the perturbed Hamiltonian model in the sense of being sensitive to the initial condition. In addition, Ouchi et al. [55] numerically studied the diffusion constant of the model when the amplitude of perturbation is varied and Ouchi and Mori [54] indicated that some anomalous diffusion is caused by the accelerator-mode islands of KAM tori around cell boundaries at specific range of amplitude. Furthermore, Inoue and Hirata [35, 36] investigated the mixing patterns of another perturbed Hamiltonian model with different perturbations by analyzing Poincaré maps and the degree of mixing. In particular, Inoue and Hirata [36] showed how the chaotic structures vary when the amplitude or the frequency of the oscillation is changed and also detected some elliptic periodic points for one particular condition of parameters.

Some studies were made by focusing on invariant or coherent structures in perturbed Rayleigh-Bénard convection to understand the mechanisms or global structures of fluid transport. Camassa and Wiggins [8] introduced the perturbed Hamiltonian model of Rayleigh-Bénard convection proposed by Solomon and Gollub [63] and investigated the stable and unstable manifolds theoretically and numerically in order to clarify the mechanism of chaotic transport by the so-called *lobe dynamics*. Fig.1.1.4 illustrates the schematic illustration of stable and unstable manifolds in perturbed Rayleigh-Bénard convection. Briefly speaking, a lobe is a region enclosed by stable and unstable manifolds, which is indicated in red, orange, blue, and green in Fig.1.1.4. When the Poincaré map of a two-dimensional perturbed dynamical system is an area- and orientation-preserving diffeomorphism, points inside lobes are mapped to another lobe by a Poincaré map. Hence, as is shown in Fig.1.1.4, fluid inside lobe L_k is transported to another lobe in each period of perturbation, where the Poincaré map is denoted as P in Fig.1.1.4. Since the stable and unstable manifolds in perturbed Rayleigh-Bénard convection entangle with each other very complicatedly as homoclinic tangles, the points inside lobes are transported chaotically by horseshoe maps; see Wiggins [76] and Rom-Kedar and Wiggins [57] for more details. Camassa and Wiggins [8] showed that the volume of fluid that crosses cell boundaries increases linearly with the amplitude of the perturbation when the amplitude is small in accordance with the results in Solomon and Gollub [63]. In addition, they discussed the effect of molecular diffusion in perturbed Rayleigh-Bénard convection as well. Malhotra, Mezić, and Wiggins [46] studied the patchiness of the perturbed Hamiltonian model of Rayleigh-Bénard convection with stable and unstable manifolds, where a patch is a region that has a considerably different average velocity compared to the surrounding region.

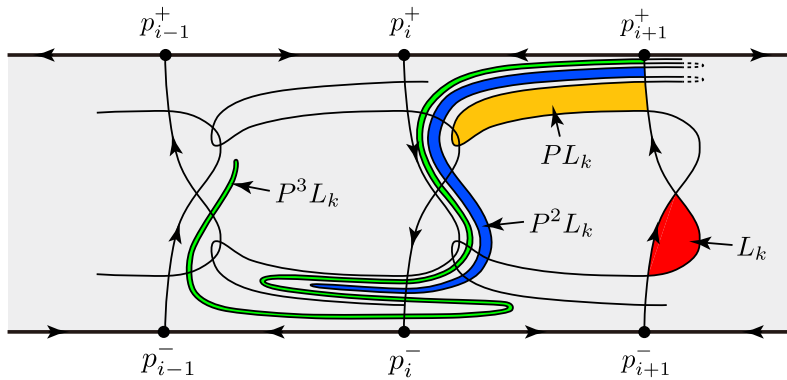


Figure 1.1.4: Lobe dynamics in perturbed Rayleigh-Bénard convection

Further, some studies were made by exploring *Lagrangian coherent structures* (LCSs). LCSs correspond to invariant manifolds in non-autonomous systems. Especially, hyperbolic LCSs correspond to stable and unstable manifolds in autonomous systems. The idea of hyperbolic LCSs was introduced by Haller and Yuan [31] to elucidate the mixing structures of two-dimensional turbulence. Then, it was shown by Shadden, Lekien, and Marsden [60] that the LCSs for a two-dimensional system can be mathematically defined as a ridge of a Finite-Time Lyapunov Exponent (FTLE) field. In that study, they also detected the hyperbolic LCSs in a two-dimensional model of double-gyre similar to perturbed Rayleigh-Bénard convection. Later on, Lekien, Shadden, and Marsden [42] gave a mathematical definition for n -dimensional LCSs and numerically analyzed the hyperbolic LCSs in three-dimensional model of perturbed Rayleigh-Bénard convection extended from the two-dimensional one proposed by Solomon and Gollub [63]. Further, Haller [27] and Farazmand and Haller [18] defined the hyperbolic LCSs by using variational theories. Then, elliptic LCSs were introduced by Haller and Beron-Vera [29] to analyze coherent material vortices in two-dimensional turbulence. Briefly speaking, elliptic LCSs are boundaries of fluid that is transported stably as a sort of vortex in the Lagrangian description. Hence, hyperbolic and elliptic LCSs are associated with chaotic and stable fluid transport respectively.

Previous works on fluid transport in other time-dependent convective flow. Let us briefly review some studies on fluid transport in other time-dependent convective flow. Some of them use magnetohydrodynamic forcing or electrical techniques to create convection similar to perturbed Rayleigh-Bénard convection, since it is easier to control the flow. Solomon, Tomas, and Warner [65, 66] experimentally detected some lobes by observing the transport of impurities in a fluid layer with a chain of horizontal vortices that are oscillated by magnetohydrodynamic forcing. Solomon and Mezić [64] explored the uniform mixing of weakly three-dimensional and weakly time-periodic vortex flow by using magnetohydrodynamic techniques in experiments and by numerically analyzing a low-dimensional model. Hidaka et al. [33] and Yamanaka et al. [79] experimentally analyzed the Lagrangian chaos and diffusion in weakly turbulent electroconvection of nematic liquid crystals.

On the other hand, some studies were dedicated on the investigation of the fluid transport in developed or turbulent Rayleigh-Bénard convection. For instance, a dual-porosity model was developed by Matveev [47] to describe the transport of impurities in developed Rayleigh-Bénard convection in two situations with chain of rolls and hexagonal lattice, where the trans-

port was studied for a wide range of Ra . Cheng et al. [11] and Hang et al. [32] studied the LCSs in turbulent Rayleigh-Bénard convection by computing the flow by Direct Numerical Simulations (DNS) in order to analyze material and heat transfer. Schneide et al. [58] and Schneide et al. [59] also explored the Lagrangian transport in turbulent Rayleigh-Bénard convection to detect the large-scale patterns called turbulent superstructures and to clarify the mechanism of heat transfer respectively.

Previous works in our research group. Our research group have investigated the chaotic fluid transport in the two-dimensional perturbed Hamiltonian model of Rayleigh-Bénard convection originally proposed by Solomon and Gollub [63] and introduced by Camassa and Wiggins [8] by focusing on Poincaré maps and hyperbolic LCSs. Fig.1.1.5 depicts the hyperbolic LCSs in the model, where T_{int} and T denote the integration time of the LCSs and the period of the perturbation respectively. Repelling and attracting LCSs which correspond to stable and unstable manifolds are indicated in blue and red respectively. The initial time is $t_0 = 0$ and the parameters are set to

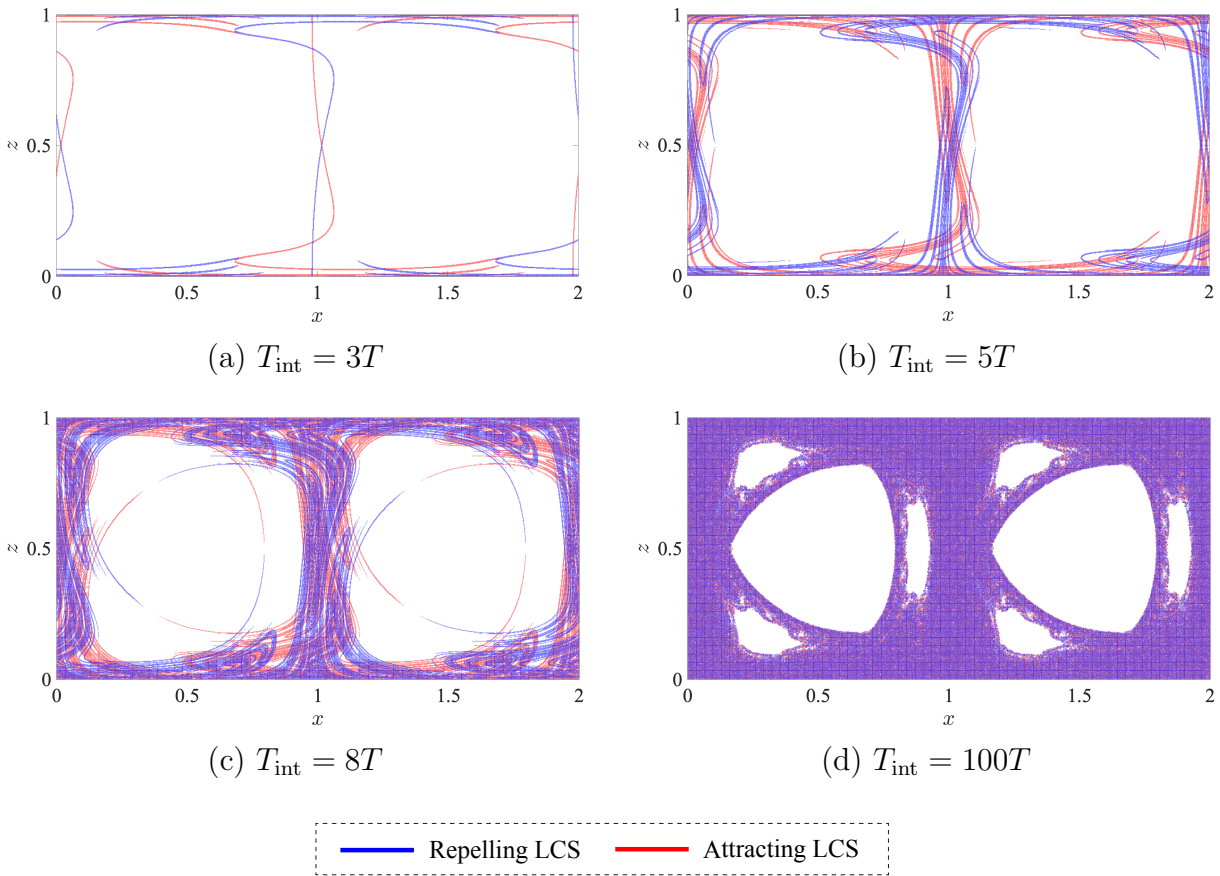


Figure 1.1.5: Hyperbolic LCSs in the perturbed Hamiltonian model

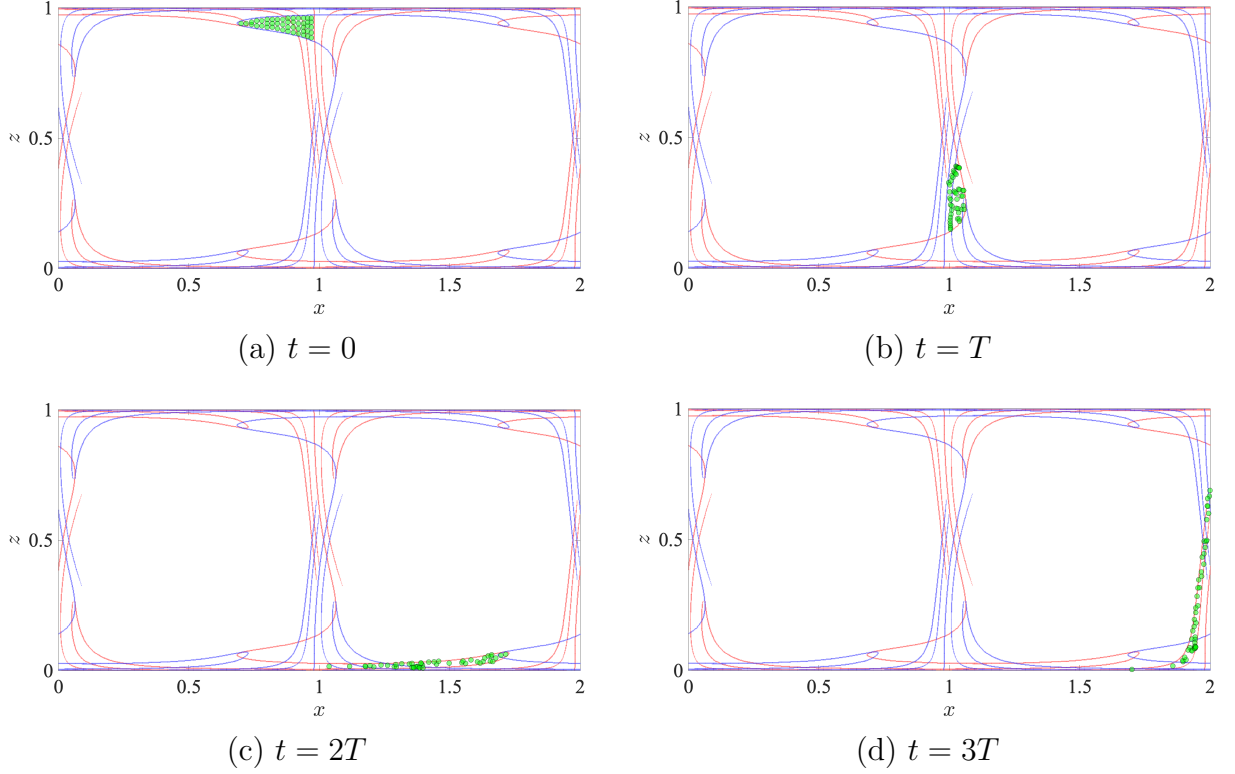


Figure 1.1.6: The transport of fluid particles inside a lobe

$A = \pi, k = \pi, T = 1/\pi, \varepsilon = 0.1$, which are the same for the Poincaré maps in Fig.1.1.3. As can be seen, we have clarified that the hyperbolic LCSs seem to fill up the chaotic regions when the integration time of the LCSs is large enough. It follows that the topological structures of hyperbolic LCSs with large integration time may correspond to that of Poincaré maps. Further, Fig.1.1.6 depicts the transport of fluid particles which initially locate in a lobe near a cell boundary, where the integration time of the LCSs is $T_{\text{int}} = 4T$. As is shown, we have detected some lobes in the model by computing hyperbolic LCSs and have verified that fluid particles inside a lobe is transported from one lobe to another in each period of perturbation in accordance with lobe dynamics.

Previous works on periodic orbits and bifurcations in convective flow. As is described in the above, most of the past works regarding the fluid transport in convective flow have been focused on the mechanisms and structures of chaotic transport. For the sake of understanding the global structures of fluid transport it is quite essential to investigate periodic transport as well, since periodic orbits are one of the most simple orbits. Furthermore, it is necessary to clarify how the transport becomes complicated when Ra is increased, in

other words, how the periodic orbits bifurcate when the amplitude of the perturbation is increased.

Now we shall briefly review some previous works analyzing periodic orbits and their bifurcations in convective flow in the Lagrangian description. Simó et al. [61] studied the structures of regular and chaotic regions in three particular three-dimensional steady Rayleigh-Bénard convection with different Ra by computing Poincaré maps and periodic points as well as critical points and Lyapunov exponents, and showed how the structures of fluid transport vary with Ra . Chabreyrie, Chandre, and Aubry [9] proposed a strategy to create sufficient chaotic mixing in two-dimensional oscillatory electro-osmotic convection by focusing on the variation of the stability of periodic pathlines associated with non-mixing regions when the amplitude or frequency of the perturbation is changed. In addition, Lagrangian chaos in two-dimensional oscillatory convection in a differentially heated cavity was studied by Oteski, Duguet, and Pastur [52]. In that study, they detected not only elliptic periodic points but also hyperbolic ones and their stable and unstable manifolds as well to clarify the dependence of mixing structures on Ra . Contreras, Speetjens, and Clercx [13] also explored the Lagrangian transport in three-dimensional steady convection in a differentially heated cavity and investigated how the chaotic structures vary with Grashof number Gr by analyzing periodic points and Poincaré maps.

On the other hand, the transitions, in other words bifurcations, of thermal convection from steady to oscillatory and chaotic flow have been explored in the Eulerian description in many studies by experiments, CFD simulations, and analyses on low-dimensional models; see for instance Gollub and Benson [21], Mukutmoni and Yang [48, 49], and Paul, Wahi, and Verma [56]. In particular, Net and Umbriá [50] and Umbriá and Net [69] analyzed the stabilities and bifurcations as well as symmetric properties of thermal flow in a tall rectangular domain with heated sidewalls when Ra is varied, where bifurcation diagrams are numerically computed by detecting *periodic orbits*, which may correspond to time-periodic flow in the Eulerian description. In addition, the resonance of quasi-periodic Rayleigh-Bénard convection was studied by Ecke and Kevrekidis [16] and Ecke, Mainieri, and Sullivan [17] in the Eulerian description.

1.2 Motivations of this study

Motivations of this study. As is shown in the above, there are some studies where periodic orbits in convective flow have been investigated in the

Lagrangian description. However, it goes without saying that they have not been analyzed enough in the sense of global investigation. For example, some only detect elliptic periodic points, or others investigate periodic points only at some fixed parameters. In particular, the global structures of m -periodic orbits ($m \in \mathbb{N}$) in perturbed Hamiltonian model of Rayleigh-Bénard convection have not been studied adequately in the perspectives of resonance and symmetry. It is crucial to investigate the resonances and symmetries of m -periodic orbits, since they are one of the important topological properties of periodic orbits. Furthermore, the bifurcations of periodic orbits with Ra as a control parameter have not been sufficiently explored in the Lagrangian description, since most of the previous researches have studied them in the Eulerian description. Needless to say, it is important to clarify the global structure of bifurcations of m -periodic orbits in a perturbed Hamiltonian model in order to clarify how the transport becomes complicated when Ra is increased.

Although such analysis on a low-dimensional system is important to understand the global structures of fluid transport, it is essential as well to analyze the invariant structures of Rayleigh-Bénard convection by experiments for the sake of practical application such as the prediction and control of chemical spills in the environment, since Rayleigh-Bénard convection is a typical natural convection. Especially, it is crucial to investigate the hyperbolic and elliptic LCSs to understand the chaotic and stable fluid transport respectively. In addition, we need to look into periodic points as well to analyze the elliptic LCSs. However, the invariant structures of Rayleigh-Bénard convection have not been studied enough by experiments.

1.3 Contributions and organization of this thesis

Contributions of this thesis. In this thesis we explore the global structures of fluid transport in perturbed Rayleigh-Bénard convection theoretically, numerically, and experimentally by focusing on invariant structures such as periodic orbits and Lagrangian coherent structures. We have two main goals.

The first goal is to clarify the global structures of periodic orbits in the perspectives of symmetry and resonance as well as bifurcation in the two-dimensional perturbed Hamiltonian model of Rayleigh-Bénard convection, which was originally developed by Solomon and Gollub [63] and introduced by Camassa and Wiggins [8]. To do this, we first extend the non-autonomous system to an autonomous system in the extended phase space and define

a Poincaré map. Then, we numerically detect the elliptic and hyperbolic periodic points on the Poincaré section and investigate the structures of the associated periodic orbits in the extended phase space. Next, we consider the projection of periodic orbits onto the original phase space to investigate the resonances and symmetries of periodic orbits. Lastly, we show the global structures of ε -parameter bifurcations of periodic orbits, where ε denotes the amplitude of perturbation.

The second goal is to detect hyperbolic and elliptic LCSs as well as periodic points in perturbed Rayleigh-Bénard convection by experiments in order to clarify the global structures of chaotic and stable fluid transport. To do this, we develop an experimental apparatus to measure the two-dimensional velocity fields of perturbed Rayleigh-Bénard convection by Particle Image Velocimetry (PIV). Then, we numerically obtain the LCSs and periodic points by using the obtained velocity data. In particular, we show that some fluid particles may be transported chaotically by horseshoe maps, while some others may be transported stably. Finally, we propose a novel perturbed Hamiltonian model that elucidates the experimental results better by qualitatively representing the velocity fields obtained by PIV analysis, since in experiments we have observed some structures that are different from those in the model proposed by Solomon and Gollub [63] and Camassa and Wiggins [8]. It is important to develop a low-dimensional dynamical system because essential structures of the flow that may not been observed in experiments may become clear.

Organization of this thesis. The organization of this thesis is illustrated in Fig.1.3.1. In Chap.2, the two-dimensional perturbed Hamiltonian model of Rayleigh-Bénard convection is first described together with symmetric properties. Then, periodic points are numerically detected by using Poincaré maps and the structures of periodic orbits are discussed in the perspectives of symmetry and resonance. In Chap.3, the ε -parameter bifurcations of periodic orbits in the perturbed Hamiltonian model are illustrated and, in particular, the classification of the bifurcations is made into fold or flip bifurcations according to the multipliers of the periodic points. Hence, Chap.2 and Chap.3 discuss the periodic fluid transport in the perturbed Hamiltonian model theoretically and numerically. Recall that chaotic fluid transport in the model have already been actively studied by others. Then in Chap.4, hyperbolic and elliptic LCSs as well as periodic points in perturbed Rayleigh-Bénard convection are experimentally detected from the two-dimensional velocity data obtained by PIV analysis. Thus, in this chapter both chaotic and stable fluid

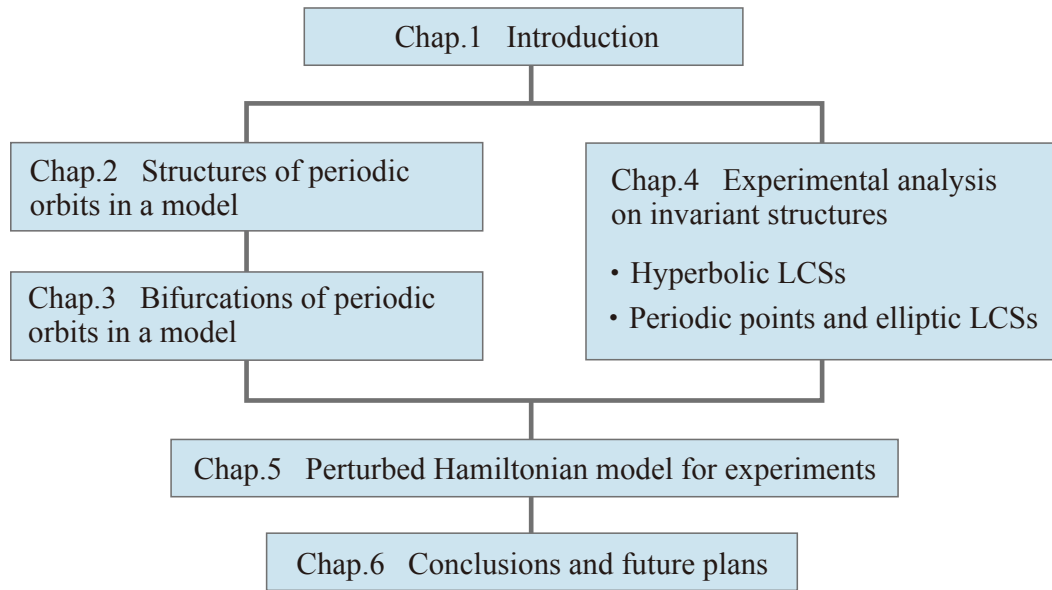


Figure 1.3.1: The organaization of this thesis

transport are discussed by experiments. However, in experiments we observe some structures that do not appear in the perturbed Hamiltonian model investigated in Chap.2 and Chap.3. Therefore, in Chap.5, a novel perturbed Hamiltonian model for Rayleigh-Bénard convection is proposed to elucidate the experimental results. Finally in Chap.6, conclusions and future plans are described.

Chapter 2

Structures of periodic orbits in a model

In order to investigate the global structures of periodic transport in two-dimensional Rayleigh-Bénard convection whose velocity field is perturbed by even oscillatory instability, we employ the two-dimensional perturbed Hamiltonian system, which was originally developed by Solomon and Gollub [63] and introduced by Camassa and Wiggins [8]. Then, we detect the periodic points on the Poincaré section of the perturbed Hamiltonian system and investigate the resonances and symmetries of periodic orbits which are solution curves passing through periodic points.

2.1 Model of perturbed Rayleigh-Bénard convection

Hamiltonian system of steady Rayleigh-Bénard convection. By assuming the stress-free boundary condition, it follows from the Navier-Stokes equations with the Boussinesq approximation that two-dimensional steady Rayleigh-Bénard convection can be modeled by a Hamiltonian system as

$$\begin{aligned}\frac{dx}{dt} &= -\frac{\partial H_0(x, z)}{\partial z} = -\frac{A\pi}{k}\sin(kx)\cos(\pi z), \\ \frac{dz}{dt} &= \frac{\partial H_0(x, z)}{\partial x} = A\cos(kx)\sin(\pi z),\end{aligned}\tag{2.1.1}$$

where $H_0(x, z)$ is a Hamiltonian, given by the stream function

$$H_0(x, z) = \frac{A}{k}\sin(kx)\sin(\pi z);$$

see Chandrasekhar [10]. In the above, $x \in \mathbb{R}$ and $z \in U = [0, 1] \subset \mathbb{R}$ are the horizontal and vertical coordinates respectively, and hence we define the phase space $M = \mathbb{R} \times U$. Further, A denotes the amplitude of the

velocity in z direction and k is the wave number of the cell pattern in x direction. In this Hamiltonian system, we have the hyperbolic equilibrium points $p_{i,0}^\pm = (x_{i,0}, z_i^\pm)$ as

$$(x_{i,0}, z_i^\pm) = \left(\frac{i\pi}{k}, z_i^\pm \right), \quad (i = 0, \pm 1, \pm 2, \dots),$$

where $z_i^- = 0$ and $z_i^+ = 1$, and it is noticed that there exist heteroclinic connections between $p_{i,0}^+$ and $p_{i,0}^-$ along the roll boundaries.

Hamiltonian model of perturbed Rayleigh-Bénard convection. Now we consider the case in which a time-periodic term $\varepsilon \cos(\omega t)$ is added to x in the Hamiltonian $H_0(x, z)$ for the steady Rayleigh-Bénard convection. Then, it follows that a time-dependent Hamiltonian on the extended phase space $M \times \mathbb{R}$ is given in coordinates $(x, z, t) \in M \times \mathbb{R}$ as

$$H(x, z, t) := H_0(x, z) + \varepsilon H_1(x, z, t),$$

where Taylor expansion is applied to the sinusoidal term as

$$H_1(x, z, t) = A \cos(\omega t) \cos(kx) \sin(\pi z).$$

Note that A denotes some given constant of the magnitude. Then, we get a non-autonomous Hamiltonian vector field $X_H : M \times \mathbb{R} \rightarrow TM$, locally given by

$$\begin{aligned} \frac{dx}{dt} &= -\frac{\partial H(x, z, t)}{\partial z} = -\frac{\partial H_0(x, z)}{\partial z} - \varepsilon \frac{\partial H_1(x, z, t)}{\partial z}, \\ \frac{dz}{dt} &= \frac{\partial H(x, z, t)}{\partial x} = \frac{\partial H_0(x, z)}{\partial x} + \varepsilon \frac{\partial H_1(x, z, t)}{\partial x}. \end{aligned} \tag{2.1.2}$$

In the above, $\varepsilon \in \mathbb{R}^+$ is a given magnitude of the perturbation and the perturbed terms $\frac{\partial H_1(x, z, t)}{\partial z}$ and $\frac{\partial H_1(x, z, t)}{\partial x}$ are respectively given by the periodic function:

$$\begin{aligned} \frac{\partial H_1(x, z, t)}{\partial z} &= A\pi \cos(\omega t) \cos(kx) \cos(\pi z), \\ \frac{\partial H_1(x, z, t)}{\partial x} &= -Ak \cos(\omega t) \sin(kx) \sin(\pi z). \end{aligned}$$

Symmetric properties of the model. Recall from Camassa and Wiggins [8] that the perturbed Hamiltonian system (2.1.2) is invariant under the following coordinate transformations:

$$\begin{aligned}
\text{i)} \quad & x \mapsto x + \frac{2a\pi}{k}, \quad z \mapsto -z + 1, \quad t \mapsto -t + bT, \\
\text{ii)} \quad & x \mapsto x + \frac{(2a+1)\pi}{k}, \quad z \mapsto z, \quad t \mapsto -t + bT, \\
\text{iii)} \quad & x \mapsto x + \frac{2a\pi}{k}, \quad z \mapsto z, \quad t \mapsto t + bT,
\end{aligned}$$

where $T(= 2\pi/\omega)$ is the period of the perturbation and $a, b \in \mathbb{Z}$. Note that there exists two more symmetries associated with the following transformation:

$$\begin{aligned}
\text{iv)} \quad & x \mapsto -x + \frac{(2a+1)\pi}{k}, \quad z \mapsto z, \quad t \mapsto -t + \left(b + \frac{1}{2}\right)T, \\
\text{v)} \quad & x \mapsto -x + \frac{(2a+1)\pi}{k}, \quad z \mapsto -z + 1, \quad t \mapsto t + \left(b + \frac{1}{2}\right)T,
\end{aligned}$$

which will be used for investigating symmetries of periodic orbits in §2.5.

2.2 Structures of periodic points

In this section, we numerically compute Poincaré maps to detect periodic points on a Poincaré section. To do this, we transform the perturbed Hamiltonian system that is a non-autonomous system on $M = \mathbb{R} \times U$ with local coordinates (x, z) into the setting of an autonomous system by introducing the extended phase space $\mathcal{M} = M \times S^1$ with local coordinates (x, z, θ) and then define a Poincaré map $P_\varepsilon^{\theta_0} : \Sigma^{\theta_0} \longrightarrow \Sigma^{\theta_0}$, where $\Sigma^{\theta_0} \subset \mathcal{M}$ is a chosen Poincaré section.

Autonomous Hamiltonian system. By introducing an angle variable $\theta := \omega t + \theta_0 \in S^1$, where $\theta_0 \in [0, 2\pi)$, the Hamiltonian can be rewritten on the extended phase space $\mathcal{M} = M \times S^1$ as

$$H(x, z, \theta) := H_0(x, z) + \varepsilon H_1(x, z, \theta),$$

where

$$H_1(x, z, \theta) = A \cos(\theta - \theta_0) \cos(kx) \sin(\pi z).$$

Then, the vector field for the non-autonomous Hamiltonian system given in (2.1.2) can be transformed into the form of the vector field $X_H : \mathcal{M} \longrightarrow T\mathcal{M}$ of the autonomous system on the extended phase space \mathcal{M} , which can be

described by using local coordinates (x, z, θ) :

$$\begin{aligned}\frac{dx}{dt} &= -\frac{\partial H(x, z, \theta)}{\partial z} = -\frac{\partial H_0(x, z)}{\partial z} - \varepsilon \frac{\partial H_1(x, z, \theta)}{\partial z}, \\ \frac{dz}{dt} &= \frac{\partial H(x, z, \theta)}{\partial x} = \frac{\partial H_0(x, z)}{\partial x} + \varepsilon \frac{\partial H_1(x, z, \theta)}{\partial x}, \\ \frac{d\theta}{dt} &= \omega,\end{aligned}\tag{2.2.1}$$

and the perturbed terms are given as

$$\begin{aligned}\frac{\partial H_1(x, z, \theta)}{\partial z} &= A\pi \cos(\theta - \theta_0) \cos(kx) \cos(\pi z), \\ \frac{\partial H_1(x, z, \theta)}{\partial x} &= -Ak \cos(\theta - \theta_0) \sin(kx) \sin(\pi z).\end{aligned}$$

Poincaré map of the model. Associated with the autonomous Hamiltonian system described in (2.2.1), let $\phi^\varepsilon : \mathbb{R} \times \mathcal{M} \longrightarrow \mathcal{M}$; $(t, x, z, \theta) \longmapsto \phi^\varepsilon(x, z, \theta)$ be the flow, where $t \in \mathbb{R}$ indicates a time interval. Hence, for some fixed t and given ε , we define the diffeomorphism on the extended phase space as

$$\phi_t^\varepsilon : \mathcal{M} \longrightarrow \mathcal{M}; (x, z, \theta) \longmapsto \phi_t^\varepsilon(x, z, \theta).$$

Let $(x(t), z(t), \theta(t))$ be an integral curve of the Hamiltonian system in (2.2.1). For some fixed θ_0 , the angle variable $\theta(t)$ may be written as a periodic function with period $T = 2\pi/\omega$ such that $\theta(t) = \theta_0 + \omega t = \theta_0 + 2\pi t/T$. For each discrete time $t = kT$, $k \in \mathbb{Z}$, we can identify θ with $\theta_0 + 2\pi k$ and the equivalent class $[\theta]$ of S^1 is given by $[\theta] := \{\theta \in S^1 \mid \theta = \theta_0 + 2\pi k\}$. Choose a representative θ_0 for the equivalent class to define a Poincaré section Σ^{θ_0} by setting

$$\Sigma^{\theta_0} := \{(x, z, \theta_0) \in \mathcal{M}/S^1 \mid (x, z) \in M, \theta_0 \in [\theta]\}.\tag{2.2.2}$$

Then, for some fixed parameter $\varepsilon \in \mathbb{R}$, we define a Poincaré map $P_\varepsilon^{\theta_0}$ on Σ^{θ_0} by

$$P_\varepsilon^{\theta_0} := \phi_T^\varepsilon \Big|_{\Sigma^{\theta_0}} : \Sigma^{\theta_0} \longrightarrow \Sigma^{\theta_0},$$

which is locally given by

$$\begin{aligned}(x(kT), z(kT), \theta(kT) = \theta_0 + 2\pi k \equiv \theta_0) \\ \longmapsto (x((k+1)T), z((k+1)T), \theta((k+1)T) = \theta_0 + 2\pi(k+1) \equiv \theta_0).\end{aligned}$$

Note that one special choice for θ_0 may be $\theta_0 = 0$ and then the Poincaré section Σ^{θ_0} is locally isomorphic to $M \cong \mathcal{M}/S^1$. Hence, we note that a point on Σ^{θ_0} is mapped by $P_\varepsilon^{\theta_0} : \Sigma^{\theta_0} \longrightarrow \Sigma^{\theta_0}$ to another point on Σ^{θ_0} during the period T .

Periodic points. A fixed point of the Poincaré map corresponds to a *periodic orbit* with period T for the flow, and an *m-periodic point*, which corresponds to the periodic orbit with period mT ($m \in \mathbb{Z}^+$), namely the *m-periodic orbit*, is the fixed point $\mathbf{x}_0 \in \Sigma^{\theta_0}$ such that

$$\begin{aligned} (P_\varepsilon^{\theta_0})^m(\mathbf{x}_0) &= \mathbf{x}_0, \\ \text{while } (P_\varepsilon^{\theta_0})^\ell(\mathbf{x}_0) &\neq \mathbf{x}_0 \text{ for } 1 \leq \ell \leq m-1 \text{ } (m \geq 2), \end{aligned} \tag{2.2.3}$$

where

$$(P_\varepsilon^{\theta_0})^m = \underbrace{(P_\varepsilon^{\theta_0}) \circ \cdots \circ (P_\varepsilon^{\theta_0})}_m.$$

Since the Poincaré section Σ^{θ_0} is two-dimensional, it is apparent that the Jacobian matrix of the Poincaré m -return map

$$J_\varepsilon(\mathbf{x}) := \frac{\partial (P_\varepsilon^{\theta_0})^m(\mathbf{x})}{\partial \mathbf{x}}$$

have two eigenvalues. Especially, the eigenvalues of the Jacobian matrix evaluated at an periodic point is called the *multipliers*. Let μ_1 and μ_2 be the two multipliers of an m -periodic point $\mathbf{x}_0 \in \Sigma^{\theta_0}$, where $|\mu_1| \leq |\mu_2|$. Since $|J_\varepsilon(\mathbf{x}_0)| = 1$, the multipliers have the product $\mu_1\mu_2 = 1$. The m -periodic points are classified according to the conditions of the associated multipliers as follows (see Guckenheimer and Holmes [24]):

- hyperbolic: $|\mu_1| < 1 < |\mu_2|$
- elliptic: $|\mu_i| = 1$ but $\mu_i \neq \pm 1$ ($i = 1, 2$)
- parabolic: $\mu_i = \pm 1$ ($i = 1, 2$)

The periodic orbits are stable when the associated periodic points are elliptic, while they are unstable when the associated ones are hyperbolic.

Numerical algorithm for detecting periodic points. Now we compute the image of the Poincaré map $P_\varepsilon^{\theta_0} : \Sigma^{\theta_0} \rightarrow \Sigma^{\theta_0}$ in order to detect periodic points, each of which corresponds to a periodic orbit in \mathcal{M} through itself. First, we describe our numerical algorithm for detecting m -periodic points for some *fixed* amplitude ε of the perturbation. Define a map $F_\varepsilon : \Sigma^{\theta_0} \rightarrow \mathbb{R}^2$ as

$$F_\varepsilon(\mathbf{x}) := \mathbf{x} - (P_\varepsilon^{\theta_0})^m(\mathbf{x}), \text{ for } \mathbf{x} = (x, z) \in \Sigma^{\theta_0}.$$

For detecting m -periodic points, we shall numerically compute the kernel of the map F_ε to find a solution \mathbf{x} for $F_\varepsilon(\mathbf{x}) = \mathbf{0}$, where we employ Newton's method as follows:

Numerical algorithm for detecting an m -periodic point:

- (1) Set $k = 0$ with an initial approximation $\mathbf{x}^{(0)}$ for the required m -periodic point.
- (2) Set $k := k + 1$ and compute the k -th approximation $\mathbf{x}^{(k)}$ by Newton's method as

$$\mathbf{x}^{(k)} := \mathbf{x}^{(k-1)} - \left(\frac{\partial F_\varepsilon(\mathbf{x})}{\partial \mathbf{x}} \bigg|_{\mathbf{x}=\mathbf{x}^{(k-1)}} \right)^{-1} F_\varepsilon(\mathbf{x}^{(k-1)}),$$

where

$$\frac{\partial F_\varepsilon(\mathbf{x})}{\partial \mathbf{x}} \bigg|_{\mathbf{x}=\mathbf{x}^{(k-1)}} = \mathbf{I} - J_\varepsilon(\mathbf{x}^{(k-1)}).$$

Here, \mathbf{I} is the unit matrix and the Jacobian matrix

$$J_\varepsilon(\mathbf{x}^{(k-1)}) = \frac{\partial (P_\varepsilon^{\theta_0})^m(\mathbf{x})}{\partial \mathbf{x}} \bigg|_{\mathbf{x}=\mathbf{x}^{(k-1)}}$$

is numerically obtained by using the central difference scheme.

- (3) If $|F_\varepsilon(\mathbf{x}^{(k)})| < \delta$, where the convergence radius is set to $\delta = 10^{-10}$, then the computation ends up and the m -periodic point is to be detected as $\mathbf{x} = \mathbf{x}^{(k)}$.
- (4) Otherwise, return to (2) in order to iterate the computation until convergence.

Remark 2.2.1. Since the approximation value of the periodic points are unknown, we cover the Poincaré section with a small grid spacing and set each grid point as the initial condition $\mathbf{x}^{(0)}$. In our computation the grid spacing is set to 0.005. The Poincaré maps are computed with 7th-order Runge-Kutta method with double precision floating point, which are the same through Chap.2, Chap.3, and Chap.5.

Periodic points at $\varepsilon = 0.1$. Let us consider to detect the periodic points for the case $\varepsilon = 0.1$. For the numerical computations related to this model, throughout this thesis, we fix the other parameters to $A = \pi, k = \pi, T = 1/\pi$. Now we illustrate in Fig.2.2.1 the image of the Poincaré section by the

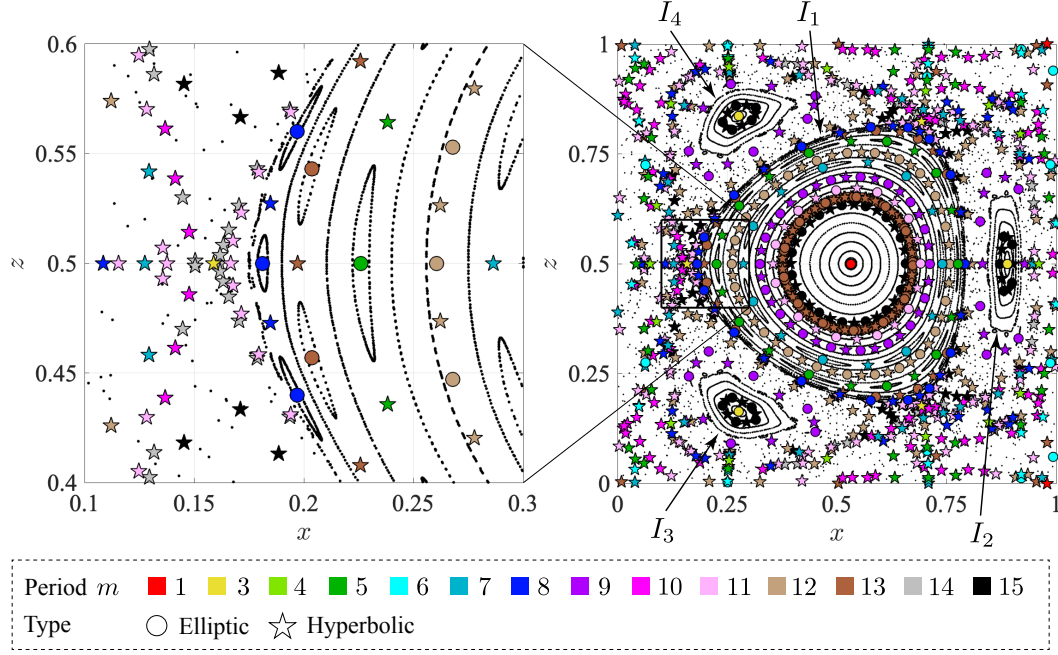


Figure 2.2.1: Structures of elliptic and hyperbolic periodic points ($\varepsilon = 0.1$)

Poincaré map and the detected periodic points in a cell which range from $x = 0$ to $x = 1 (= \pi/k)$, where the elliptic and hyperbolic periodic points with period $m \leq 15$ are depicted. The color and the shape of the plots denote the period m and the symbols of plots, i.e., \bullet and \star , indicate elliptic and hyperbolic respectively. The number of recurrences due to the Poincaré map is set to $N = 1000$ and the initial condition for θ is $\theta_0 = 0$. Note that there is no loss of generality to investigate only one single cell, since there is a topological isomorphism among cells. The left figure in Fig.2.2.1 shows an enlarged view of the squared section in the right figure of Fig.2.2.1. In conjunction with symmetry, it is observed that the periodic points appear symmetrically with respect to $z = 1/2$, which is consistent with the symmetric property i) of the non-autonomous system in (2.1.2).

Periodic points and KAM curves. It is apparent from the Poincaré map that there exists one large island in the middle of the cell which we denote by label I_1 , while there are three small islands surrounding the main island I_1 , each of which is respectively denoted by labels I_2 , I_3 , and I_4 as in Fig.2.2.1. As is well known, inside the islands, there exist quasi-periodic points, while outside the islands there is a chaotic sea where points correspond to chaotic orbits. We can see that elliptic and hyperbolic periodic points inside the islands appear alternately along KAM curves in the perturbed Hamiltonian system as is well known; see Guckenheimer and Holmes [24] and Doherty

and Ottino [15].

In particular, it is observed in Fig.2.2.1 that the elliptic periodic points appear at the center of islands, which is surrounded by KAM curves. For example, the elliptic 3-periodic points exist at the center of islands I_2 , I_3 , and I_4 in Fig.2.2.1, and the elliptic 5, 7, 8, and 13-periodic points appear at the center of the small islands in I_1 . The relation between the elliptic periodic points and the islands will be discussed in detail in §2.3. In contrast, it is observed that the hyperbolic periodic points appear in the chaotic regions. This is because the stable and unstable manifolds associated with the hyperbolic periodic points form complicated homoclinic tangles around them and the points in the neighborhood are to be transported chaotically. Further, we note that some of the elliptic and hyperbolic periodic points do not appear as mentioned above, since not all of the islands and chaotic regions can be numerically detected in Fig.2.2.1. Especially, the chaotic regions between KAM curves in the islands cannot be observed in details.

2.3 Structures of periodic orbits and KAM tori.

As we have shown in Fig.2.2.1, the elliptic periodic points appear at the center of the islands of KAM tori. In this section, we investigate the structures of periodic orbits and KAM tori in the extended phase space $\mathcal{M} = M \times S^1$, which are associated with elliptic periodic points. Here, we especially focus on those associated with the elliptic 3-periodic points at the center of islands I_2 , I_3 , and I_4 in Fig.2.2.1.

Twisted structures of periodic orbits and KAM tori. Fig.2.3.1a illustrates the elliptic 3-periodic points at the center of islands I_2 , I_3 , and I_4 on the Poincaré section Σ^{θ_0} . Their 3-periodic orbit and the associated KAM torus in the extended phase space \mathcal{M} are shown in Fig.2.3.1b in yellow and blue respectively. The Poincaré section Σ^{θ_0} given in (2.2.2) is depicted in gray, where it is restricted to $U \times U \subset M$ and where we choose $\theta_0 = 0$ for $[\theta] = \theta_0 + 2\pi k$. The intersection of the KAM torus and the Poincaré section Σ^{θ_0} corresponds to the KAM curve of the island, and those of the periodic orbit $\tilde{c} \in \mathcal{M}$ and Σ^{θ_0} corresponds to the elliptic 3-periodic points. It is apparent that the periodic orbit and the associated KAM tori for the 3-periodic points are connected with each other and thus they globally have a twisted structure. Generally, this implies that KAM tori for elliptic periodic points whose period is more than two have twisted structures in the extended phase space \mathcal{M} and also that the orbit of the elliptic periodic points goes through the center of it.

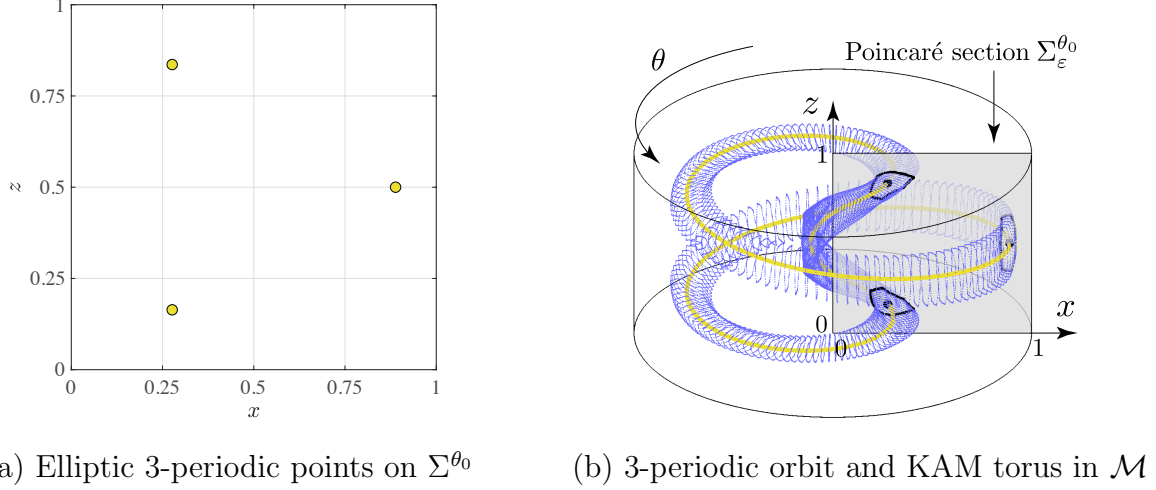


Figure 2.3.1: 3-periodic orbit and the associated KAM torus

Note that such KAM torus do not appear around the orbits of hyperbolic periodic points.

Periodic transport of islands. Since we have seen in Fig.2.3.1b that the KAM tori for each island are connected with each other, we next investigate the images of the island regions by Poincaré map $P_\varepsilon^{\theta_0}$. Let us denote the closed regions of island I_i as $R_i \subset U \times U$ for $i = 2, 3, 4$. Fig.2.3.2 shows the initial position and the image of the regions mapped by $P_\varepsilon^{\theta_0}$. In order to easily recognize the deformation of the regions, each of them is illustrated in four colors. The elliptic 3-periodic points are indicated in yellow plots. We can see that the regions of I_2, I_3 , and I_4 are mapped to I_3, I_4 , and I_2 respectively in order with the 3-periodic points as

$$P_\varepsilon^{\theta_0}(R_2) = R_3, \quad P_\varepsilon^{\theta_0}(R_3) = R_4, \quad P_\varepsilon^{\theta_0}(R_4) = R_2.$$

It follows that the region of each island is mapped to the same island after three times of Poincaré maps as

$$(P_\varepsilon^{\theta_0})^3(R_i) = R_i.$$

Of course, this implies that the region R of an island associated with an m -periodic point is mapped to the same island after m times of Poincaré maps as

$$(P_\varepsilon^{\theta_0})^m(R) = R.$$

Furthermore, Fig.2.3.2 indicates that the regions of the islands rotate around the 3-periodic points when they are mapped. It follows from the physical point of view that fluid in the region of an island is transported periodically

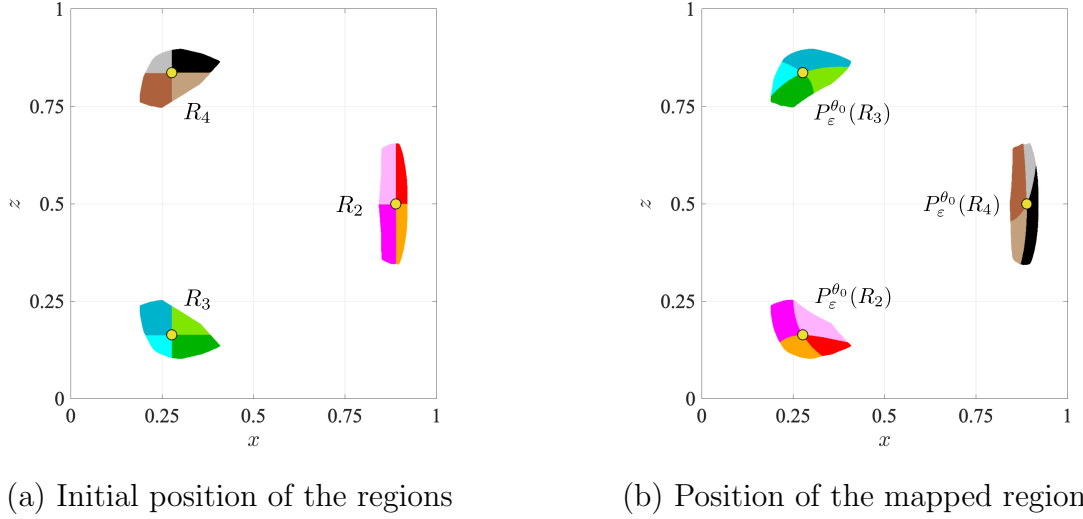


Figure 2.3.2: Mapping of the regions of the islands by a Poincaré map

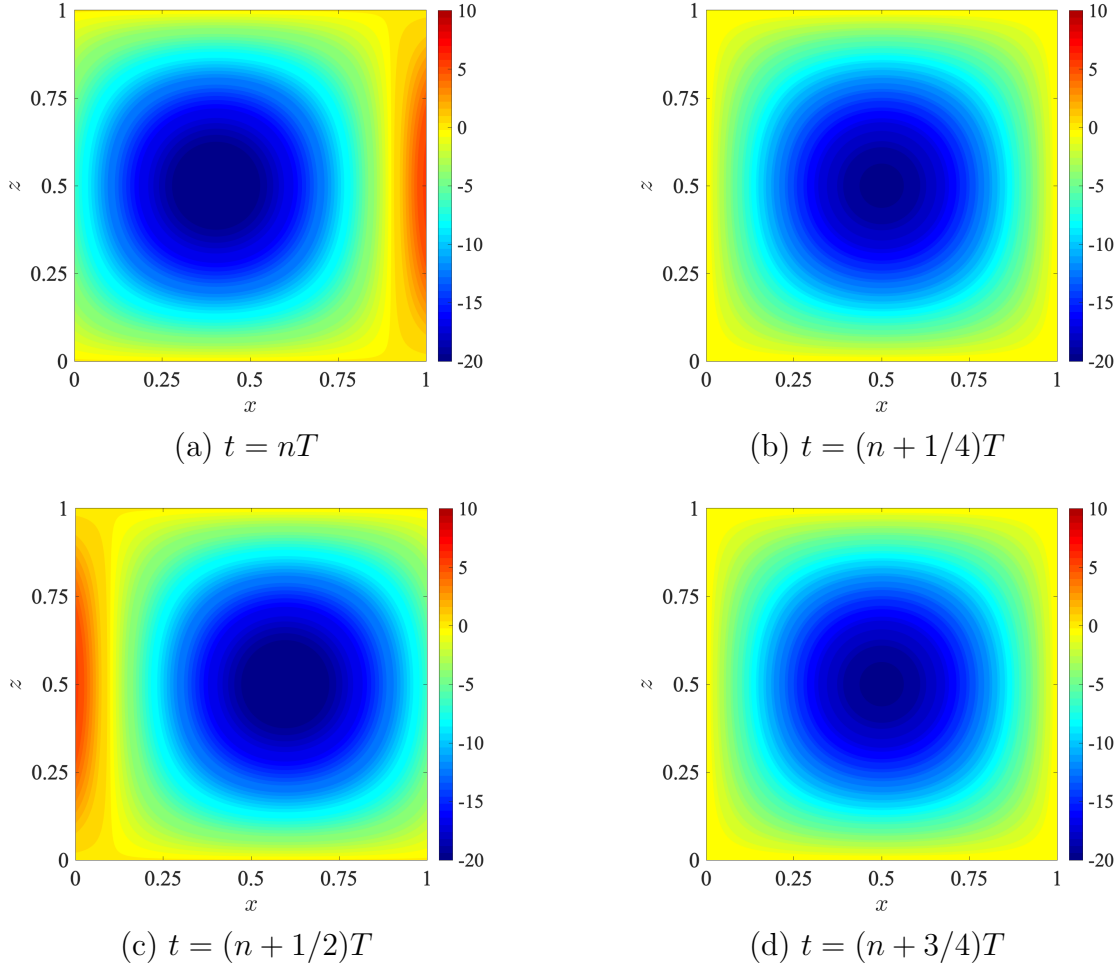
as a sort of vortex by the Lagrangian transport as a whole, though each point is transported quasi-periodically. The KAM curve in the region, which is an invariant manifold, seems to act as a barrier and enclose the fluid inside. Notice that these vortex structures do not appear in vorticity fields in the Eulerian description, which is illustrated in Fig.2.3.3. It seems that these structures are quite relevant with the *Lagrangian vortices* or *Lagrangian eddies*, which are regions that are transported stably as rotating regions. To be more precise, such vortices are defined as regions enclosed by elliptic Lagrangian coherent structures (LCSs). Let us make a brief review on elliptic LCSs by following Haller and Beron-Vera [29] and Haller and Beron-Vera [30].

Definition 2.3.1. Consider a two-dimensional dynamical system given by

$$\frac{d\mathbf{x}(t)}{dt} = \mathbf{v}(\mathbf{x}(t), t),$$

where \mathbf{x} is an element in an open region $D \subset \mathbb{R}^2$ and t denotes the time. We consider a closed curve γ on D at $t = t_0$ and denote it as $r(s)$ with parameter $s \in [0, \sigma]$. *Elliptic Lagrangian coherent structures* are defined as closed stationary curves of the averaged tangential strain along γ , given by

$$Q(\gamma) = \frac{1}{\sigma} \int_0^\sigma \frac{\sqrt{\langle r'(s), C_{t_0}^t(r(s))r'(s) \rangle}}{\sqrt{\langle r'(s), r'(s) \rangle}} ds,$$

Figure 2.3.3: Vorticity fields ($n \in \mathbb{Z}$)

where the finite-time Cauchy-Green tensor is given by

$$C_{t_0}^t(\mathbf{x}) = \frac{d\phi_{t_0}^{t_0+T}(\mathbf{x})}{d\mathbf{x}}^* \frac{d\phi_{t_0}^{t_0+T}(\mathbf{x})}{d\mathbf{x}}. \quad (2.3.1)$$

Here, $r'(s) := dr(s)/ds$ and $\langle \cdot, \cdot \rangle$ denotes the Euclidean inner product.

Such curves turn out to be closed solution curves of one of the two differential equations given by

$$r'(s) = \eta_\lambda^\pm(r(s)), \quad (2.3.2)$$

where

$$\eta_\lambda^\pm = \sqrt{\frac{\lambda_2 - \lambda^2}{\lambda_2 - \lambda_1}} \xi_1 \pm \sqrt{\frac{\lambda^2 - \lambda_1}{\lambda_2 - \lambda_1}} \xi_2,$$

and ξ_i and λ_i ($i = 1, 2$) are the eigenvectors and eigenvalues of the finite-time Cauchy-Green tensor in (2.3.1). Here, $\lambda > 0$ is some parameter. Hence, elliptic LCSs appear in families of limit cycles parametrized by λ .

Numerical methods for detecting elliptic LCSs. Let us briefly explain the numerical methods for detecting elliptic LCSs in perturbed Hamiltonian model. In order to compute vector fields η_λ^\pm we first obtain the flow maps in (2.3.1) by numerically integrating the velocity fields of the perturbed Hamiltonian system in (2.1.2) with 7th-order Runge-Kutta method. Then, we obtain the solution curves of (2.3.2) by numerically integrating the velocity fields η_λ^\pm with 4th-order Runge-Kutta method, where the velocity at each point is approximated by linear interpolation. When we numerically integrate η_λ^\pm , following Onu and Haller [51], the orientation of η_λ^\pm at each point is reversed as required so that the solution curve becomes smooth as possible. We consider that a solution curve is closed and regard it as an elliptic LCS, if the point returns to a place within a radius of δ from its initial position. Note that we exclude some of the orbits that are collapsed or intersect with themselves.

Elliptic LCSs in the model. Fig.2.3.4 depicts the elliptic LCSs around 1 and 3-periodic points in the perturbed Hamiltonian model, where red and yellow points indicate the 1 and 3-periodic points respectively. The initial time of the LCSs is $t_0 = 0$ and the integration time is set to $T_{\text{int}} = 200T, 300T$ for those around 1 and 3-periodic points respectively. The radius for detecting closed solution curves on vector fields η_λ^\pm is $\delta = 0.001$. As can be seen in Fig.2.3.4, the elliptic LCSs appear similarly as KAM curves. This implies that KAM curves and KAM islands may correspond to elliptic LCSs and Lagrangian vortices respectively. In addition, we can see in Fig.1.1.5d and Fig.2.3.4 that elliptic LCSs appear where no hyperbolic LCSs exist. This is consistent with the fact that hyperbolic and elliptic LCSs are associated with chaotic and stable fluid transport respectively.

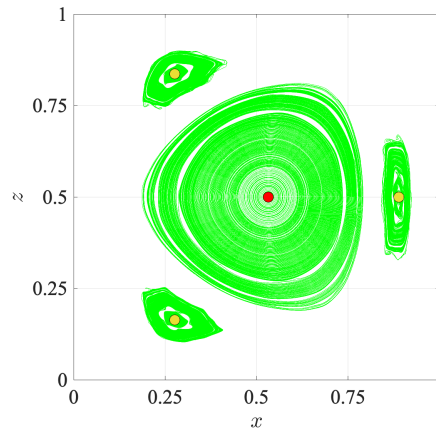


Figure 2.3.4: Elliptic LCSs and 1, 3-periodic points

2.4 Resonances of periodic orbits

In this section, we investigate the resonances of periodic orbits which is a solution curve passing through periodic points. To do this, we consider the projection of the m -periodic orbits in the extended phase space $\mathcal{M} = M \times S^1$ to the original phase space M and analyze the winding number n of the projected orbits around the center of a cell.

Periodic solutions. Let us investigate the resonance of periodic orbits by introducing a projection. Let $\tilde{c}(t) := (x(t), z(t), \theta(t))$, $t \in \mathbb{I} \subset \mathbb{R}$ be a periodic solution of the perturbed Hamiltonian system in (2.2.1), which is given by a curve on the extended phase space \mathcal{M} , and let $\pi : \mathcal{M} \rightarrow M; (x, z, \theta) \mapsto (x, z)$ be the natural projection. Then, from the periodic solution $\tilde{c}(t)$, the projected curve $c(t)$ can be defined on M as

$$c(t) := \pi(\tilde{c}(t)) = (x(t), z(t)),$$

which can be identified with the solution curve of the non-autonomous Hamiltonian system in (2.1.2) on M . From a physical point of view, projected orbits correspond to the orbits of fluid particles in the convection.

Fig.2.4.1 illustrates the projection of the 3-periodic orbit in Fig.2.3.1b by π onto M . It follows that the projection is a closed orbit and that it goes around the center of the cell $(x, z) = (1/2, 1/2)$ once.

Winding number of periodic orbits. In order to analyze the number of times that a projected periodic orbit goes around the center of a cell, let us introduce the concept of *winding number* n of a projected orbit.

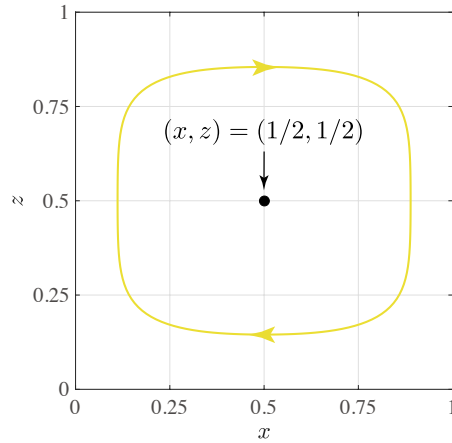


Figure 2.4.1: 3-periodic orbit projected by π on M

Definition 2.4.1. Consider an m -periodic orbit $\tilde{c}(t) := (x(t), z(t), \theta(t))$, $t \in \mathbb{I} \subset \mathbb{R}$ on the extended phase space $\mathcal{M} = M \times S^1$. Let us define a periodic curve on M by $c(t) = (x(t), z(t)) := \pi(\tilde{c}(t))$. Then, the *winding number* of $c(t)$ is given by

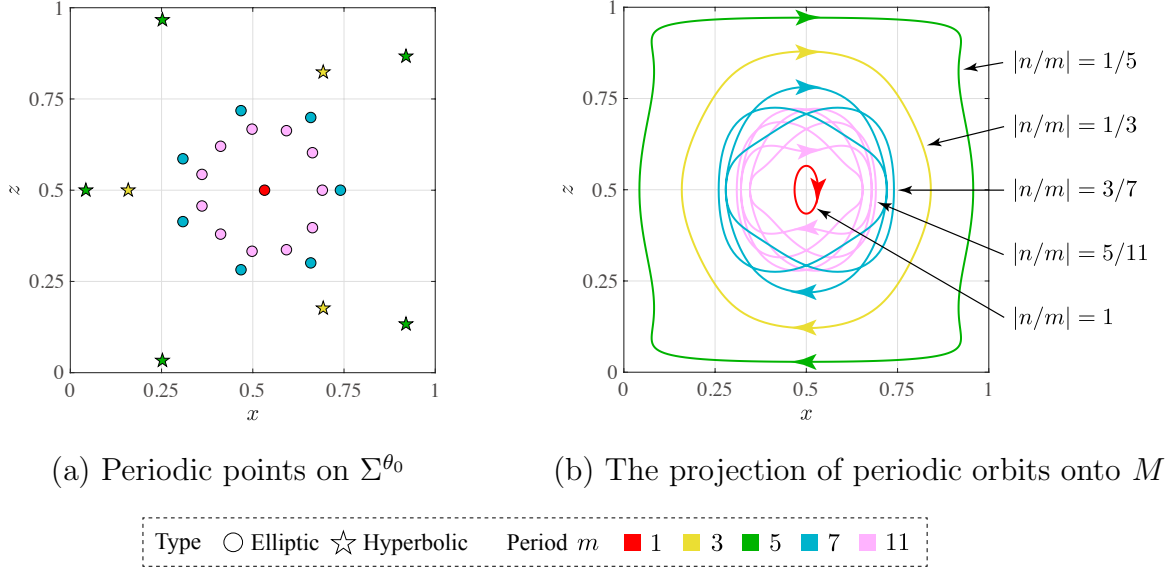
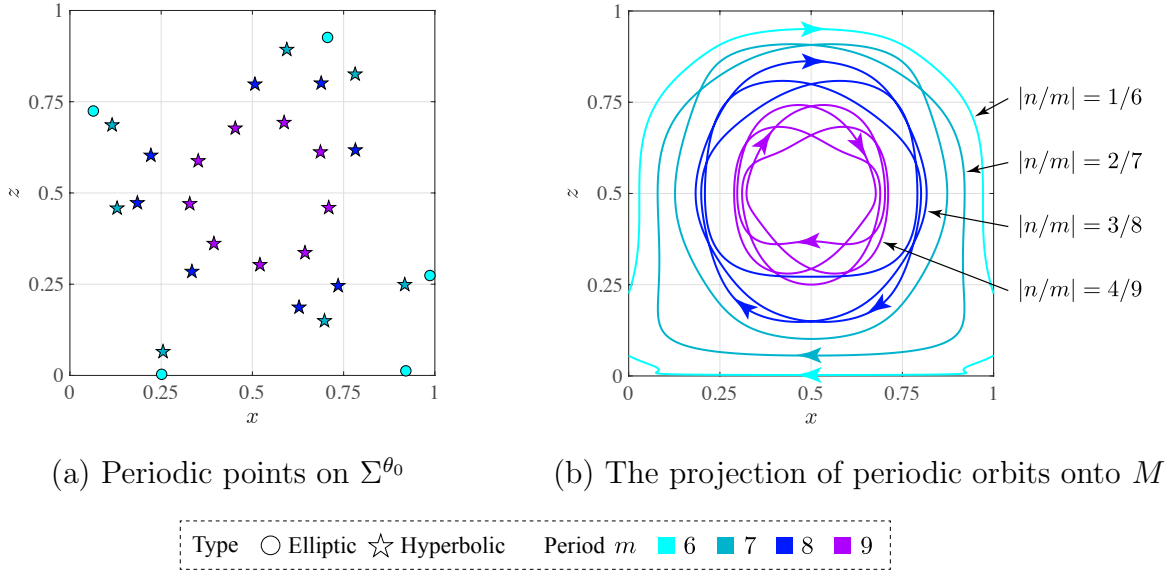
$$n = \frac{1}{2\pi i} \oint_c \frac{dw}{w - w_c}, \quad (2.4.1)$$

where $w = x + iz \in \mathbb{C}$ is a point on $c(t)$ and $w_c = x_c + iz_c \in \mathbb{C}$ is a point on M such that $w_c \notin c(t)$. Regarding the winding number, see Flanagan [20].

The absolute value of the winding number n corresponds to the number of times that the orbit goes around the center of a cell, while it could take both positive and negative values in general according to the direction. Namely, the winding number is positive when the orbit goes in counter-clockwise direction, while it is negative when it goes in clockwise direction. For example, the winding number of the projection of the 3-periodic orbit shown in Fig.2.4.1 is $n = -1$ when $x_c = z_c = 1/2$, since the orbit goes around $(x, z) = (1/2, 1/2)$ once in clockwise direction.

Resonant periodic orbits. Fig.2.4.2 – Fig.2.4.5 illustrate some of the periodic points in Fig.2.2.1 and the projection of the associated periodic curves onto M , where they are classified according to the symmetry with respect to the horizontal and vertical center lines of the cell, namely $x = \pi/(2k)$ and $z = 1/2$. As can be seen, the projected orbits go around the center of the cell once or several times. For example, the projection of the 7-periodic orbit in Fig.2.4.2 goes around the center of the cell three times in clockwise direction, which means that the winding number is $n = -3$ when $x_c = z_c = 1/2$. It follows that m -periodic orbits can be considered as *resonant orbits* in the sense that those with winding number n go around the center of a cell n times when they are projected on M , while they go around m times in θ direction in the extended phase space \mathcal{M} .

Resonance condition of periodic orbits. Let us define the *resonance condition* of an m -periodic orbit with winding number n as $|n/m|$. The resonance conditions of the detected periodic orbits are indicated besides each orbit in Fig.2.4.2 – Fig.2.4.5, where $x_c = z_c = 1/2$. Fig.2.4.2 – Fig.2.4.5 shows that there are many kinds of periodic orbits with different resonance conditions. It follows that the resonance conditions of the orbits in the middle of the cell tend to be larger than that of those in the outer area, since the absolute value of the winding number of those in the middle tend to be larger. It is also

Figure 2.4.2: Orbits symmetric with respect to $x = \pi/(2k)$ and $z = 1/2$ Figure 2.4.3: Orbits symmetric only with respect to $x = \pi/(2k)$

observed that some of the m -periodic orbits have different resonance conditions even when their periods are the same. For example, we can see two different kinds of 7-periodic orbits with $|n/m| = 3/7, 2/7$, and also 11-periodic orbits with $|n/m| = 5/11, 3/11$.

Furthermore, it is found in our numerical computation that some of the orbits have the same resonance conditions even when their periods are different. For example, we illustrate some of the orbits of which resonance condition is $|n/m| = 1/3$ in Fig.2.4.6. As can be seen, the winding number of the 9, 12, and 15-periodic orbits are $n = -3, -4, -5$ respectively, where

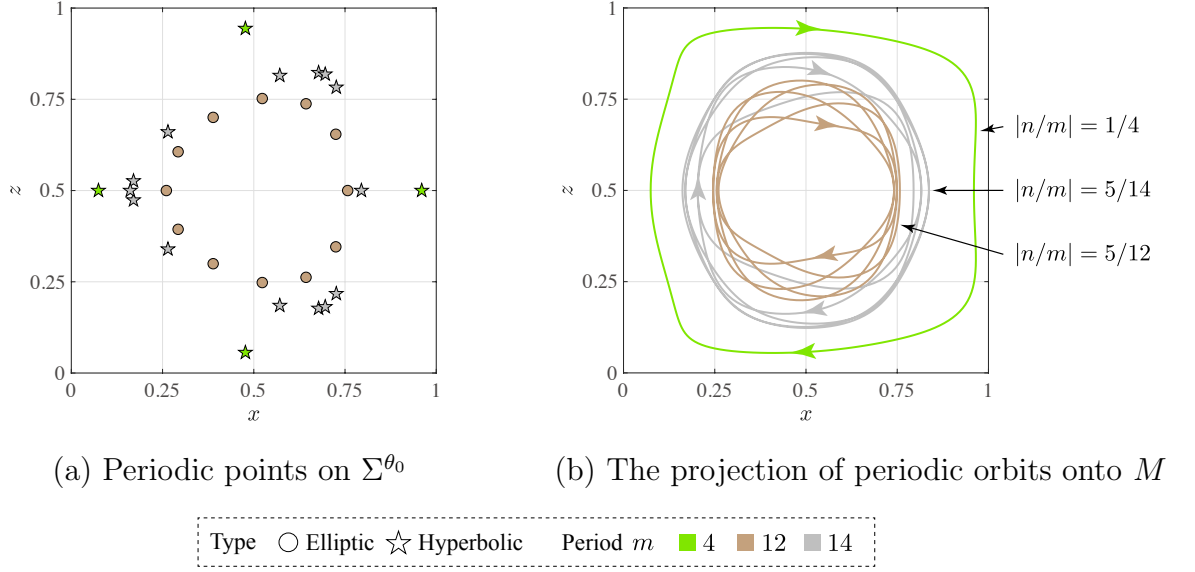
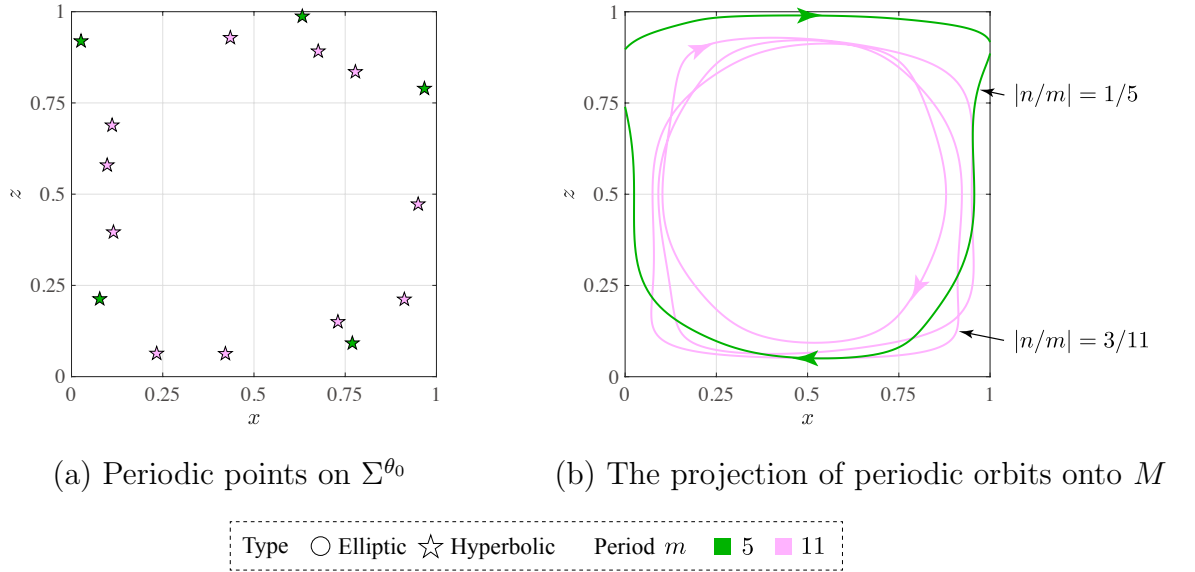
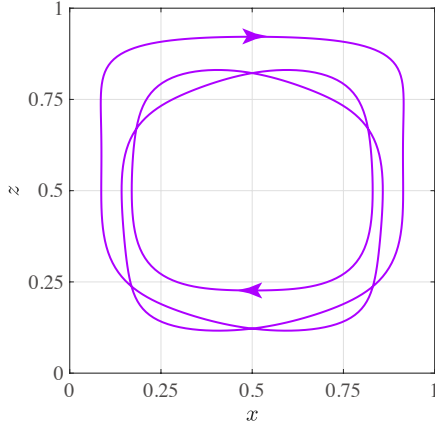
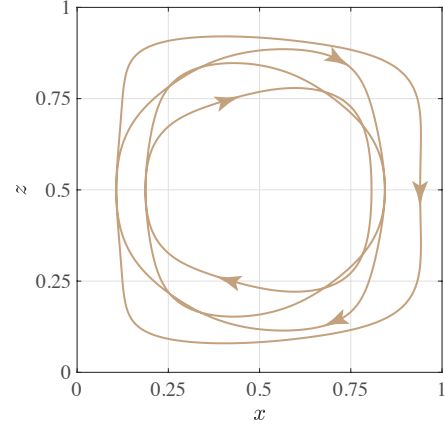
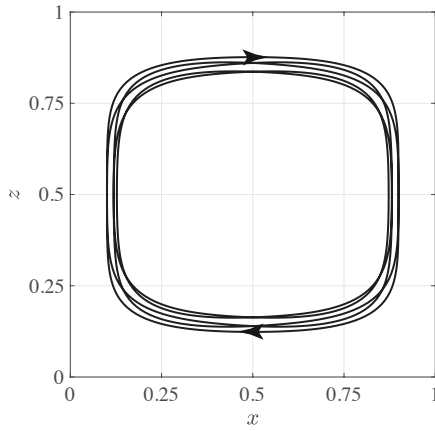
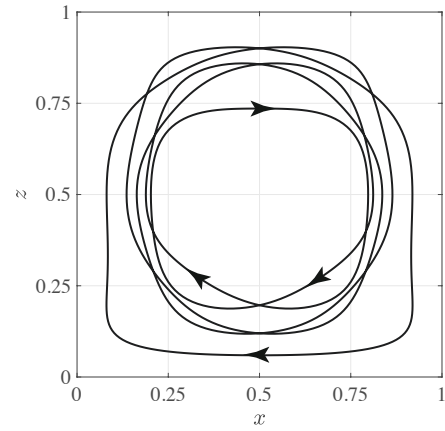

 Figure 2.4.4: Orbits symmetric only with respect to $z = 1/2$


Figure 2.4.5: Asymmetric orbits

we recall that the negative signs indicate that periodic orbits have clockwise directions. Periodic orbits with the same resonance conditions seem to be related to fold bifurcations as we shall discuss this in Chap.3.

Remark 2.4.1 (Action angle variables). We can introduce the action angle variables (J, ϕ) to transform the Hamiltonian system in terms of (x, z) to that in terms of (J, ϕ) . When the model is unperturbed, i.e., $\varepsilon = 0$, J and ϕ are obtained by

$$J = \frac{1}{2\pi} \oint z dx, \quad \phi = \frac{2\pi}{T} t,$$

(a) 9-periodic orbit ($n = -3$)(b) 12-periodic orbit ($n = -4$)(c) 15-periodic orbit ($n = -5$)(d) 15-periodic orbit ($n = -5$)Figure 2.4.6: The projection of periodic orbits with $|n/m| = 1/3$

where the integral is taken over one cycle of the periodic curve of (2.1.1) which preserves $H(x, z) = H$ (constant) and T is the period of the orbit. Then the unperturbed model (2.1.1) can be rewritten as

$$\frac{dJ}{dt} = 0, \quad \frac{d\phi}{dt} = \Lambda(J),$$

where $\Lambda(J) = 2\pi/T$. Then, the perturbed system (2.1.2) can be restated in terms of (J, ϕ) as

$$\frac{dJ}{dt} = \varepsilon f(J, \phi, t), \quad \frac{d\phi}{dt} = \Lambda(J) + \varepsilon g(J, \phi, t), \quad (2.4.2)$$

where $f(J, \phi, t) = -\frac{\partial J}{\partial x} \frac{\partial H_1}{\partial z} + \frac{\partial J}{\partial z} \frac{\partial H_1}{\partial x}$ and $g(J, \phi, t) = -\frac{\partial \phi}{\partial x} \frac{\partial H_1}{\partial z} + \frac{\partial \phi}{\partial z} \frac{\partial H_1}{\partial x}$; see, for instance, Wiggins [75].

As was shown in (2.2.1), the perturbed Hamiltonian system (2.4.2) can be written as an autonomous system in terms of $(J, \phi, \theta) \in \mathbb{R} \times S^1 \times S^1$ as

$$\begin{aligned}\frac{dJ}{dt} &= \varepsilon f(J, \phi, \theta), \\ \frac{d\phi}{dt} &= \Lambda(J) + \varepsilon g(J, \phi, \theta), \\ \frac{d\theta}{dt} &= \omega,\end{aligned}\tag{2.4.3}$$

where $\theta = \omega t + \theta_0$. Of course, the perturbed Hamiltonian system (2.2.1) with the variables (x, z, θ) is transformed into the system (2.4.3) with the action-angle variables (J, ϕ, θ) .

Remark 2.4.2 (Poincaré-Birkhoff theorem). Let us consider an invariant curve with action J such that $\Lambda(J) = n/m$ in an unperturbed Hamiltonian system, where m and n are integers. The Poincaré-Birkhoff theorem states that when the system is perturbed such curve varies to $2\ell m$ points of m -periodic points, where ℓm of them are to be elliptic and the others are to be hyperbolic. Here, ℓ is some unknown integer; see Birkhoff [3], Guckenheimer and Holmes [24], and Lichtenberg and Lieberman [43].

2.5 Symmetries of n/m -resonant orbits

In this section, we consider the symmetric properties concerning n/m -resonant orbits, namely, m -periodic orbits with winding number n . We especially consider the special case of such n/m -resonant orbits $\tilde{c}(t)$ in the extended phase space $\mathcal{M} = M \times S^1$ in which $c(t) = \pi(\tilde{c}(t))$ is symmetric with respect to the horizontal and vertical center lines of a cell, namely $x = (2a + 1)\pi/(2k)$ ($a \in \mathbb{Z}$) and $z = 1/2$, by the following theorem.

Theorem 2.5.1 (Symmetries of n/m -resonant orbits). Let

$$\tilde{c}(t) := (x(t), z(t), \theta(t)) \subset M \times S^1, \quad t \in \mathbb{I} = [0, mT]$$

be a n/m -resonant orbit such that $\tilde{c}(0) = \tilde{c}(mT) = p$, where p is an m -periodic point on Σ^{θ_0} . Then, let

$$c(t) := \pi(\tilde{c}(t))$$

be a periodic curve on M . If $c(t)$ is symmetric with respect to the horizontal and vertical center lines of a cell, namely $x = (2a + 1)\pi/(2k)$ ($a \in \mathbb{Z}$) and $z = 1/2$, the period m and the winding number n of $c(t)$ are both odd.

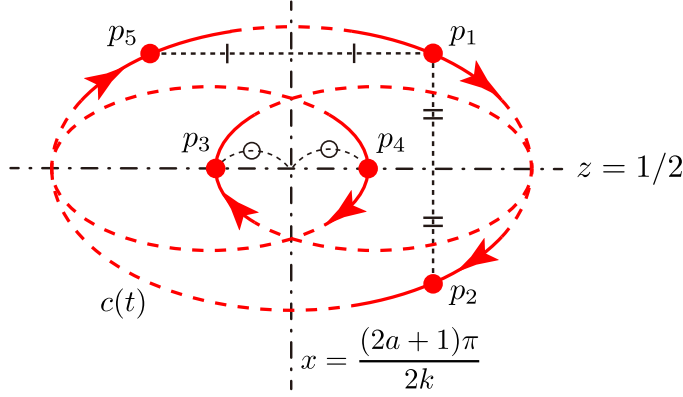


Figure 2.5.1: Points p_1, p_2, p_3 and p_4 on curve $c(t)$

Proof. For the sake of proving this theorem, recall the following symmetric properties i), iv), and v) of the non-autonomous system in (2.1.2), since $c(t) \subset M$ corresponds to the solution curve of the non-autonomous system.

$$\text{i)} \quad x \mapsto x + \frac{2a\pi}{k}, \quad z \mapsto -z + 1, \quad t \mapsto -t + bT,$$

$$\text{iv)} \quad x \mapsto -x + \frac{(2a+1)\pi}{k}, \quad z \mapsto z, \quad t \mapsto -t + \left(b + \frac{1}{2}\right)T,$$

$$\text{v)} \quad x \mapsto -x + \frac{(2a+1)\pi}{k}, \quad z \mapsto -z + 1, \quad t \mapsto t + \left(b + \frac{1}{2}\right)T,$$

As is shown in Fig.2.5.1, consider an n/m -resonant periodic orbit $\tilde{c}(t) \in M \times S^1$ such that $\tilde{c}(0) = \tilde{c}(mT) = p$, where p is an m -periodic point, and suppose that the periodic curve $c(t) = \pi(\tilde{c}(t))$ on M has the symmetric properties that $c(t)$ is symmetric with respect to $x = (2a+1)\pi/(2k)$ ($a \in \mathbb{Z}$) and $z = 1/2$. Note that $c(t)$ is partly illustrated in dashed lines to indicate a general curve in Fig.2.5.1, which denotes that the dashed lines can have a loop as long as $c(t)$ maintain the symmetric properties.

First, we shall prove that m is odd. To do this, let $p_1 := \pi(p)$, where $p_1 = c(0) = c(mT) \in M$, and let $p_2 \in M$ be the associated symmetric point with p_1 regarding the horizontal center line of a cell, namely $z = 1/2$. Since $c(t)$ is symmetric with respect to $z = 1/2$, it follows from property i) that p_2 can be expressed as $p_2 = c(\ell T)$, where ℓ is some integer such that $0 \leq \ell \leq m-1$.

We denote the initial time for p_1 and p_2 by $t_1 = 0$ and $t_2 = \ell T$ respectively. Then, one can define an intermediate point p_3 in a path from p_1 to p_2 such

that $p_3 := c(t_3)$, where

$$t_3 = \frac{t_1 + t_2}{2} = \frac{\ell}{2}T$$

is the middle time between t_1 and t_2 . Further, we denote the first return time for p_1 as $t'_1 = mT$. Then, one can define an intermediate point p_4 in a path from p_2 to p_1 such that $p_4 := c(t_4)$, where

$$t_4 = \frac{t_2 + t'_1}{2} = \frac{\ell + m}{2}T$$

is the middle time between t_2 and t'_1 . Since p_1 and p_2 are the points of curve $c(t)$ at $t \equiv 0 \pmod{T}$ and that they are symmetric with respect to $z = 1/2$, it follows from property i) that p_3 and p_4 lie on the horizontal center line $z = 1/2$, as is shown in Fig.2.5.1.

Next, let $p_5 \in M$ be the associated symmetric point with p_1 regarding the vertical center line of a cell, namely $x = (2a + 1)\pi/(2k)$. Since $c(t)$ is symmetric with respect to the vertical center line, p_5 is a point of $c(t)$. Furthermore, it follows from property v) that the time from p_2 to p_5 is the half of the period of the orbit, namely $mT/2$, since p_2 and p_5 are symmetric with respect to point $(x, z) = ((2a+1)\pi/(2k), 1/2)$. Thus, p_5 can be expressed as $p_5 = c(t_5)$, where

$$t_5 = t_2 + \frac{mT}{2} = \left(\ell + \frac{m}{2}\right)T.$$

Then, the times from p_1 to p_3 and p_4 to p_5 become the same as is shown below.

$$t_3 - t_1 = t_5 - t_4 = \frac{\ell}{2}T$$

Since p_1 and p_5 are symmetric with respect to the vertical center line, it follows from property iv) that p_3 and p_4 are also symmetric with respect to the vertical center line, as is shown in Fig.2.5.1.

Now, we prove by contradiction that period m is an odd number. To do this, let us assume that m is an even number. Then, time t_3 and t_4 become $t_3 \equiv t_4 \equiv 0$ when ℓ is even, while they become $t_3 \equiv t_4 \equiv T/2$ when ℓ is odd. However, since p_3 and p_4 are symmetric with respect to $x = (2a + 1)\pi/(2k)$, it follows from property iv) that there are only two cases; One is the case when $t_3 \equiv 0$ and $t_4 \equiv T/2$, and the other is the case when $t_3 \equiv T/2$ and $t_4 \equiv 0$. Therefore, the assumption that m is an even number is not correct. Thus, it is proved that m is an odd number.

Next, we shall prove that n is odd. Recall that the winding number n of a periodic orbit $c(t)$ is given by (2.4.1), where $c(t)$ is regarded as a closed

curve $c(t) = x(t) + iz(t)$ in \mathbb{C} and the interval of integration can be divided as

$$\begin{aligned} n &= \frac{1}{2\pi i} \oint_{c(t)} \frac{dw}{w - w_c} \\ &= \frac{1}{2\pi i} \left(\int_{c_{3,4}(t)} \frac{dw}{w - w_c} + \int_{c_{4,3}(t)} \frac{dw}{w - w_c} \right). \end{aligned}$$

Here, $c_{3,4}(t)$ and $c_{4,3}(t)$ respectively denote the part of curve $c(t)$ from p_3 to p_4 and vice versa. From assumption, note that $c(t)$ is symmetric with respect to $z = 1/2$ and also that p_3 and p_4 lie on $z = 1/2$, and it follows

$$\int_{c_{3,4}(t)} \frac{dw}{w - w_c} = \int_{c_{4,3}(t)} \frac{dw}{w - w_c},$$

where $w = x + iz$ is an arbitrary point on $c(t)$ and $(x_c, z_c) = ((2a + 1)\pi/(2k), 1/2)$ is set as a fixed point. Therefore,

$$\begin{aligned} n &= \frac{1}{\pi i} \int_{c_{3,4}(t)} \frac{dw}{w - w_c} \\ &= \frac{1}{\pi i} \{ \ln(w(t_4) - w_c) - \ln(w(t_3) - w_c) \}. \end{aligned}$$

Now, we rewrite a point $w = x + iz$ on $c(t)$ in the polar coordinates as

$$w(t) - w_c = r(t)e^{i\psi(t)},$$

where $r = |w| = \sqrt{(x - x_c)^2 + (z - z_c)^2} \geq 0$ and $\psi = \arg w = \arctan\left(\frac{z - z_c}{x - x_c}\right)$. Since p_3 and p_4 lie on $z = 1/2$ and are symmetric with each other with respect to $x = (2a + 1)\pi/(2k)$,

$$\begin{aligned} r(t_3) &= r(t_4), \\ |\psi(t_4) - \psi(t_3)| &= \pi, \end{aligned}$$

Therefore,

$$\begin{aligned} n &= \frac{1}{\pi i} \{ \ln r(t_4) + i(\psi(t_4) + 2\ell'\pi) - \ln r(t_3) - i(\psi(t_3) + 2\ell''\pi) \} \\ &= 2(\ell' - \ell'') \pm 1, \end{aligned}$$

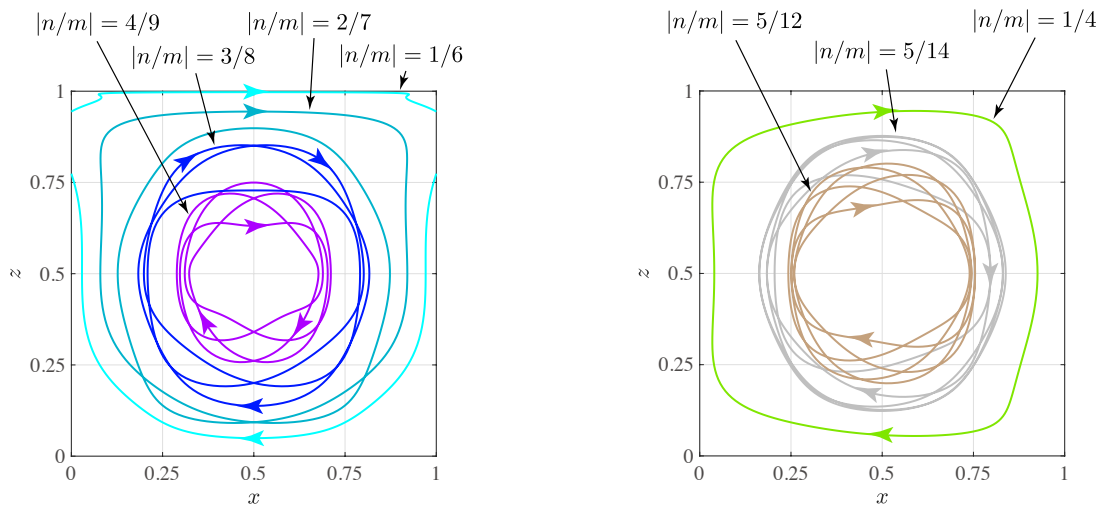
where $\ell', \ell'' \in \mathbb{Z}$. Hence, it is proved that n is an odd number. Thus, theorem is proved. ■

As the theorem states, we can see in Fig.2.4.2b that the periodic orbits of which projection is symmetric with respect to the horizontal and vertical center lines of the cell have odd period m and winding number n . Furthermore, the following corollary can be stated from Theorem 2.5.1.

Corollary 2.5.2. If the period m or the winding number n of a periodic orbit $\tilde{c}(t)$ is an even number, there appear one or three more n/m -resonant orbits of which projection is symmetric with $c(t) = \pi(\tilde{c}(t))$ with respect to either horizontal or vertical center lines, or the center point of a cell.

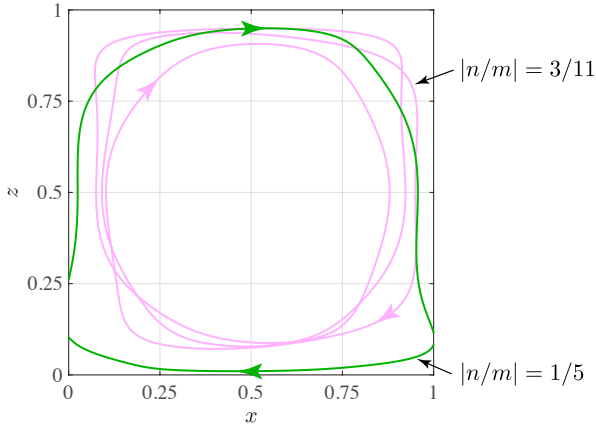
Proof. Considering the contraposition of Theorem 2.5.1, if m or n is an even number, $c(t) = \pi(\tilde{c}(t))$ is not symmetric with respect to either horizontal or vertical center lines of a cell. If $c(t)$ is not symmetric with only one of the two lines, it follows from property i) or iv) that there appear one more orbit of which projection is symmetric with $c(t)$. If $c(t)$ is not symmetric with both of the two lines, it follows from property i) and iv) that there appear two more orbits $\tilde{c}_1(t)$ and $\tilde{c}_2(t)$ of which projection is symmetric with $c(t)$ with respect to either of the two lines, and in addition another orbit $\tilde{c}_3(t)$ of which projection is symmetric with $c(t)$ with respect to the center point of the cell. Thus, the corollary is proved. ■

Fig.2.5.2 and Fig.2.5.3 illustrate the projection of orbits of which period m or winding number n is an even number. When we look at them with Fig.2.4.3 – Fig.2.4.5, it is observed that there appear one or three more n/m -resonant orbits. Note that the evolution of the orbits in Fig.2.5.2 and Fig.2.5.3 are depicted in the positive direction of time t in both figures and also that the orientation of orbits could be opposite when computing the evolution for the negative direction of t , while the resonance conditions of the orbits that are symmetric in spatial coordinates (x, z) with each other are the same.

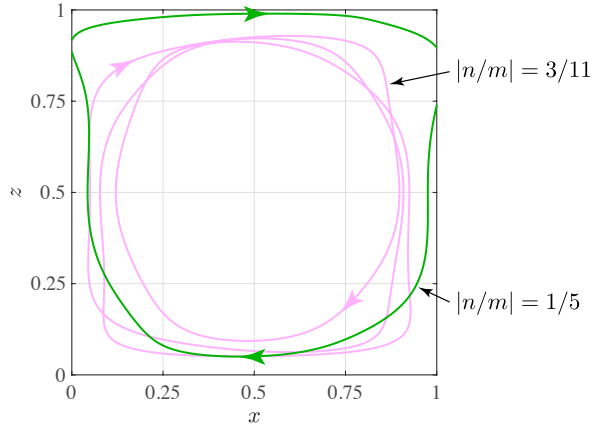


(a) Orbits symmetric with those in Fig.2.4.3 (b) Orbits symmetric with those in Fig.2.4.4

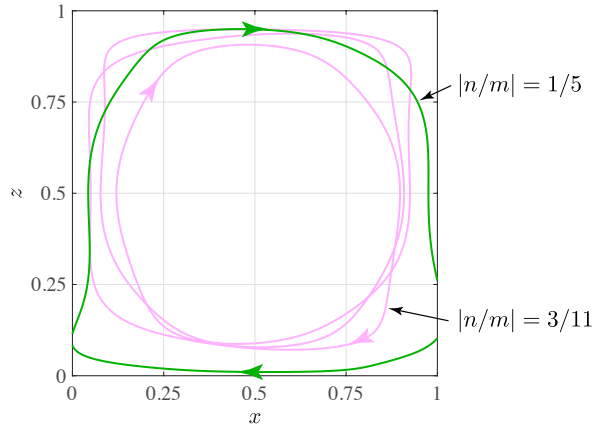
Figure 2.5.2: Orbits symmetric with those in Fig.2.4.3 and Fig.2.4.4



(a) Orbits symmetric with respect to $z = 1/2$



(b) Orbits symmetric with respect to $x = \pi/(2k)$



(c) Orbits symmetric with respect to $(x, z) = (\pi/(2k), 1/2)$

Figure 2.5.3: Orbits symmetric with those in Fig.2.4.5

2.6 Summary

In this chapter, we first describe the two-dimensional perturbed Hamiltonian model of Rayleigh-Bénard convection, which is a non-autonomous system on phase space $M = \mathbb{R} \times U$. Then, the model is extended to an autonomous system by introducing the extended phase space $\mathcal{M} = M \times S^1$ in order to define a Poincaré map. Next, elliptic and hyperbolic periodic points on the Poincaré section are numerically detected and the structures of periodic orbits are investigated. It is shown that KAM tori in the extended phase space \mathcal{M} appear around the orbits of elliptic periodic points and generally have twisted structures. From a physical point of view, this implies that each region of KAM islands may be transported stably as a sort of vortex in the Lagrangian description. In addition, KAM curves and KAM islands

may correspond to elliptic LCSs and Lagrangian vortices respectively, since elliptic LCSs appear similarly as KAM curves. Further, the symmetries and resonances of periodic orbits are explored by projecting the orbits in the extended phase space \mathcal{M} onto the original phase space M . In particular, we propose and prove a theorem that the period m and the winding number n of a periodic orbit are both odd if the projection of the orbit is symmetric with respect to the horizontal and vertical center lines of a cell.

Chapter 3

Bifurcations of periodic orbits in a model

As already mentioned, the amplitude of perturbations in Rayleigh-Bénard convection increases when Rayleigh number Ra is gradually raised from a critical number Ra_t by increasing the temperature difference between the top and bottom planes. In this chapter, we study the bifurcations of periodic orbits in the perturbed Hamiltonian system by varying parameter ε , i.e., the amplitude of perturbation, in order to clarify how the transport becomes complicated when Ra is increased. We first describe the ε -parameter bifurcation diagrams of m -periodic points and then clarify the structures of bifurcations associated with the main KAM island I_1 and the surrounding islands I_2, I_3 , and I_4 , and furthermore those associated with other islands.

3.1 Structures of ε -parameter bifurcation

Computation of ε -parameter bifurcation diagrams. In the numerical computations in Chap.2, we have analyzed the periodic points and the associated orbits when the amplitude ε of the perturbation is set to $\varepsilon = 0.1$. In order to obtain the ε -parameter bifurcation diagram of the periodic points for $0 < \varepsilon \leq 0.5$, we shall compute to detect the elliptic and hyperbolic periodic points on the Poincaré section for each amplitude of perturbation $\varepsilon = 0.001, 0.002, \dots, 0.5$ independently by Newton's method shown in §2.2. The other parameters of the convection and the initial condition of θ are set to $A = \pi, k = \pi, T = 1/\pi$, and $\theta_0 = 0$ as the same in Fig.2.2.1. For numerical computations of bifurcation diagrams in fluids continuation methods are used in other studies; see for instance Umbriá and Net [69]. However, in this thesis we obtain the bifurcation diagram by the above methods, since the Hamiltonian $H(x, z, t) = H_0(x, z) + \varepsilon H_1(x, z, t)$ of the model in this study is

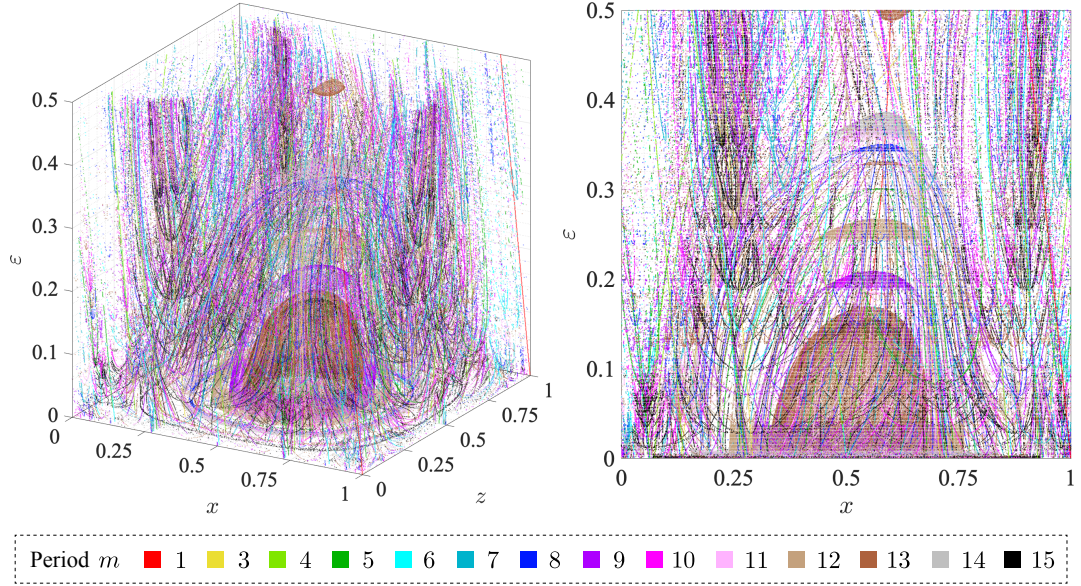


Figure 3.1.1: ε -parameter bifurcation diagram of periodic points

given, and thus the velocity fields $dx/dt = -\partial H/\partial z$, $dz/dt = \partial H/\partial x$ for each ε can be obtained explicitly. Fig.3.1.1 shows the detected bifurcation diagram from diagonal and z direction, where the periodic points with period $m \leq 15$ are depicted. Note that the computations are conducted independently for each ε . The color of the plots indicate the period m of each point, however the types of the points, namely elliptic or hyperbolic, are not illustrated in Fig.3.1.1. We will depict them in the figures shown latter.

Periodic points on Poincaré section with some parameters ε . Before we take a look at the bifurcation diagram let us show how the Poincaré maps and the detected periodic points vary with the amplitude ε of the perturbation. Fig.3.1.2 illustrates the image of the Poincaré section by Poincaré map $P_\varepsilon^{\theta_0}$ and the periodic points for $\varepsilon = 0.2, 0.3, 0.4, 0.5$. As can be seen, the islands of KAM tori, which correspond to stable transport regions, exist for a while when ε is increased. However, when we increase it furthermore, the area of the islands and the number of elliptic periodic points gradually decrease. Especially, islands I_2, I_3 and I_4 seem to disappear by $\varepsilon = 0.5$. In contrast, it is apparent that the area of chaotic regions increases. This denotes that the periodic orbits in the system of (2.2.1) bifurcate one after another and lead to chaotic orbits when ε is increased.

Bifurcations of 1 and 3-periodic points. Now we take a closer look at the bifurcation diagram detected in our numerical computation. Since it is too complicated to understand the structure of the diagram from Fig.3.1.1, let

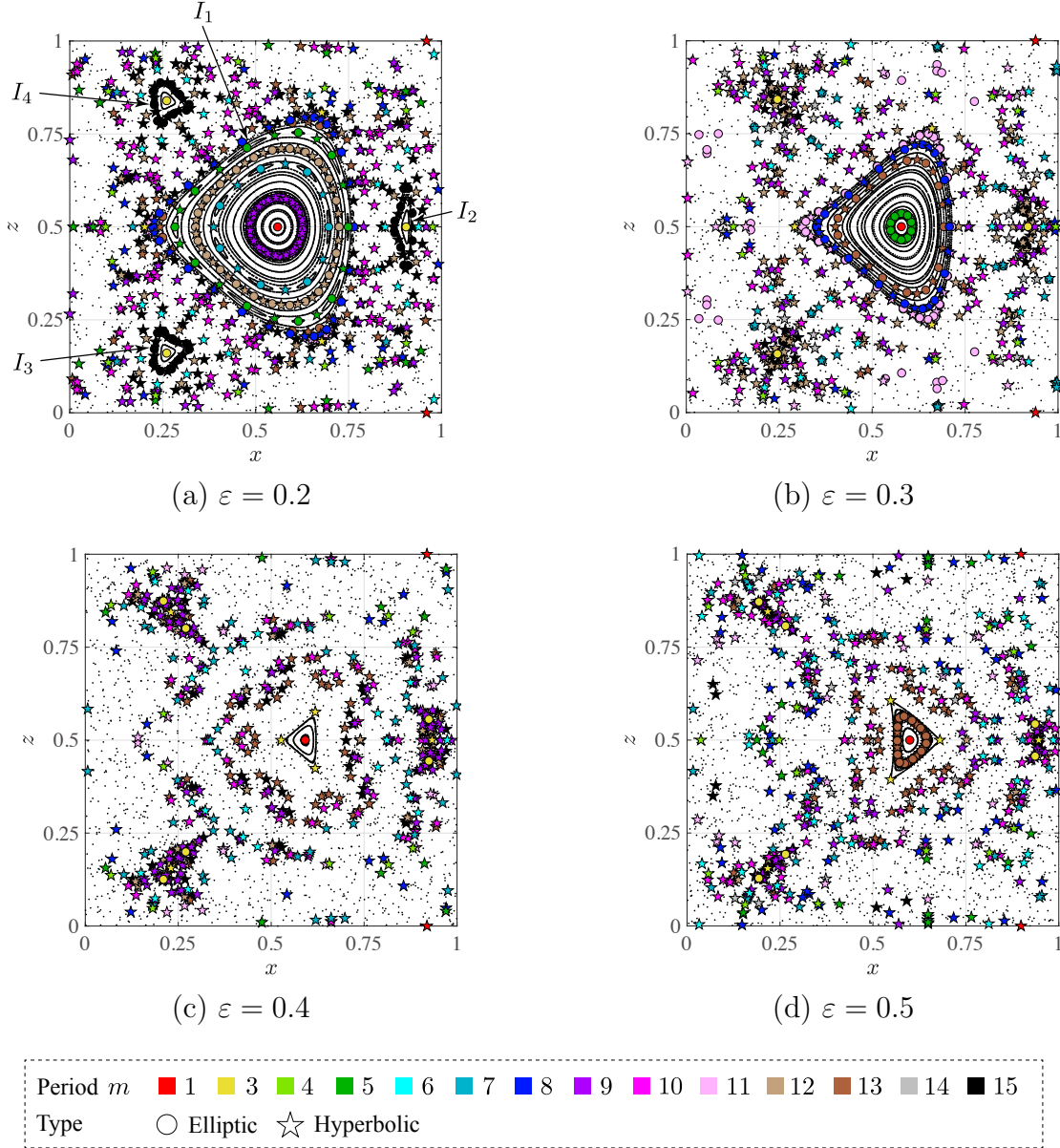
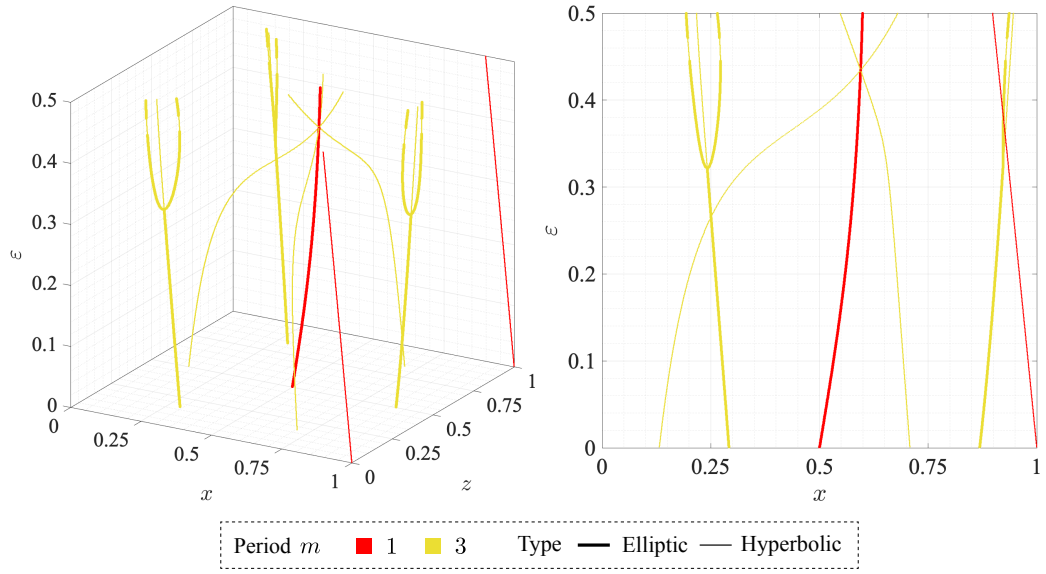
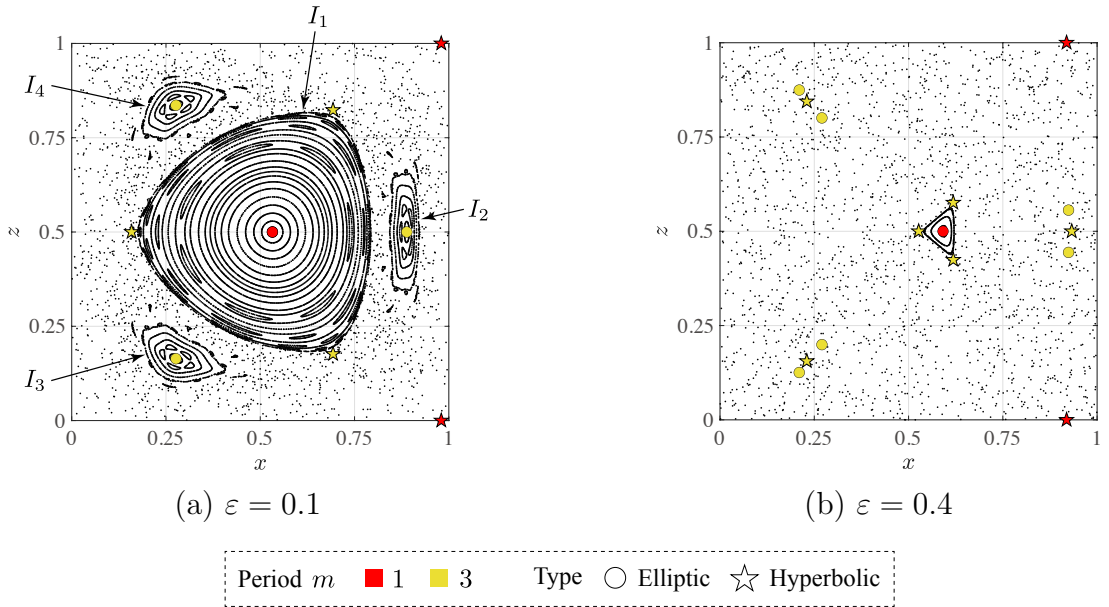


Figure 3.1.2: Elliptic and hyperbolic periodic points ($\varepsilon = 0.2, 0.3, 0.4, 0.5$)

us first focus on the bifurcations of 1 and 3-periodic points, which are illustrated in Fig.3.1.3 from diagonal and z direction. Here, the branches of elliptic and hyperbolic periodic points are depicted in thick and thin lines respectively. In addition, we especially depict the 1 and 3-periodic points with the image of the Poincaré section at $\varepsilon = 0.1, 0.4$ in Fig.3.1.4 so that we can clearly see the periodic points. As is shown in Fig.3.1.4, an elliptic 1-periodic point and three hyperbolic 3-periodic points appear at the center and the corners of the main island I_1 respectively.

Thus, the thick red branch of elliptic 1-periodic points in the middle of Fig.3.1.3 and the three thin yellow branches of hyperbolic 3-periodic points,

Figure 3.1.3: ε -parameter bifurcation diagram of 1 and 3-periodic pointsFigure 3.1.4: 1 and 3-periodic points at $\varepsilon = 0.1, 0.4$

which cross with the red branch, correspond to those of the periodic points associated with I_1 . Furthermore, Fig. 3.1.4 indicates that an elliptic 3-periodic point appear in the middle of each island I_2, I_3 , and I_4 when ε is small but vary to two elliptic and one hyperbolic 3-periodic points when ε is increased. Thus, the three fork-shaped branches of elliptic 3-periodic points in Fig. 3.1.3 correspond to those of the periodic points associated with islands I_2, I_3 , and I_4 . The two straight branches of hyperbolic 1-periodic points on the wall of Fig. 3.1.3 are those of the 1-periodic points on the upper and lower boundaries of the convection.

Bifurcations associated with KAM islands I_1, I_2, I_3 , and I_4 . Next, we focus on the bifurcations associated with KAM islands I_1, I_2, I_3 , and I_4 . First, we take a look at those of the main island I_1 . As is shown in Fig.3.1.2, the periodic points in I_1 appear along the KAM curves around an elliptic 1-periodic point. Thus, the mountainous structure depicted in Fig.3.1.5 may correspond to the bifurcations associated with I_1 . Though the type of the periodic points are not illustrated here, it follows that many branches of various periods gather to the branch of the elliptic 1-periodic points. Especially, it is observed that

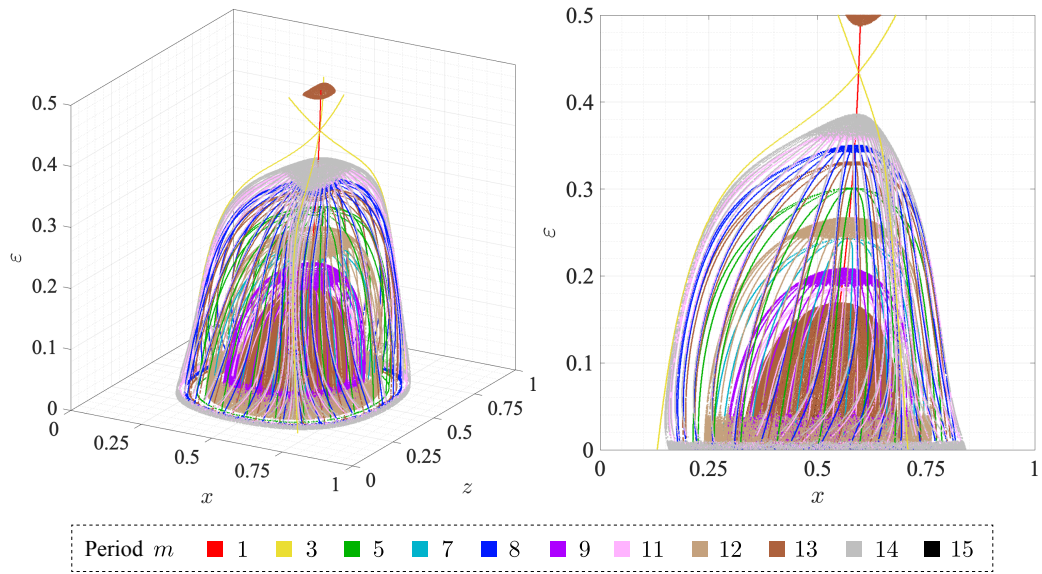


Figure 3.1.5: Mountainous structure in bifurcations of island I_1

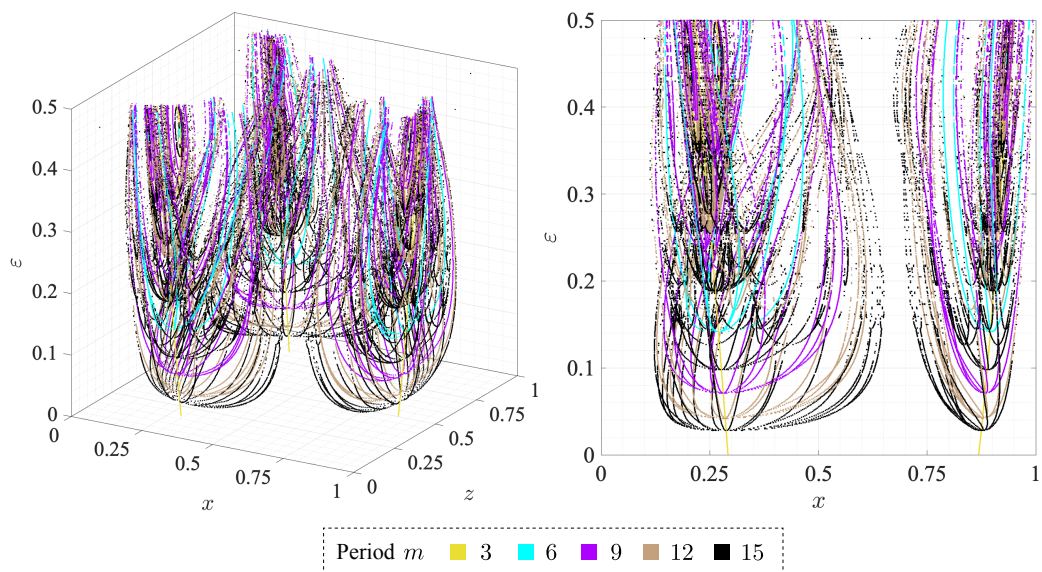


Figure 3.1.6: Bifurcations associated with island I_2, I_3 , and I_4

the three branches of hyperbolic 3-periodic points at the corners of island I_1 appear around the outer side of the mountainous structure. Furthermore, since they cross with the branch of 1-periodic points at around $\varepsilon = 0.432$, it seems that I_1 once disappear when the amplitude ε is increased. We will analyze the bifurcations associated with I_1 more in detail in §3.3. Then, let us take a look at the bifurcations of islands I_2, I_3 , and I_4 . It is found in our numerical computation that the bifurcations shown in Fig.3.1.6 may correspond to those associated with I_2, I_3 , and I_4 . As can be seen, many branches of $3l$ -periodic points ($l = 2, 3, 4, 5$) grow from the fork-shaped branch of 3-periodic points to form the shapes of three broom tips standing upside down as in Fig.3.1.3 and create three tree-like structures. We will clarify the structure of the bifurcations more in detail in §3.4.

3.2 Numerical methods for detecting bifurcation points

Before we clarify the global structures of the ε -parameter bifurcation diagram more in detail, let us briefly review the classification of bifurcations of periodic points and describe how each bifurcation point is detected in numerical computations.

Classification of bifurcation points. Recall that multipliers μ of an m -periodic point are eigenvalues of the Jacobian matrix of the Poincaré m -return map

$$J_\varepsilon(\mathbf{x}) = \left. \frac{\partial (P_\varepsilon^{\theta_0})^m(\mathbf{x})}{\partial \mathbf{x}} \right|_{\mathbf{x}=\mathbf{x}_0},$$

where \mathbf{x}_0 indicates the m -periodic point. According to the multipliers μ of the m -periodic point at the bifurcation point (see, for instance, Kuznetsov [41]), the bifurcations of m -periodic points are classified into the following types:

- Fold bifurcation (also called, tangent or saddle-node bifurcation): $\mu = 1$
- Flip bifurcation (also called, period-doubling bifurcation): $\mu = -1$
- Neimark-Sacker bifurcation (also called, Hopf bifurcation for maps):
 $|\mu|=1$ but $\mu \neq \pm 1$

In this thesis, we mainly focus on the fold and flip bifurcations.

Computation of fold and flip bifurcation points. We shall show the numerical methods for detecting the fold and flip bifurcation point of m -periodic points. To do this, we shall employ the numerical computation method that was developed by Tsumoto et al. [68]; see also Kuznetsov [41]. As already mentioned, we do not use the continuation methods in other studies, since the Hamiltonian is given in this study, and thus the velocity fields for each amplitude ε can be obtained explicitly. Using the Poincaré map $P_\varepsilon^{\theta_0} : \Sigma^{\theta_0} \rightarrow \Sigma^{\theta_0}$, the following two conditions have to be satisfied at the bifurcation point for some m -periodic point \mathbf{x}_0 :

- (i) **Condition for m -periodic points.** Recall that associated with the vector field of the autonomous Hamiltonian system in (2.2.1), we can uniquely define the flow $\phi^\varepsilon : \mathbb{R} \times \mathcal{M} \rightarrow \mathcal{M}; (t, x_0, z_0, \theta_0) \rightarrow (x_t, z_t, \theta_t) = \phi^\varepsilon(t, x_0, z_0, \theta_0)$ for some given parameter $\varepsilon \in \mathbb{R}^+$. Then, a diffeomorphism $\phi_t^\varepsilon : \mathcal{M} \rightarrow \mathcal{M}; (x_0, z_0, \theta_0) \mapsto (x_t, z_t, \theta_t) = \phi_t^\varepsilon(x_0, z_0, \theta_0)$ can be given for each fixed t .

Recall also that we can define the Poincaré m -return map by

$$(P_\varepsilon^{\theta_0})^m := \phi_{mT}^\varepsilon \Big|_{\Sigma^{\theta_0}} : \Sigma^{\theta_0} \rightarrow \Sigma^{\theta_0},$$

which is locally given by

$$\begin{aligned} (x(0) = x_0, z(0) = z_0, \theta(0) = \theta_0) \\ \mapsto (x(mT), z(mT), \theta(mT) = \theta_0 + 2\pi m \equiv \theta_0). \end{aligned}$$

Therefore, the condition that some point $\mathbf{x}_0 = (x_0, z_0) \in \Sigma^{\theta_0}$ becomes the m -periodic point is given by

$$(P_\varepsilon^{\theta_0})^m(\mathbf{x}_0) = \mathbf{x}_0. \quad (3.2.1)$$

- (ii) **Condition for bifurcation points.** Suppose that \mathbf{x}_0 is an m -periodic point on Σ^{θ_0} and consider to find a bifurcation point for \mathbf{x}_0 associated with the parameter ε , where we need to vary ε to detect the bifurcation point. Recall that the Poincaré m -return map is given by, for some $\mathbf{x}^{(\ell)} \in \Sigma^{\theta_0}$ and with fixed ε ,

$$\mathbf{x}^{(\ell+1)} = (P_\varepsilon^{\theta_0})^m(\mathbf{x}^{(\ell)}), \quad \ell = 0, 1, 2, \dots$$

Let $\mathbf{x}_0 = (x_0, z_0) \in \Sigma^{\theta_0}$ be an m -periodic solution and we define the variation of $\mathbf{x}^{(\ell)}$ associated with \mathbf{x}_0 , i.e., a small deviation from \mathbf{x}_0 by

$$\mathbf{w}^{(\ell)} := \mathbf{x}^{(\ell)} - \mathbf{x}_0.$$

Then, by definition $\mathbf{x}^{(\ell+1)} = \mathbf{x}_0 + \mathbf{w}^{(\ell+1)}$, and it follows by Tayler expansion and by neglecting the higher-order terms that the variational equations may be given as

$$\mathbf{w}^{(\ell+1)} = J_\varepsilon(\mathbf{x}_0) \mathbf{w}^{(\ell)}, \quad (3.2.2)$$

where

$$J_\varepsilon(\mathbf{x}_0) = \left. \frac{\partial (P_\varepsilon^{\theta_0})^m(\mathbf{x})}{\partial \mathbf{x}} \right|_{\mathbf{x}=\mathbf{x}_0}.$$

The characteristic equation of (3.2.2) is

$$\det (J_\varepsilon(\mathbf{x}_0) - \mu \mathbf{I}) = 0, \quad (3.2.3)$$

where \mathbf{I} denotes the unit matrix and μ a multiplier that corresponds to an eigenvalue.

Notice that the parameter ε is fixed in equations (3.2.1), (3.2.2) and (3.2.3). On the other hand, the m -periodic point may be bifurcated at some ε_0 when μ satisfy $|\mu| = 1$; for instance, the fold and flip bifurcations can be occurred when $\mu = 1$ and $\mu = -1$ respectively.

Thus, when a bifurcation associated with some specific $\mu_0 \in \mathbb{R}^+$ for an m -periodic point $\mathbf{x}_0 = (x_0, z_0) \in \Sigma^{\theta_0}$ occurs at some ε_0 , the following set of μ_0 -dependent nonlinear algebraic equations (3.2.1) and (3.2.3) holds:

$$G_{\mu_0}(\mathbf{x}_0, \varepsilon_0) = \begin{bmatrix} F(\mathbf{x}_0, \varepsilon_0) \\ g_{\mu_0}(\mathbf{x}_0, \varepsilon_0) \end{bmatrix} = \mathbf{0}, \quad (3.2.4)$$

where we define the map $F : \Sigma^{\theta_0} \times \mathbb{R}^+ \longrightarrow \mathbb{R}^2$ by, for each $(\mathbf{x}_0, \varepsilon_0) \in \Sigma^{\theta_0} \times \mathbb{R}^+$,

$$F(\mathbf{x}_0, \varepsilon_0) := \mathbf{x}_0 - (P_{\varepsilon_0}^{\theta_0})^m(\mathbf{x}_0),$$

and also the map $g_{\mu_0} : \Sigma^{\theta_0} \times \mathbb{R}^+ \longrightarrow \mathbb{R}$ by

$$g_{\mu_0}(\mathbf{x}_0, \varepsilon_0) := \det (J_{\varepsilon_0}(\mathbf{x}_0) - \mu_0 \mathbf{I}).$$

In the above, notice that ε_0 is treated as a variable together with \mathbf{x}_0 . In other words, in order to detect a bifurcation point associated with some μ_0 that satisfies $|\mu_0| = 1$ for the m -periodic point \mathbf{x}_0 together with the specific parameter ε_0 , we have to find a solution $(\mathbf{x}_0, \varepsilon_0)$ that satisfies the nonlinear algebraic equations (3.2.4).

For numerical computations, we shall employ Newton's method again as follows.

Numerical algorithm for detecting a fold or flip bifurcation point:

- (1) Set $\mu_0 = 1$ for a fold bifurcation or $\mu_0 = -1$ for a flip bifurcation.
- (2) Set $k = 0$ with an initial approximation $\mathbf{y}_0^{(0)} = (\mathbf{x}_0^{(0)}, \varepsilon_0^{(0)})$ for some required bifurcation point $\mathbf{y}_0 = (\mathbf{x}_0, \varepsilon_0)$.
- (3) Set $k := k + 1$ and compute the k -th approximation by

$$\mathbf{y}_0^{(k)} := \mathbf{y}_0^{(k-1)} - \left(\frac{\partial G_{\mu_0}(\mathbf{y}_0)}{\partial \mathbf{y}_0} \bigg|_{\mathbf{y}_0 = \mathbf{y}_0^{(k-1)}} \right)^{-1} G_{\mu_0}(\mathbf{y}_0^{(k-1)}),$$

where the Jacobian matrix is numerically approximated by the central difference scheme.

- (4) If $|G_{\mu_0}(\mathbf{y}_0^{(k)})| < \delta$, where the convergence radius is set to $\delta = 10^{-10}$, then the computation ends up and the bifurcation point for the m -periodic point is to be detected as $\mathbf{y}_0 = \mathbf{y}_0^{(k)}$.
- (5) Otherwise, return to (3) in order to iterate the computation until convergence.

Remark 3.2.1. The initial approximation $\mathbf{y}_0^{(0)} = (\mathbf{x}_0^{(0)}, \varepsilon_0^{(0)})$ in the Newton's method is obtained from the ε -parameter bifurcation diagram.

3.3 Bifurcations associated with KAM island I_1

In this section, we investigate the bifurcations of periodic points associated with the main KAM island I_1 . As we have seen in Fig.3.1.5, many branches of periodic points with various periods gather to the branch of 1-periodic points at the center of island I_1 . Let us first show the bifurcation points numerically detected in our computation, and then illustrate how the periodic orbits vary with ε by taking a look at the 7-periodic orbits for example.

Fold bifurcations associated with I_1 . Fig.3.3.1 shows from z direction the bifurcation points numerically detected in the ε -parameter bifurcation diagram associated with I_1 , where the branches of elliptic and hyperbolic periodic points are depicted in the same way. Each bifurcation point of m -periodic

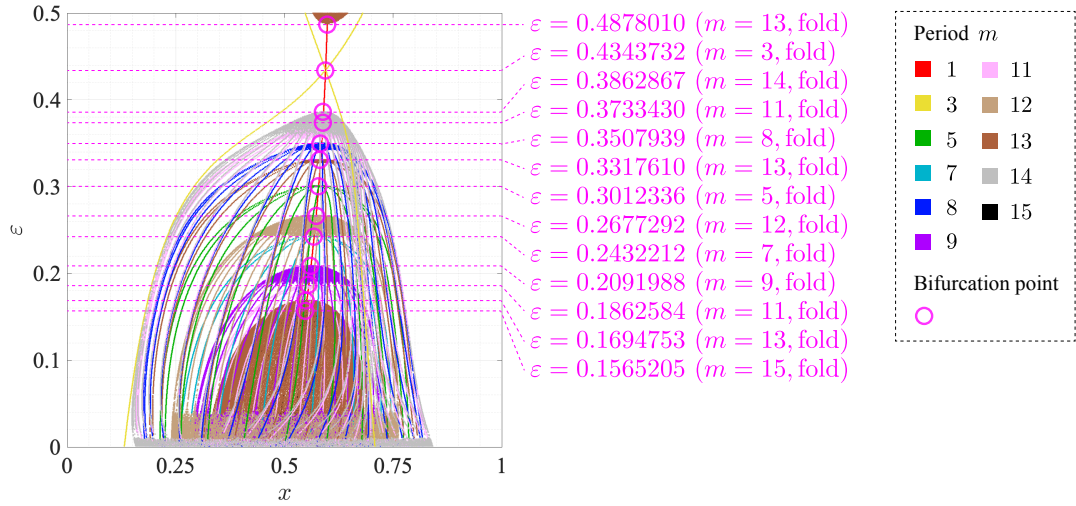


Figure 3.3.1: Bifurcation diagram of periodic points associated with I_1

points is indicated with a circle in magenta. The amplitude ε for each point is also shown beside them with the period m and the type of the bifurcation. As can be seen, it was numerically clarified that the m -periodic points bifurcate in a fold bifurcation when they coalesce with the 1-periodic point at the center of I_1 . Note that the 1-periodic points themselves do not seem to bifurcate when the m -periodic points bifurcate in a fold bifurcation.

Fold bifurcations of 7-periodic points. Next, let us investigate how the periodic orbits vary with ε near the fold bifurcation point. Here, we take a look at the 7-periodic orbits for example. Fig.3.3.2 illustrates the ε -parameter bifurcation diagram of 1 and 7-periodic points in I_1 , where the branches of elliptic and hyperbolic periodic points are depicted in thick and thin lines respectively. Fig.3.3.3 also shows the 1 and 7-periodic points on the Poincaré section Σ^{θ_0} at $\varepsilon = 0.2$ and the projection of the associated periodic orbits onto the phase space M . As can be seen in Fig.3.3.3, elliptic and hyperbolic 7-periodic points appear seven each in addition to the 1-periodic point. It follows that stable and unstable 7-periodic orbits appear one each in addition to a stable 1-periodic orbit. The blue points in circles and stars in Fig.3.3.3a correspond to the points of the stable and unstable 7-periodic orbits respectively, while the red circle point corresponds to the point of the stable 1-periodic orbit. It is observed that the resonance condition of the 1 and 7-periodic orbits are $|n/m| = 1$ and $|n/m| = 3/7$ respectively.

However, when the amplitude is increased from $\varepsilon = 0.2$, the resonance condition of the unstable 7-periodic orbit varies to $|n/m| = 5/7$ at around $\varepsilon = 0.213$; the case $\varepsilon = 0.23$ is illustrated in Fig.3.3.4. Furthermore, right before the bifurcation point at around around $\varepsilon = 0.237$, the resonance

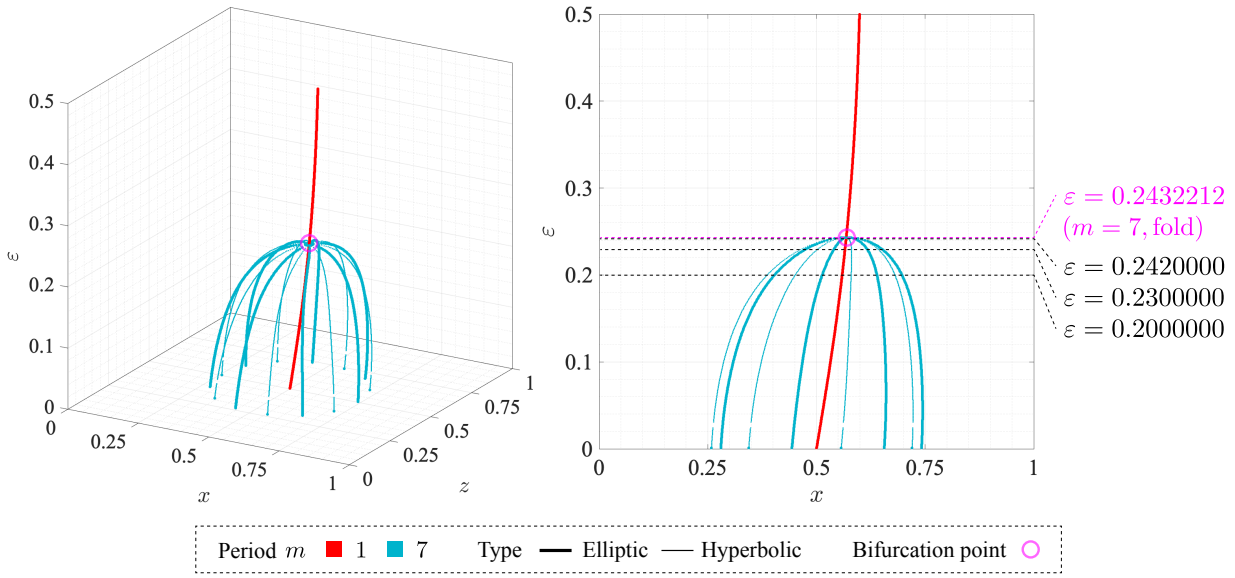
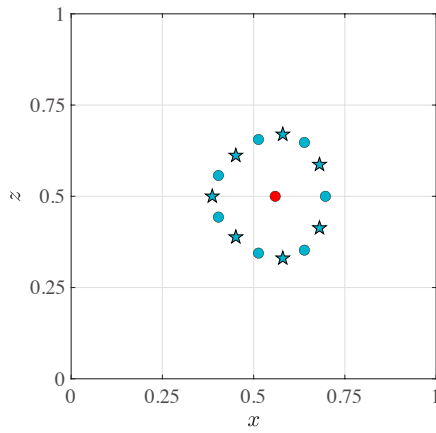
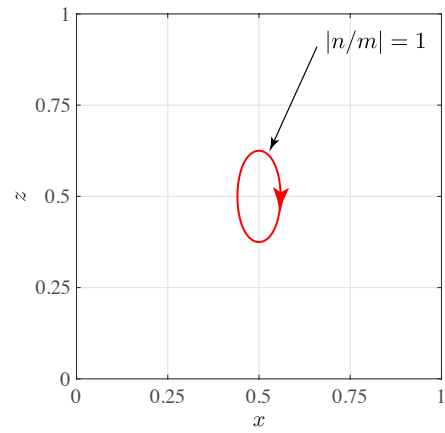


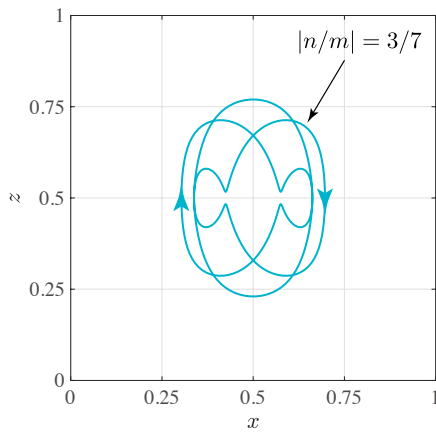
Figure 3.3.2: Bifurcation diagram of 1 and 7-periodic points



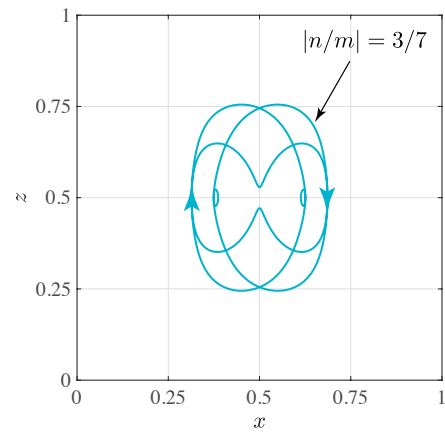
(a) 1 and 7-periodic points



(b) Stable 1-periodic orbit

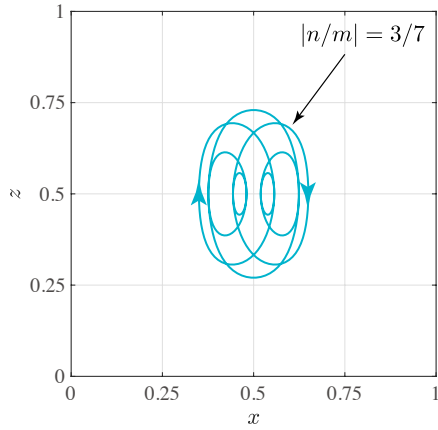


(c) Stable 7-periodic orbit

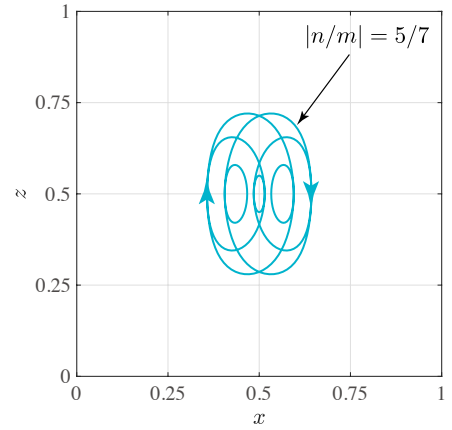


(d) Unstable 7-periodic orbit

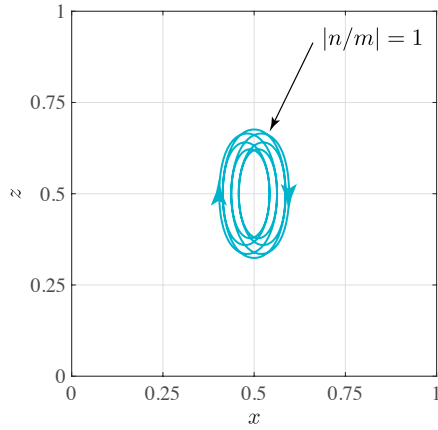
Figure 3.3.3: 1 and 7-periodic points and their orbits at $\varepsilon = 0.2$



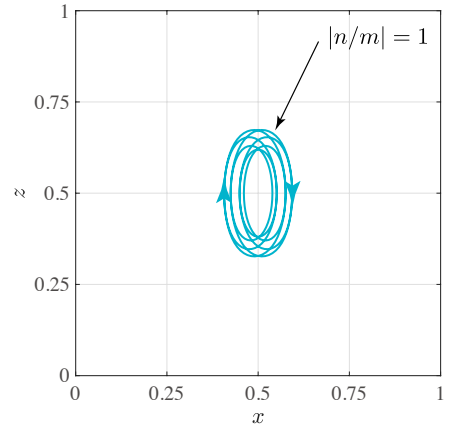
(a) Stable 7-periodic orbit



(b) Unstable 7-periodic orbit

Figure 3.3.4: The projection of 7-periodic orbits at $\varepsilon = 0.23$ 

(a) Stable 7-periodic orbit



(b) Unstable 7-periodic orbit

Figure 3.3.5: The projection of 7-periodic orbits at $\varepsilon = 0.242$

condition of both the stable and unstable 7-periodic orbits varies to $|n/m| = 7/7 = 1$, which corresponds to that of the 1-periodic orbit; the case $\varepsilon = 0.242$ is depicted in Fig. 3.3.5. Therefore, it seems that the 7-periodic orbits disappear at the bifurcation point and vary to a 1-periodic orbit. Further, it is observed in our numerical computation that the projection of the 7-periodic orbits associated with I_1 is symmetric with respect to the horizontal and vertical center lines of the cell regardless of the amplitude ε . It is consistent with Theorem 2.5.1 that the period $m = 7$ and the winding number $n = -3, -5, -7$ are odd. The other m -periodic orbits associated with I_1 vary similarly to the 7-periodic orbits, which indicates that they disappear one by one when ε is increased.

3.4 Bifurcations associated with KAM islands I_2, I_3, I_4

In this section, we analyze the bifurcations associated with the three KAM islands I_2, I_3 , and I_4 around the main island I_1 . Let us first take a look at the bifurcations of 3-periodic points, and then investigate those of 6, 9, 12, and 15-periodic points.

Fold and flip bifurcations of 3-periodic points. Fig.3.4.1 depicts the ε -parameter bifurcation diagram of 3 and 6-periodic points associated with islands I_2, I_3 , and I_4 . Let us first focus on the bifurcation of 3-periodic points which is illustrated in yellow. As can be seen, the branches of 3-periodic points bifurcate similarly to a fork at around $\varepsilon = 0.321$. It is found in our computation that a fold bifurcation occurs at $\varepsilon = 0.3217135$. Let us take a look at how the 3-periodic points and the projection of the associated periodic orbits vary by the bifurcation. Fig.3.4.2 and Fig.3.4.3 show those at $\varepsilon = 0.3$ and $\varepsilon = 0.34$. We can see that three elliptic 3-periodic points appear at $\varepsilon = 0.3$. It follows that one stable 3-periodic orbit appears at $\varepsilon = 0.3$. However, as we increase ε , each elliptic 3-periodic point varies to a hyperbolic one at the bifurcation point and two more elliptic 3-periodic points appear in the neighborhood. This denotes that the stable 3-periodic orbit varies to an unstable 3-periodic orbit at the bifurcation point and two more stable 3-periodic orbits appear at the same time. We denote the two new stable 3-periodic orbits by c_a and c_b , and label the associated elliptic 3-periodic points in Fig.3.4.3 as a and b

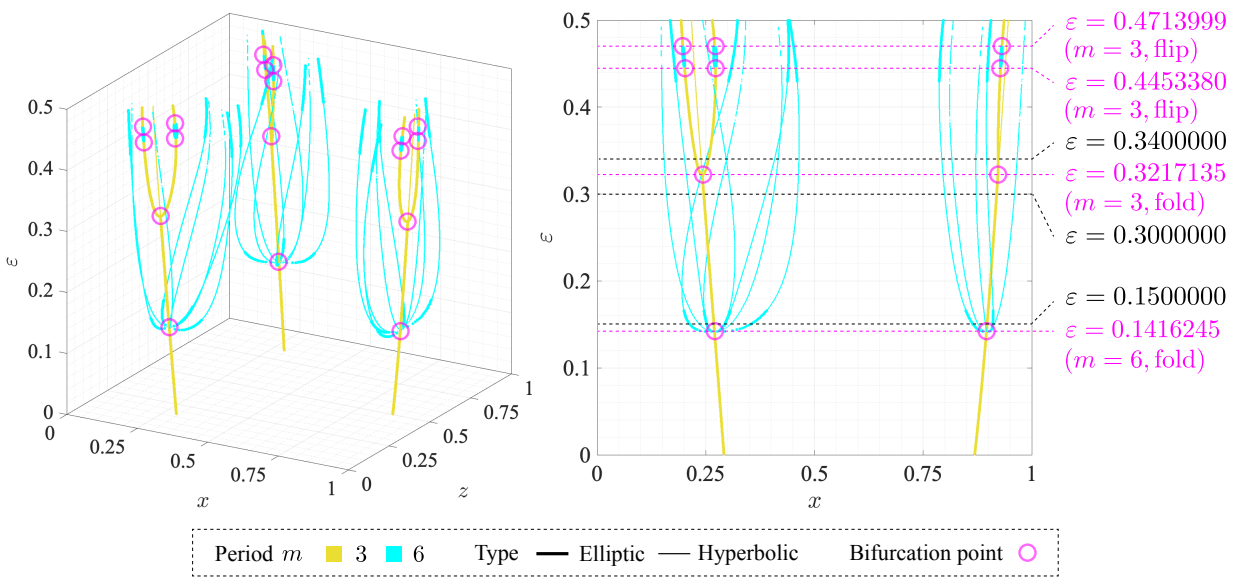
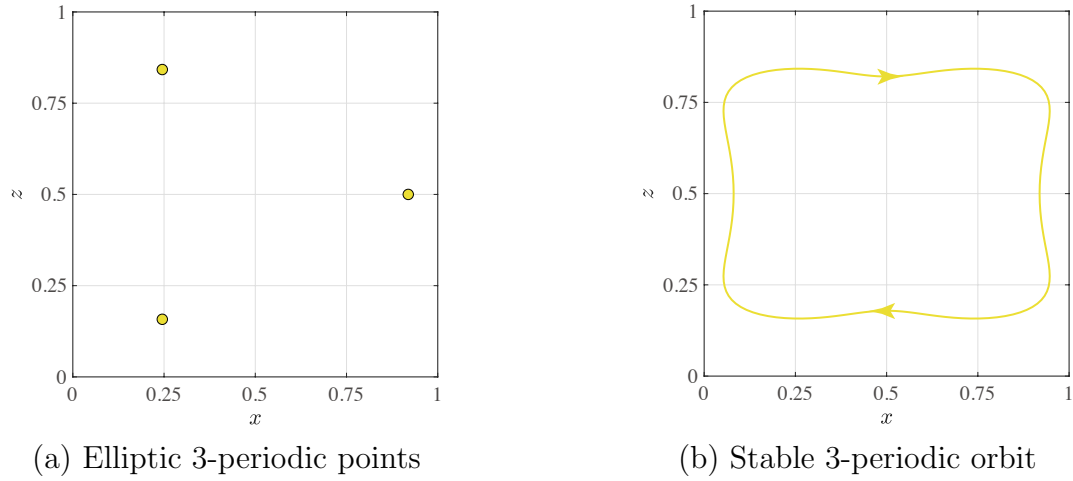
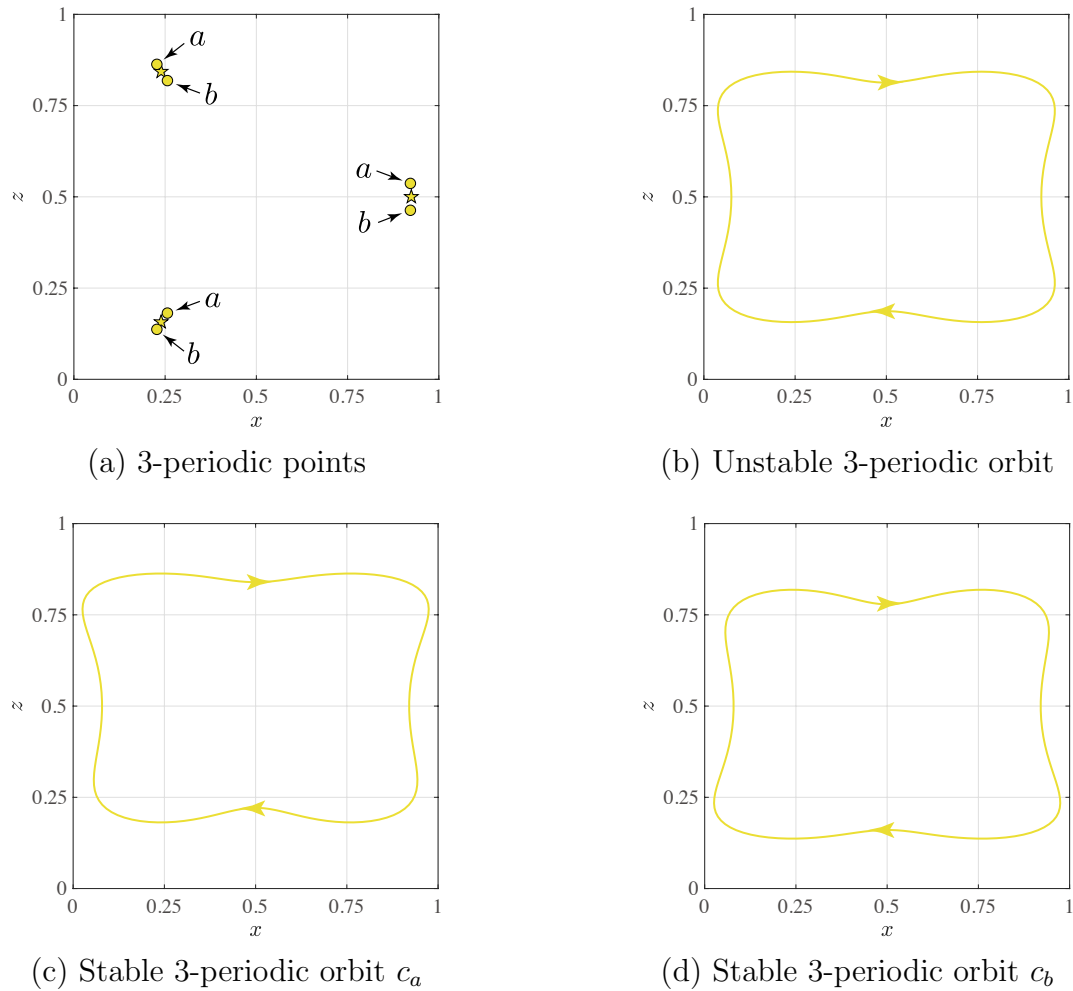


Figure 3.4.1: Bifurcation diagram of 3 and 6-periodic points

Figure 3.4.2: 3-periodic points and their orbits at $\varepsilon = 0.3$ Figure 3.4.3: 3-periodic points and their orbits at $\varepsilon = 0.34$

respectively in order to show the correspondence between the periodic points and their orbits. It is observed that the original stable 3-periodic orbit is symmetric with respect to the horizontal and vertical center lines of the cell,

but those of the two new stable ones are only symmetric with respect to the vertical one. It seems that the stable orbits loose one of the symmetric properties by the bifurcation.

Furthermore, it is clarified in our computation that the 3-periodic points bifurcate in a flip bifurcation at $\varepsilon = 0.4453380$ and $\varepsilon = 0.4713999$. Since the periodic orbits vary around these bifurcation points similarly to those around the flip bifurcations of 4-periodic points in §3.5, we do not discuss this here.

Fold bifurcations of 6-periodic points. As can be seen in Fig.3.4.1, the blue branches of 6-periodic points grow from the yellow branches of 3-periodic points at around $\varepsilon = 0.142$. It is clarified in our computation that the 6-periodic points bifurcate in a fold bifurcation at $\varepsilon = 0.1416245$. Note that the 3-periodic points themselves do not seem to bifurcate when the 6-periodic points bifurcate in a fold bifurcation. Let us take a look at how the periodic orbits vary with ε near such fold bifurcation point. Fig.3.4.4 shows the 3 and

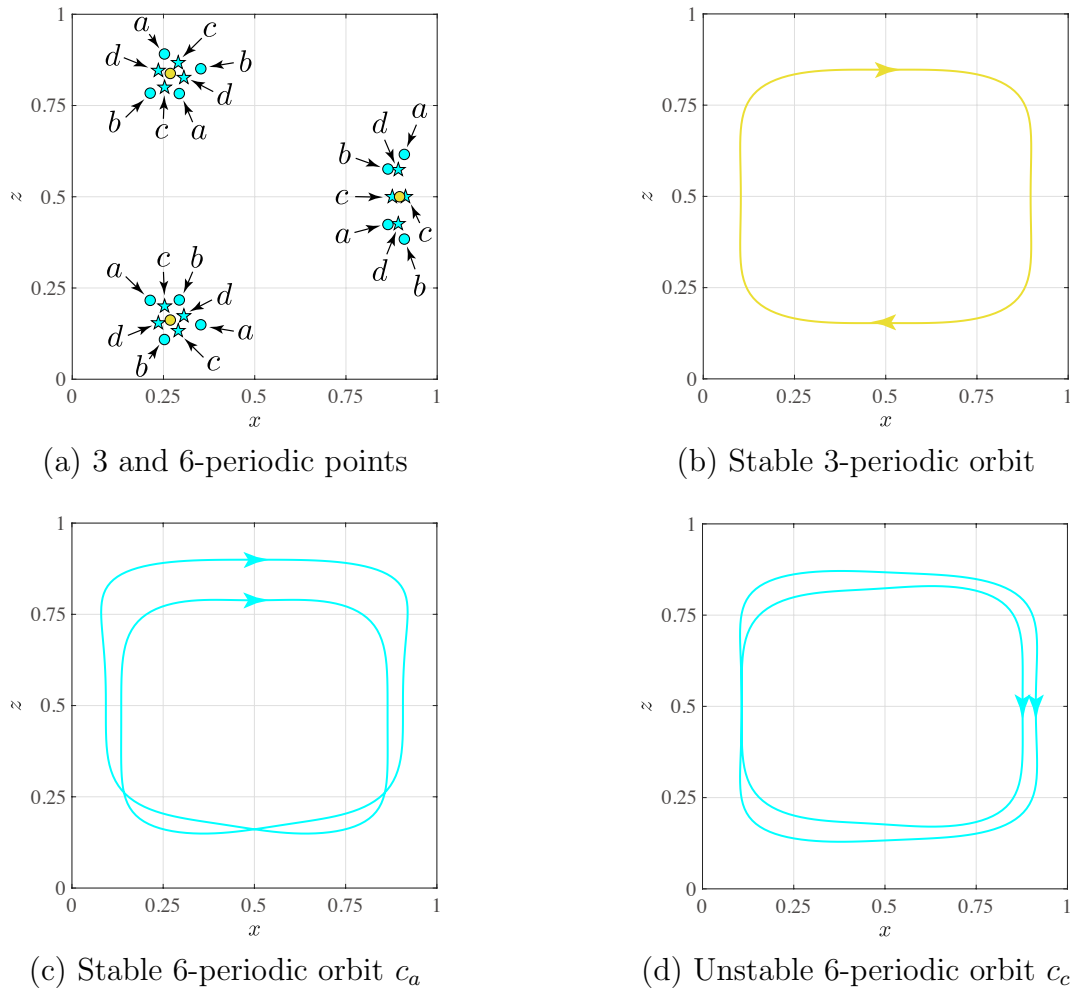


Figure 3.4.4: 3 and 6-periodic points and their orbits at $\varepsilon = 0.15$

6-periodic points and the projection of the associated periodic orbits at $\varepsilon = 0.15$. We can see that elliptic and hyperbolic 6-periodic points appear four each around each elliptic 3-periodic points. It follows that stable and unstable 6-periodic orbits appear two each in addition to the stable 3-periodic orbit. We name the projection of the four 6-periodic orbits as c_a, c_b, c_c , and c_d , and label the associated 6-periodic points in Fig.3.4.4a as a, b, c , and d respectively in order to show the correspondence, where c_a and c_b are symmetric with each other with respect to the horizontal center line of the cell, and c_c and c_d are symmetric with respect to the vertical one. The projection of the 3-periodic orbit and that of the 6-periodic orbits c_a and c_c are illustrated in Fig.3.4.4b – Fig.3.4.4d. It is observed in Fig.3.4.4 that the resonance condition of the 6-periodic orbits are $|n/m| = 1/3$, which is the same of that of the 3-periodic orbit. This implies that the 6-periodic orbits at the bifurcation point correspond to the 3-periodic orbit.

Fold bifurcations of 9, 12, and 15-periodic points. We have seen that the 6-periodic points bifurcate in a fold bifurcation, which makes some branches of 6-periodic points grow from those of 3-periodic points. Such fold bifurcations are also observed in 9, 12, and 15-periodic points associated with islands I_2, I_3 , and I_4 , where the ε -parameter bifurcation diagrams of those periodic points are illustrated in Fig.3.4.5 – Fig.3.4.7. The 9, 12, and 15-periodic orbits vary similarly to the 6-periodic orbits near these bifurcation points. Hence, 3ℓ -periodic orbits ($\ell = 2, 3, 4, 5$) are generated one after another from

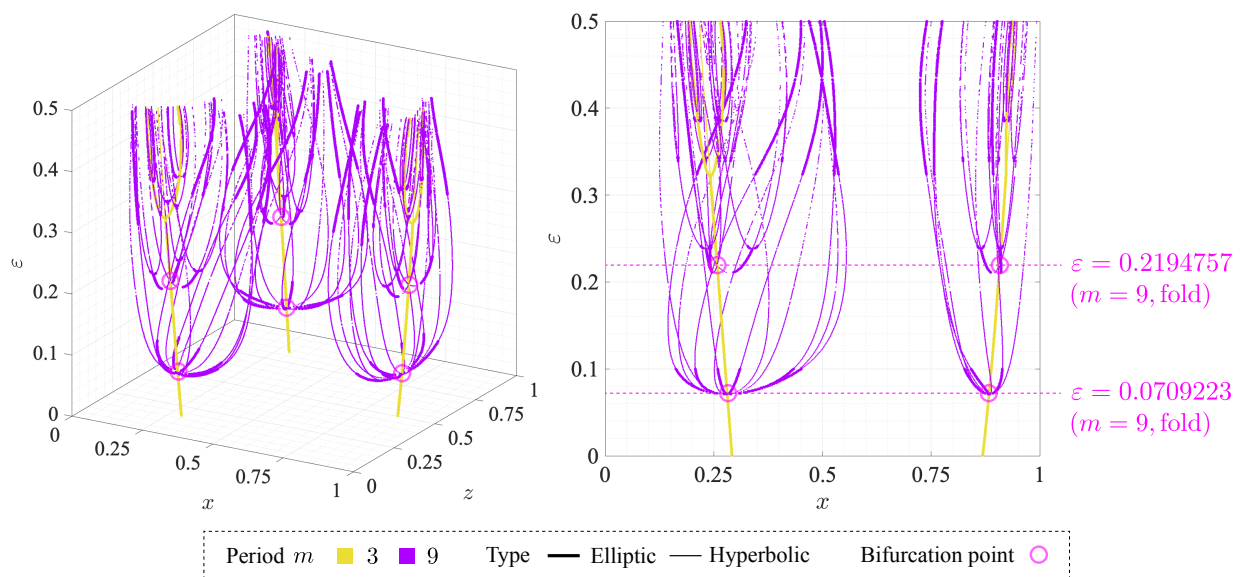


Figure 3.4.5: Bifurcation diagram of 3 and 9-periodic points

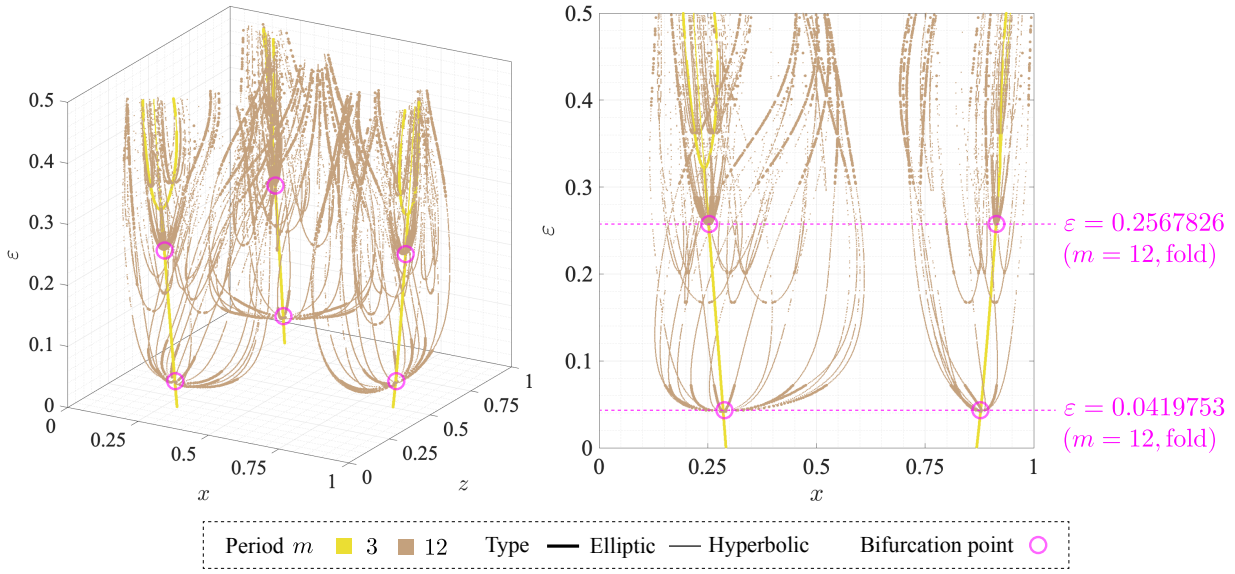


Figure 3.4.6: Bifurcation diagram of 3 and 12-periodic points

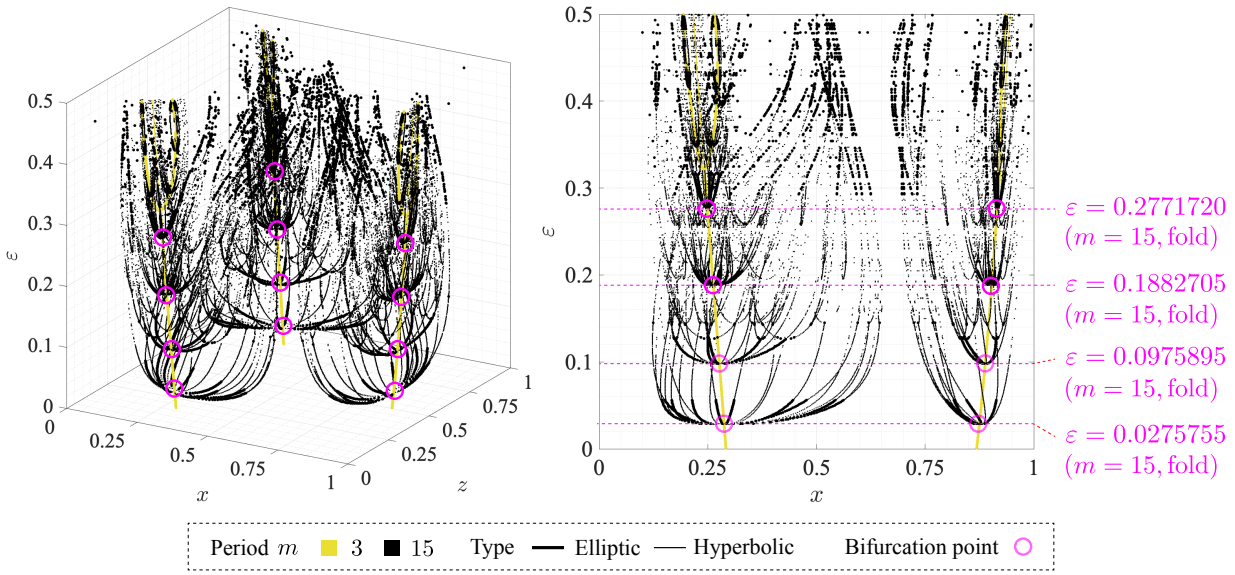


Figure 3.4.7: Bifurcation diagram of 3 and 15-periodic points

the 3-periodic orbits by increasing the amplitude ε of the perturbation. The resonance conditions of the generated orbits are all $|n/m| = 1/3$, since they correspond to the 3-periodic orbit at the bifurcation point.

3.5 Bifurcations associated with other KAM islands

So far we have explored the bifurcations associated with KAM islands I_1, I_2, I_3 , and I_4 . In this section, we investigate those which seem to be associated

with other islands. Here, we especially focus on the bifurcations of 5-periodic points with resonance condition $|n/m| = 1/5$ and those of 4 and 8-periodic points with $|n/m| = 1/4$.

Fold bifurcations of 5-periodic points. Fig.3.5.1 indicates the ε -parameter bifurcation diagram of 5-periodic points of which resonance condition is $|n/m| = 1/5$. It follows that the 5-periodic points bifurcate at $\varepsilon = 0.0469599$ and $\varepsilon = 0.0832330$ in a fold bifurcation. Now let us take a look at how the symmetry of the stable 5-periodic orbits vary by the two bifurcations. Fig.3.5.2a shows the 5-periodic points at $\varepsilon = 0.04$, where it follows that the elliptic and hyperbolic 5-periodic points exist five each on the Poincaré section Σ^{θ_0} . As is illustrated in Fig.3.5.2b, the projection of the orbit of the elliptic 5-periodic points, namely, the stable 5-periodic orbit, is symmetric with respect to the horizontal and vertical center lines of the cell. However, when we increase ε , each elliptic 5-periodic point vary to a hyperbolic 5-periodic point and two new elliptic 5-periodic points appear in the neighborhood by the fold bifurcation at $\varepsilon = 0.0469599$; the case $\varepsilon = 0.053$ is depicted in Fig.3.5.3a. We name the projection of the two new stable 5-periodic orbits as c_a and c_b , and label the associated elliptic 5-periodic points as a and b respectively in order to show the correspondence, where c_a and c_b is symmetric with each other with respect to the horizontal center line. From c_a in Fig.3.5.3b, it follows that the orbit loses one of its symmetric property and becomes only symmetric with the vertical center line.

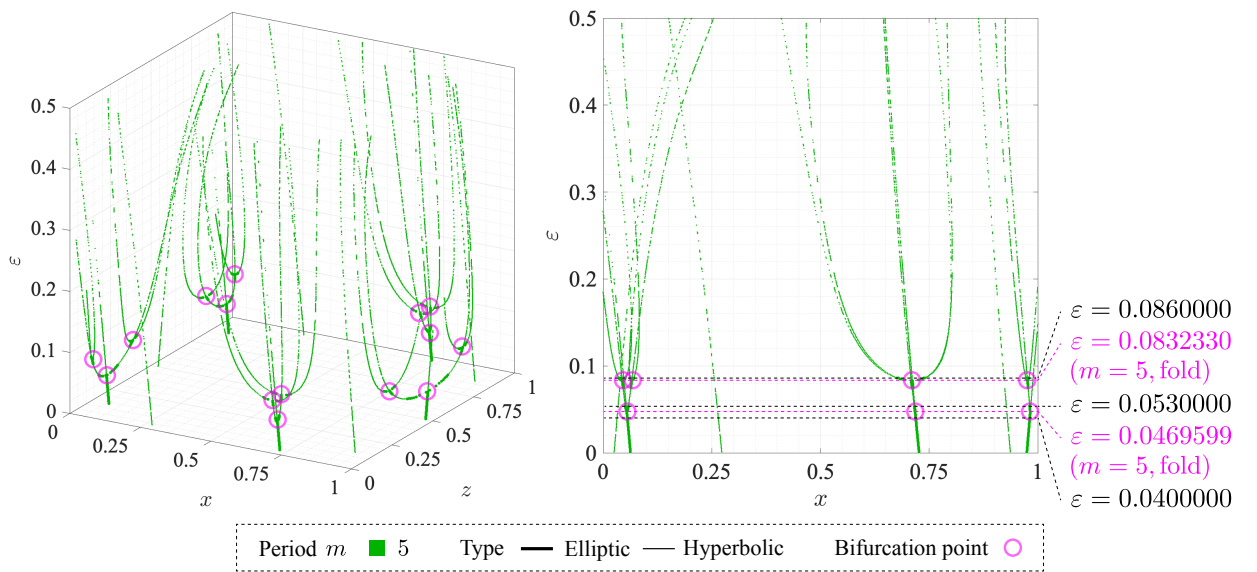
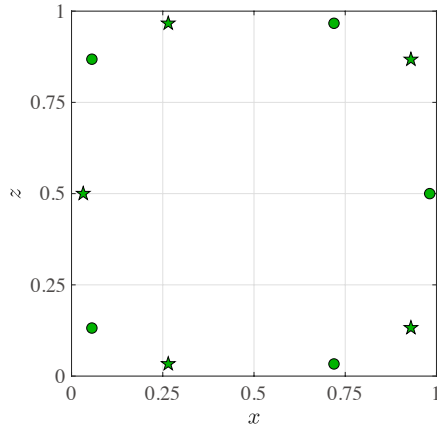
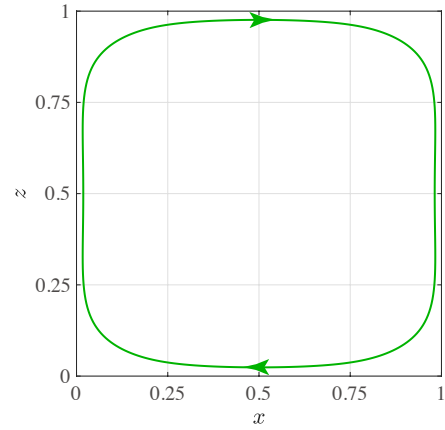


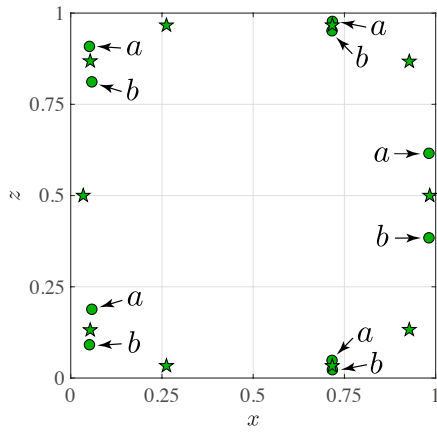
Figure 3.5.1: Bifurcation diagram of 5-periodic points with $|n/m| = 1/5$



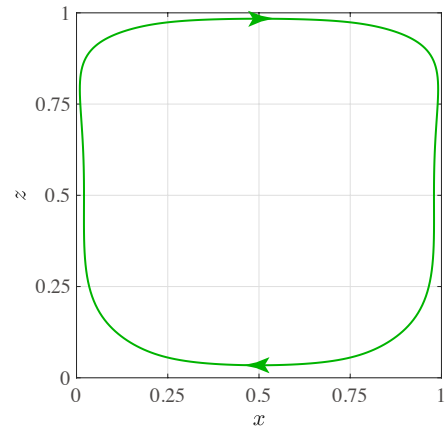
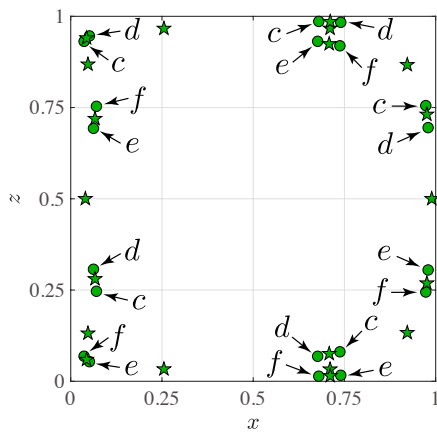
(a) 5-periodic points



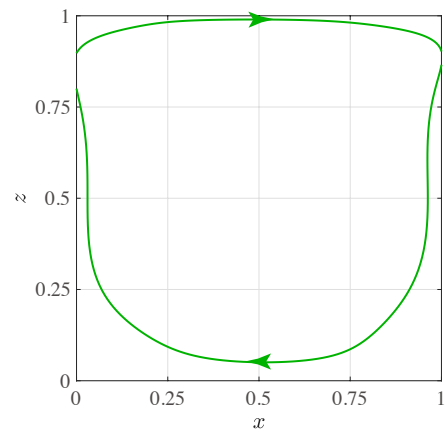
(b) Stable 5-periodic orbit

Figure 3.5.2: 5-periodic points and their orbits at $\varepsilon = 0.04$ 

(a) 5-periodic points

(b) Stable 5-periodic orbit c_a Figure 3.5.3: 5-periodic points and their orbits at $\varepsilon = 0.053$ 

(a) 5-periodic points

(b) Stable 5-periodic orbit c_c Figure 3.5.4: 5-periodic points and their orbits at $\varepsilon = 0.086$

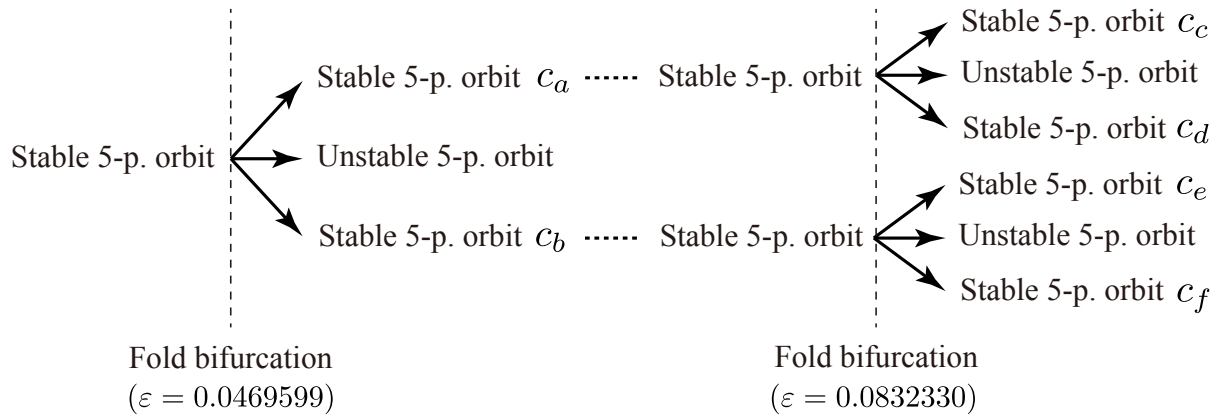


Figure 3.5.5: Conceptual bifurcation diagram of 5-periodic orbits

When the amplitude ε is increased further, the ten elliptic 5-periodic points once vary to hyperbolic ones, but return to elliptic ones. After that, they bifurcate again in a fold bifurcation at $\varepsilon = 0.0832330$, which denotes that twenty elliptic 5-periodic points appear by the bifurcation. Fig. 3.5.4a illustrates the 5-periodic points at $\varepsilon = 0.086$. We denote the projection of the four new stable 5-periodic orbits by c_c, c_d, c_e , and c_f , and label the associated elliptic 5-periodic points as c, d, e , and f respectively in order to show the correspondence, where c_c, c_d, c_e , and c_f are symmetric with each other with respect to the horizontal or vertical center line. The conceptual bifurcation diagram of 5-periodic orbits is depicted in Fig. 3.5.5. From c_c in Fig. 3.5.4b, it follows that the orbit loses its symmetry and becomes asymmetric with respect to the horizontal and vertical center lines of the cell. Hence, the stable 5-periodic orbit of which projection is originally symmetric with respect to the horizontal and vertical center lines of the cell becomes asymmetric by the two fold bifurcations. Furthermore, we can see that the number of 5-periodic orbits increases by the bifurcations and also that they become unstable when ε is large enough, which denotes that the fluid transport becomes more complicated.

Flip bifurcations of 4-periodic points. Next, let us take a look at the bifurcations of 4-periodic points. Fig. 3.5.6 illustrates the ε -parameter bifurcation diagram of 4 and 8-periodic points of which resonance condition is $|n/m| = 1/4$. When the amplitude of the perturbation is $\varepsilon = 0.05$, elliptic and hyperbolic 4-periodic points appear eight each, as is shown in Fig. 3.5.7a. It follows that stable and unstable 4-periodic orbits appear two each. We name the projection of the two stable 4-periodic orbits as c_a and c_b , and label the

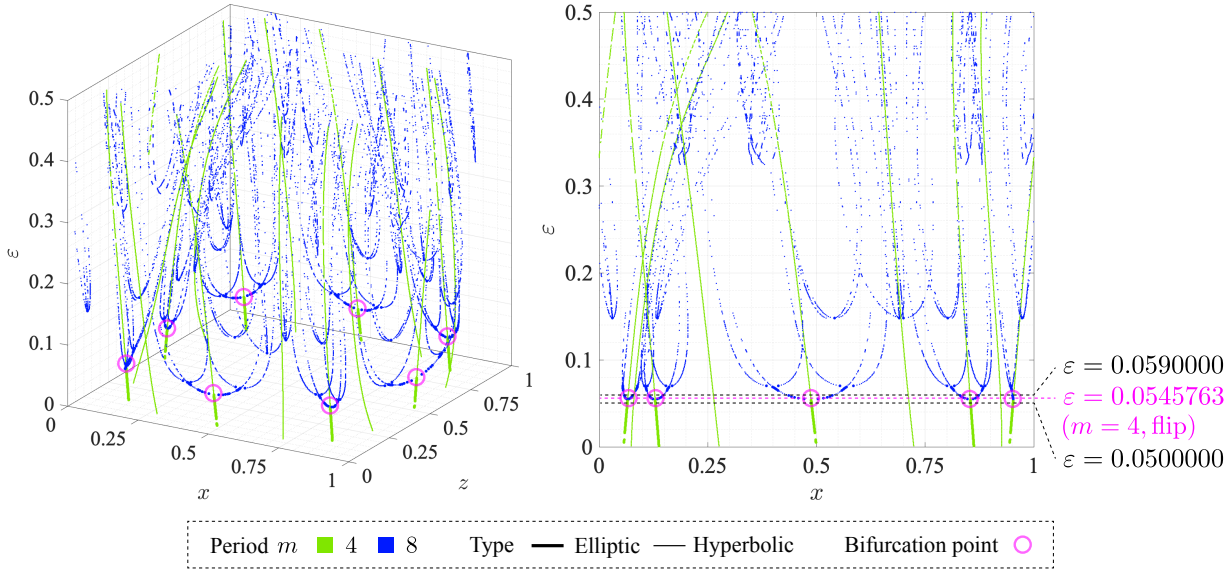
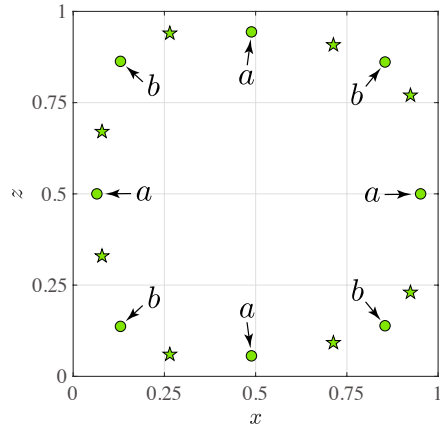


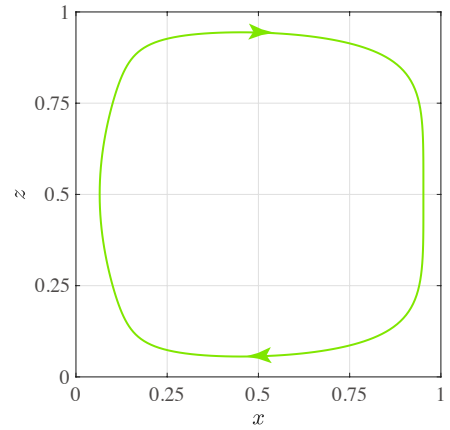
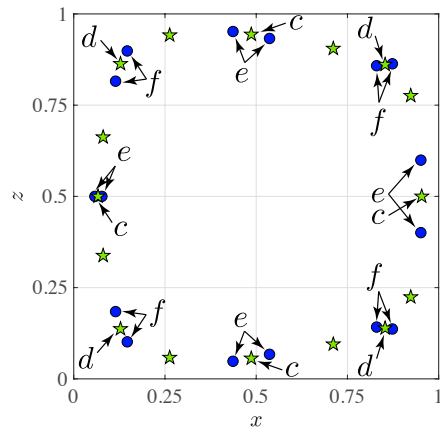
Figure 3.5.6: Bifurcation diagram of 4 and 8-periodic points with $|n/m| = 1/4$

associated elliptic 4-periodic points as a and b respectively in order to show the correspondence. As is shown in Fig.3.5.7b, c_a is only symmetric with respect to the horizontal center line of the cell, which denotes that c_b is symmetric with c_a with respect to the vertical one.

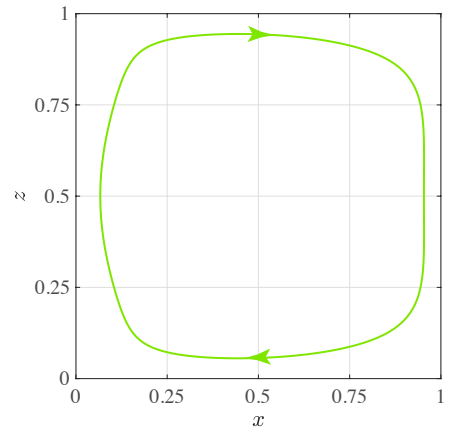
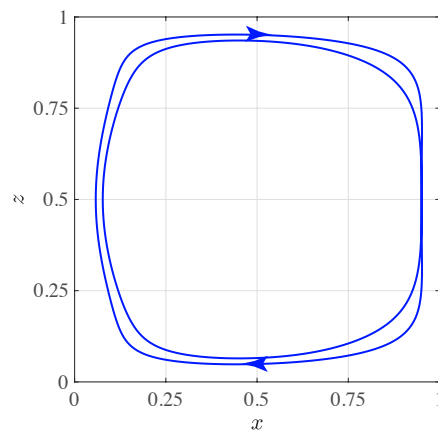
Now, we consider varying the amplitude ε . When the amplitude is increased from $\varepsilon = 0$ to $\varepsilon = 0.5$, the hyperbolic 4-periodic points do not seem to bifurcate. In contrast, it is clarified in our computation that the elliptic 4-periodic points bifurcate in a flip bifurcation at $\varepsilon = 0.0545763$. At the bifurcation point, each elliptic 4-periodic point varies to a hyperbolic one and two new 8-periodic points appear in the neighborhood of each 4-periodic point, where Fig.3.5.8a depicts them at $\varepsilon = 0.059$. It follows that each stable 4-periodic orbit varies to one unstable 4-periodic orbit and one stable 8-periodic orbit by the flip bifurcation. Since there are two stable 4-periodic orbits before the bifurcation, two new unstable 4-periodic orbits and two new stable 8-periodic orbits are generated by the bifurcation. We denote the projection of the former two orbits by c_c and c_d and that of the latter two by c_e and c_f . Then, we label the associated periodic points as c, d, e , and f respectively in order to show the correspondence. Fig.3.5.9 illustrates the conceptual bifurcation diagram of 4-periodic orbits. Note that c_c and c_d as well as c_e and c_f are symmetric with each other with respect to the vertical center line. From c_c and c_e in Fig.3.5.8b and Fig.3.5.8c, it follows that the symmetric axes of all the orbits from c_a to c_f are the same, which is the horizontal center line. In addition, the resonance conditions of the 4 and 8-periodic orbits are both $|n/m| = 1/4$. It follows that the symmetric axis



(a) 4-periodic points

(b) Stable 4-periodic orbit c_a Figure 3.5.7: 4-periodic points and their orbits at $\varepsilon = 0.05$ 

(a) 4 and 8-periodic points

(b) Unstable 4-periodic orbit c_c (c) Stable 8-periodic orbit c_e Figure 3.5.8: 4 and 8-periodic points and their orbits at $\varepsilon = 0.059$

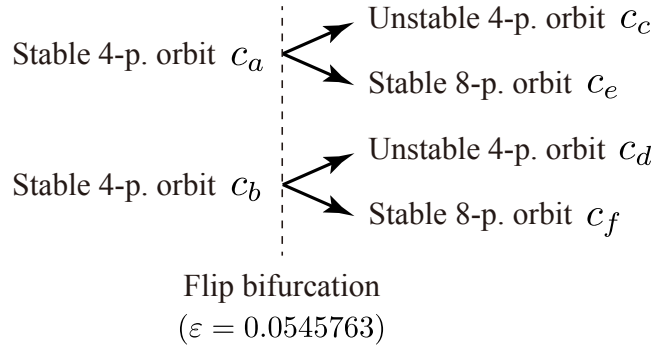


Figure 3.5.9: Conceptual bifurcation diagram of 4-periodic orbits

of the projection and the resonance condition of the periodic orbits do not vary by the bifurcation. Furthermore, it is observed that most of the 4 and 8-periodic orbits become unstable when ε is large enough, which denotes that the fluid transport becomes more complicated.

Discussions of the results in this thesis with other literatures. Finally, let us discuss the results obtained in this thesis in comparison with those in other relevant literatures, though there are not many studies that have analyzed the periodic orbits and their bifurcations in two-dimensional Rayleigh-Bénard convection in the Lagrangian description. As we mentioned in the introduction, Inoue and Hirata [36] analyzed how the chaotic structures in perturbed Rayleigh-Bénard convection vary when the amplitude or frequency of the perturbations is increased. In that study, they clarified that the qualitative patterns of chaotic mixing do not vary so much by increasing the amplitude, while they drastically change by raising the frequency since the frequency is strongly related to the resonance conditions of periodic orbits. In our study it is observed that KAM islands I_1, I_2, I_3 , and I_4 remain for a while when the amplitude is increased, as is shown in Fig. 3.1.2. However, we clarified that many periodic orbits bifurcate one after another and thus the chaotic structures of the flow gradually changes with the amplitude. In particular, islands I_1, I_2, I_3 , and I_4 almost disappear when the amplitude is raised to around $\varepsilon = 0.4$. Such different results are obtained probably because Inoue and Hirata [36] varies the amplitude only up to $\varepsilon = 0.06$ and also that the perturbations of the model in that study is different from those in this thesis. In addition, Oteski, Duguet, and Pastur [52] numerically detected periodic points in two-dimensional oscillatory convection in differentially heated cavity and showed that the whole domain except a small area in the middle becomes chaotic regions when Rayleigh number is raised up to $Ra = 2.05 \times 10^8$. It

is consistent with our result that almost all of the domain becomes chaotic regions when Ra , namely the amplitude of perturbation, is increased enough.

Chabreyrie, Chandre, and Aubry [9] proposed a strategy to create sufficient chaotic mixing in two-dimensional oscillatory electro-osmotic convection in parameter space, where the parameters are the amplitude and frequency of the oscillation. They concluded that sufficient chaotic mixing occurs when some key periodic points at the center of non-mixing regions become hyperbolic. However, in our study, island I_1 remains when the elliptic 3-periodic points at the center of islands I_2, I_3 , and I_4 bifurcate in fold bifurcation at $\varepsilon = 0.3217135$. In addition, as can be seen in Fig.3.1.3, the 1-periodic point at the center of island I_1 still seems to be elliptic when almost all of the domain is filled with chaotic regions at around $0.4 < \varepsilon < 0.5$. Thus, the strategy proposed by Chabreyrie, Chandre, and Aubry [9] may be unsuitable for the model of perturbed Rayleigh-Bénard convection in this thesis.

Further, the dependence of diffusion constant on the amplitude of the perturbations in perturbed Rayleigh-Bénard convection was studied in Ouchi and Mori [54]. When they analyze KAM islands, they observed the period-doubling tree of elliptic 2, 4, 8-periodic points associated with accelerator-mode islands. In this thesis too, we observe some flip bifurcations, namely period-doubling bifurcations, of elliptic 4-periodic points at $\varepsilon = 0.0545763$, as is shown in Fig.3.5.6. Since the parameter settings in that work are different from those in this thesis, we cannot simply compare their results with ours. However, the flip bifurcations observed in the two works may correspond with each other or have some relationship.

3.6 Summary

In this chapter, we investigate the bifurcations of periodic orbits in the perturbed Hamiltonian model of Rayleigh-Bénard convection when the amplitude ε of perturbation is raised and show how the periodic transport varies to chaotic transport. It is indicated that m -periodic points associated with the main KAM island I_1 disappear one after another by fold bifurcations and vary to an elliptic 1-periodic point. In addition, 3ℓ -periodic points ($\ell = 2, 3, 4, 5$) are generated one after another by fold bifurcations around the elliptic 3-periodic points at the center of KAM islands I_2, I_3 , and I_4 , where the 3-periodic points themselves also bifurcate in fold and flip bifurcations. Further, periodic points associated with other islands bifurcate one after another by fold and flip bifurcations and most of them vary to unstable

ones. Hence, the bifurcations of periodic points that may not be associated with I_1 may be the main factor that makes the fluid transport complicated when ε is increased.

Chapter 4

Experimental analysis on invariant structures

In Chap.2 and Chap.3 we have investigated the structures of periodic orbits in a perturbed Hamiltonian model originally proposed by Solomon and Gollub [63] and introduced by Camassa and Wiggins [8]. Although such analysis on a low-dimensional system is important to understand the global structures of fluid transport, invariant structures in perturbed Rayleigh-Bénard convection have not been studied enough by experiments. Therefore, in this chapter, we experimentally investigate the invariant manifolds called Lagrangian coherent structures (LCSs) in perturbed Rayleigh-Bénard convection as well as periodic points by using two-dimensional velocity fields obtained by PIV analysis.

4.1 Dynamical systems theory

Before we look into LCSs and periodic points in perturbed Rayleigh-Bénard convection let us make a brief review on hyperbolic LCSs and lobe dynamics associated with chaotic fluid transport by following Shadden, Lekien, and Marsden [60] and Rom-Kedar and Wiggins [57] respectively. We first review on Finite-time Lyapunov exponent (FTLE), since hyperbolic LCSs are defined as a ridge of an FTLE field.

Definition 4.1.1. Consider a two-dimensional dynamical system, given by

$$\frac{d\mathbf{x}(t)}{dt} = \mathbf{v}(\mathbf{x}(t), t), \quad (4.1.1)$$

where \mathbf{x} denotes an element in an open set $D \subset \mathbb{R}^2$ and \mathbf{v} the velocity field which is at least C^0 in time and C^2 in space. Let $\phi : \mathbb{R}^2 \times \mathbb{R} \rightarrow \mathbb{R}^2$; $(\mathbf{x}_0, t) \mapsto \phi(\mathbf{x}_0, t)$ be a flow map associated with (4.1.1), which induces

the diffeomorphism $\phi^t : D \rightarrow D$, given by

$$\mathbf{x}_0 \mapsto \phi^t(\mathbf{x}_0) := \phi(\mathbf{x}_0, t),$$

where \mathbf{x}_0 indicates a point in D and $\phi^t(\mathbf{x}_0) := \phi(\mathbf{x}_0, t)$ is another mapped point at time t in D . In the case that we specify the initial time t_0 and integration time T such that $\mathbf{x}_0 = \mathbf{x}(t_0)$, we may write the flow map as

$$\phi_{t_0}^t(\mathbf{x}_0) := \phi(\mathbf{x}_0, t), \quad (4.1.2)$$

where $t = t_0 + T$. The finite-time Cauchy-Green tensor is given by

$$\Delta(\mathbf{x}, t_0; T) = \frac{d\phi_{t_0}^{t_0+T}(\mathbf{x})}{d\mathbf{x}}^* \frac{d\phi_{t_0}^{t_0+T}(\mathbf{x})}{d\mathbf{x}},$$

where T denotes the integration time and $*$ denotes the transpose of a matrix. Then, a *Finite-time Lyapunov exponent (FTLE)* is defined as

$$\sigma_{t_0}^T(\mathbf{x}) = \frac{1}{T} \ln \sqrt{\lambda_{\max}(\Delta(\mathbf{x}, t_0; T))},$$

where $\lambda_{\max}(\Delta(\mathbf{x}, t_0; T))$ denotes the maximum eigenvalue of $\Delta(\mathbf{x}, t_0; T)$. In the above, note that the finite time T for integration could be positive and negative. Briefly speaking, the FTLE denotes how much the distance of two points initially in the neighborhood varies in finite time.

Definition 4.1.2. A *Lagrangian coherent structure (LCS)* is defined as a *second-derivative ridge* of σ , which is given by an injective curve $c : (a, b) \rightarrow D$. In particular, a *repelling LCS*, which corresponds to the stable manifold of an autonomous system, is defined as the ridge of an FTLE field with *forward-time integration*, while an *attracting LCS*, which corresponds to an unstable manifold of an autonomous system, is defined as the ridge of an FTLE field with *backward-time integration*; see Shadden, Lekien, and Marsden [60] and Lekien, Shadden, and Marsden [42] for more details.

Numerical methods for detecting hyperbolic LCSs. Let us briefly explain the numerical methods for detecting hyperbolic LCSs. In experimental analysis flow maps are obtained by numerically integrating the measured velocity fields with 4th-order Runge-Kutta method, where -1 is multiplied to the velocity fields for backward-time integration. The velocity of each point is approximated by linear interpolation in the numerical integration, since the velocity data is spatially discrete. On the other hand, in the analysis of perturbed Hamiltonian model flow maps are computed by numerically integrating the velocity fields of the model with 7th-order Runge-Kutta method.

Then, points with FTLE such that $\sigma_{t_0}^T(\mathbf{x}) \geq \alpha \sigma_{\max}$ are considered to be the ridges of FTLE fields, where α is some threshold number and σ_{\max} is the maximum value of $\sigma_{t_0}^T(\mathbf{x})$ in the domain.

Lobe dynamics. Next, let us briefly review the so-called *lobe dynamics* associated with chaotic transport by following Rom-Kedar and Wiggins [57]. Consider a two-dimensional dynamical system given by (4.1.1) and let $\mathbf{v}(\mathbf{x}, t)$ be time-periodic with period T . Then, a Poincaré map P is defined as

$$P = \phi_{t_0}^{t_0+T} : \Sigma \longrightarrow \Sigma,$$

where $\phi_{t_0}^t$ is the flow map given by (4.1.2) and Σ denotes the Poincaré section. Now let Poincaré map P be an area- and orientation-preserving diffeomorphism. We denote each hyperbolic fixed point of P on Σ as p_i ($i \in \mathbb{N}$) and also denote the stable and unstable manifolds growing from each point as $W_{p_i}^S$ and $W_{p_i}^U$ respectively. As is shown in Fig. 4.1.1, let $q_k \in W_{p_i}^S \cap W_{p_j}^U$ ($k \in \mathbb{N}, j \in \mathbb{N}, i \neq j$) be a heteroclinic point associated with p_i and p_j . Further, let $S[p_i, q_k]$ and $U[p_j, q_k]$ be the subspace of $W_{p_i}^S$ from p_i to q_k and that of $W_{p_j}^U$ from p_j to q_k respectively. If q_k is the only one intersection point of $S[p_i, q_k]$ and $U[p_j, q_k]$, then q_k is called a *primary intersection point* (PIP). Let us denote the subspace of $W_{p_i}^S$ and $W_{p_j}^U$ from q_k and q_{k+1} as $S[q_k, q_{k+1}]$ and $U[q_k, q_{k+1}]$ respectively. If no other PIPs exist on $S[q_k, q_{k+1}]$ and $U[q_k, q_{k+1}]$ except q_k and q_{k+1} , the region enclosed by $S[q_k, q_{k+1}]$ and $U[q_k, q_{k+1}]$ is called a *lobe* and the points inside the lobe is mapped by the Poincaré map P to another lobe enclosed by $PS[q_k, q_{k+1}]$ and $PU[q_k, q_{k+1}]$. When the stable and unstable manifolds of a system entangle with each other very complicatedly as homoclinic tangles, point inside lobes may be transported chaotically by horseshoe maps; see Camassa and Wiggins [8].

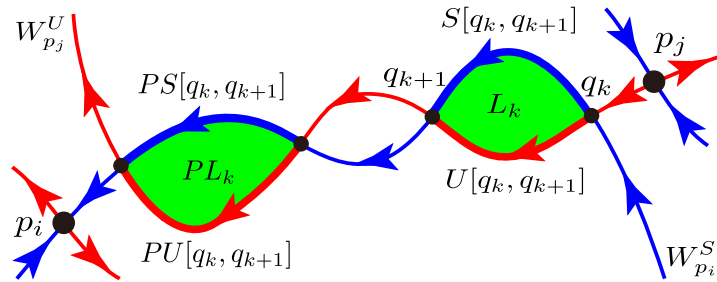


Figure 4.1.1: Lobe dynamics

4.2 Experimental methods

Experimental apparatus. In order to measure the two-dimensional velocity fields of perturbed Rayleigh-Bénard convection by Particle Image Velocimetry (PIV) we develop an experimental apparatus of which schematic illustration is shown in Fig.4.2.1; see B.1 for basic principles of PIV. As can be seen, the apparatus mainly consists of three tanks filled with water, where the temperature of the water in the lower and upper tanks is controlled by two chillers (CL-80R, TAITEC Co.). By setting the temperature of the lower tank higher than that of the upper tank, the water in the test tank is heated from below and cooled from above, since the top plate of the lower tank and the bottom plate of the upper tank is made of cooper to transfer heat. A meshed block is set at the inlet of the channel of the lower and upper tanks so that the temperature of the water around the thermometers becomes uniform. The size of the section of the channel is $100 \text{ mm} \times 20 \text{ mm}$ and the flow rate is around 7 l/min , which indicates that the average flow velocity is around 60 mm/s .

As is depicted in Fig.4.2.2, a transparent acrylic frame is set between the lower and upper tanks. Then, a rectangular box, which we shall call the test box, is created in the test tank and Rayleigh-Bénard convection appears inside the test box. The size of the test box is 200 mm long in x direction, 20 mm deep in y direction, and 10 mm height in z direction. An acrylic plate is located on the left side of the test box in order to prevent useless heat

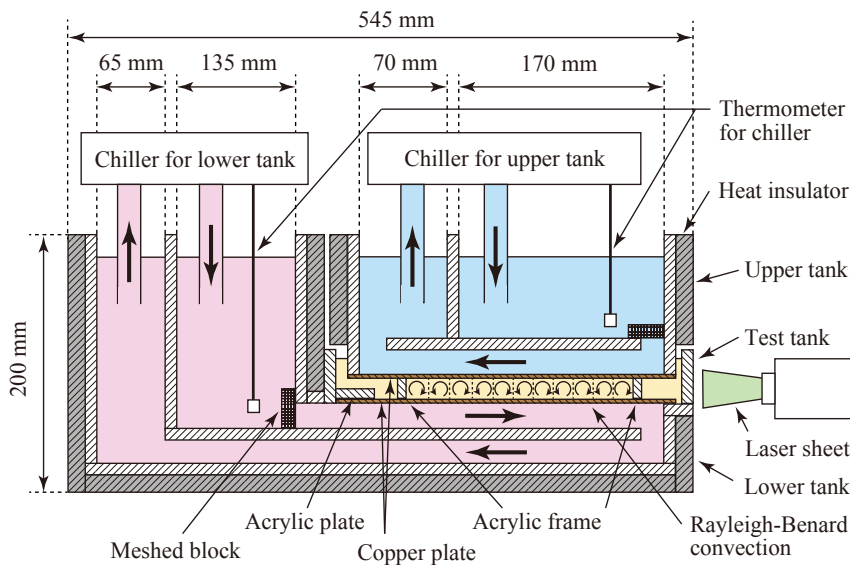


Figure 4.2.1: Experimental apparatus

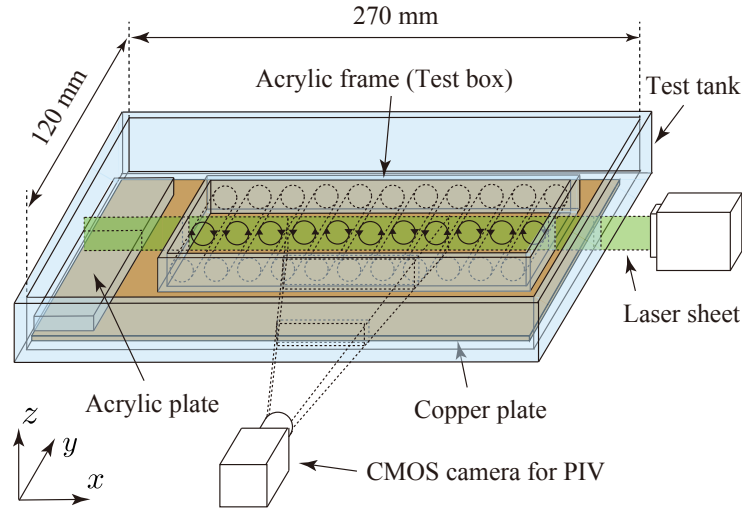


Figure 4.2.2: Test tank

transfer. Note that the scale of the equipments in Fig.4.2.1 and Fig.4.2.2 is deformed to indicate the arrangements clearly. In our study, we set the temperature of the lower and upper tanks to 25 C° and 29 C° respectively so that Rayleigh-Bénard convection with perturbed velocity fields appears in the test box. The Rayleigh number becomes $Ra = 5.6 \times 10^4$ at this condition.

Particle Image Velocimetry (PIV). For the PIV analysis we irradiate a laser sheet (1000m/G, KATO KOKEN Co., Ltd.) perpendicularly to the roll axes of the convection and record the illuminated tracer particles by a monochrome CMOS camera (STC-MBS312TK, OMRON SENTECH Co. Ltd.) from the direction of the roll axes in 10 fps, where nylon particles (KP-010TK, KATO KOKEN Co., Ltd.) with diameter 10 μm is used as tracer particles. The recording area is set in the middle of the test box where the wall of the box may affect the flow minimally. Then, we obtain the two-dimensional velocity fields of the Rayleigh-Bénard convection from the recorded image by using a commercial PIV software (FlowExpert2D2C, KATO KOKEN Co., Ltd.). The resolution of the camera is 2048×512 pixels and the spatial resolution is 0.038 mm/pixel. The interrogation window size for the PIV analysis is set to 32×32 pixels.

4.3 Perturbations observed in velocity fields

Perturbations observed in velocity fields. Fig.4.3.1 and Fig.4.3.2 illustrate the velocity fields and streamlines of Rayleigh-Bénard convection obtained by PIV analysis, where we will explain the notation $T = 17.4$ s in the caption

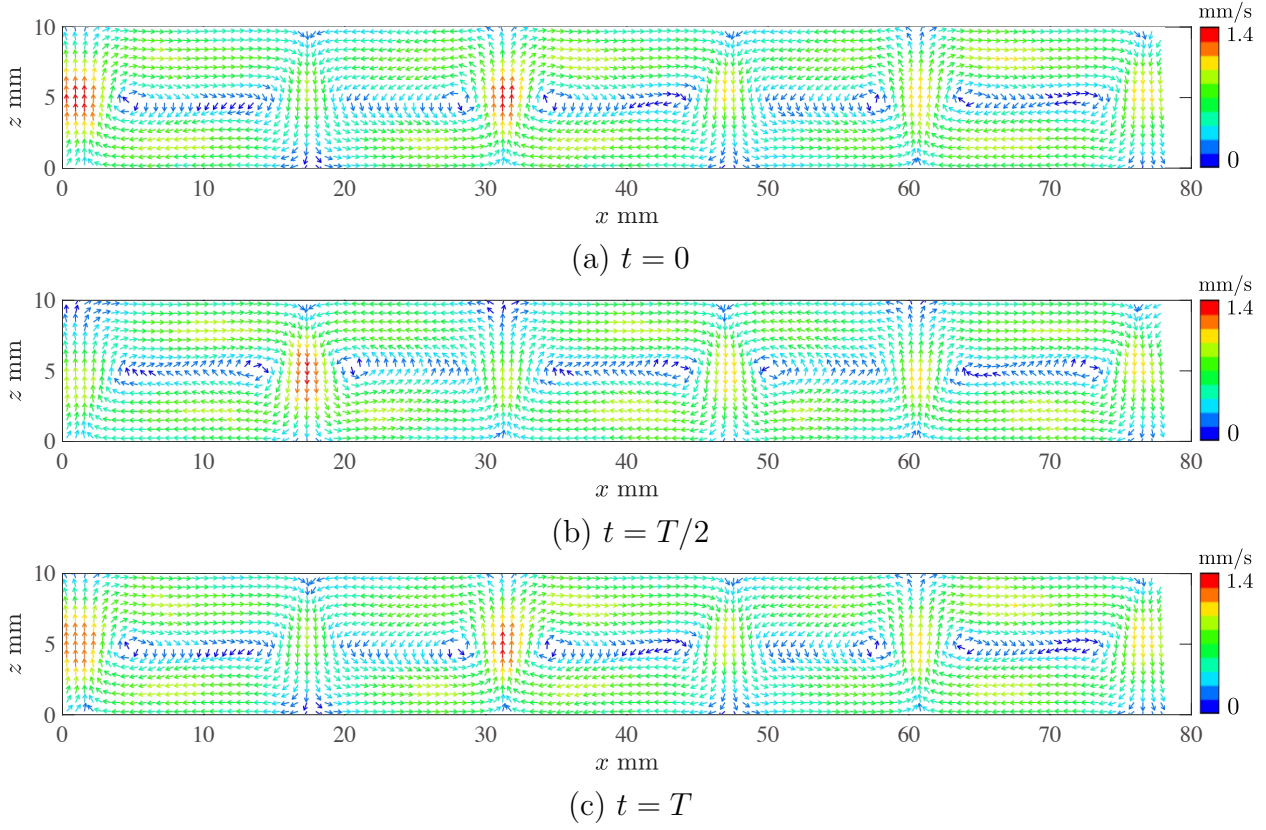


Figure 4.3.1: Velocity fields in experiments

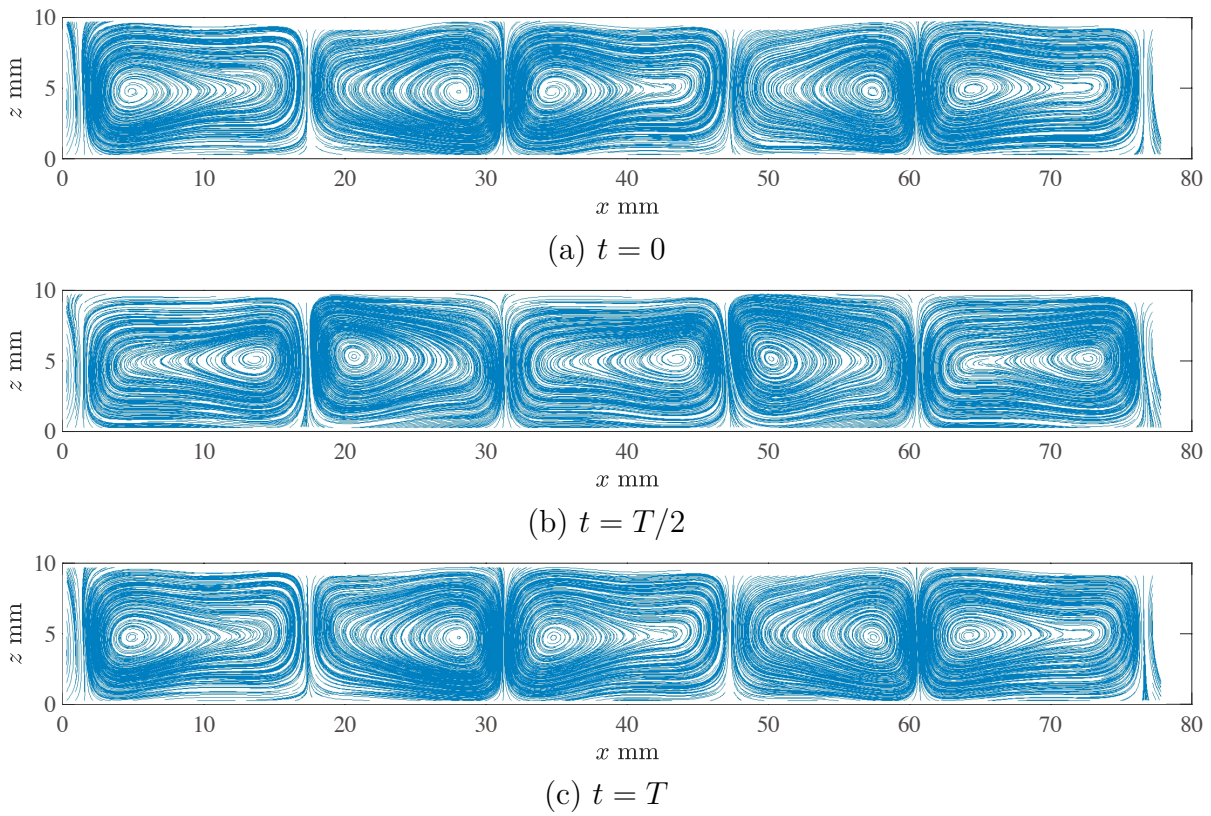


Figure 4.3.2: Streamlines in experiments

later on. We can see that five convection cells appear in the recorded area and that two types of cells with different width appear alternately in the layer. Note that the width of cells may become almost uniform in some experimental cases. Further, it is observed in Fig.4.3.1 and Fig.4.3.2 that the center of vortices in each cell oscillates side by side and that velocity around cell boundaries tend to increase when the center of vortices moves close. It follows that the velocity fields are perturbed. In order to investigate such perturbations more in detail we analyze the spectrum of velocity u and w in x and z direction at each point shown in magenta in Fig.4.3.3. The coordinates of the points are set to $x = 1, 3, \dots, 9$ mm and $z = 1, 3, \dots, 77$ mm. The spectrums are depicted in Fig.4.3.4 – Fig.4.3.8, where the spectrum of points on the same coordinates z are illustrated all together. It is observed that a maximum peak appear at $f = 0.0576$ Hz for all points, where we ignore the peaks at $f = 0$ Hz, which indicate the stationary components of the time variation. It follows that the whole velocity fields are perturbed almost periodically in period $T = 1/f = 17.4$ s. Fig.4.3.9 illustrates the time variation of velocity in x and z direction at point $(x, z) = (47 \text{ mm}, 5 \text{ mm})$ near a cell boundary. We can see that the velocity oscillates almost periodically.

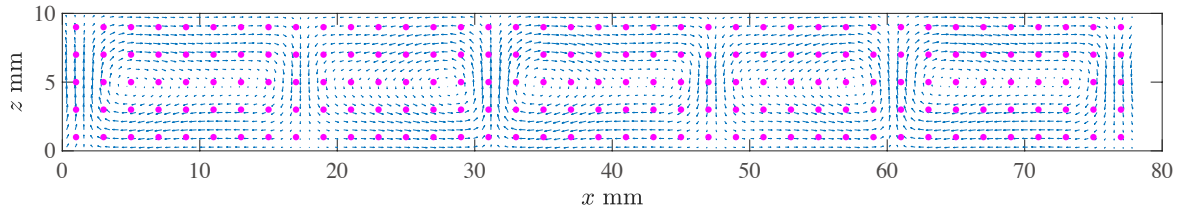


Figure 4.3.3: Points for spectral analysis on velocity fields at $t = 0$

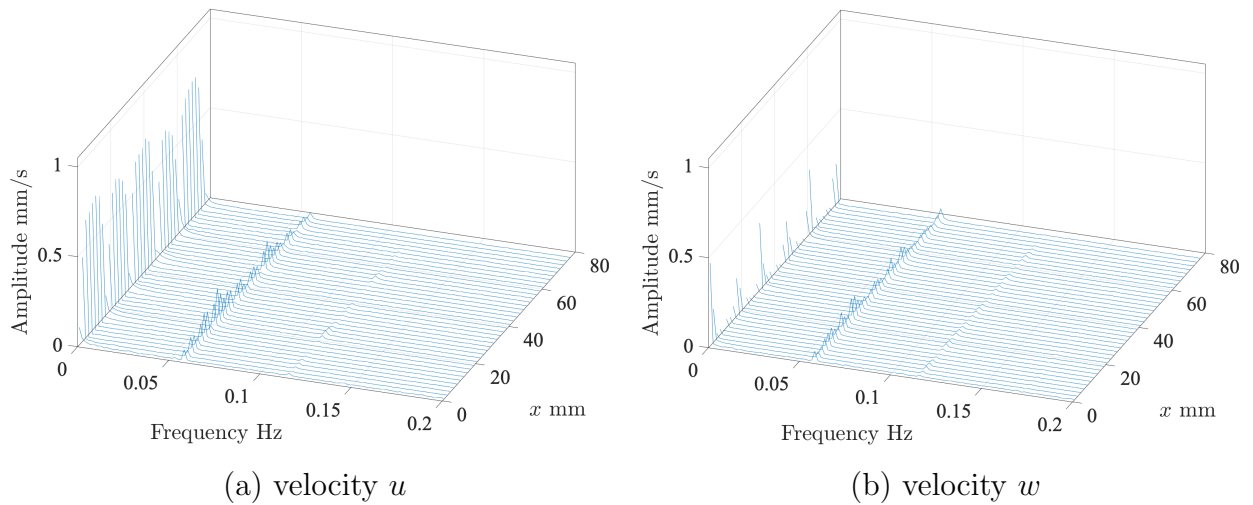
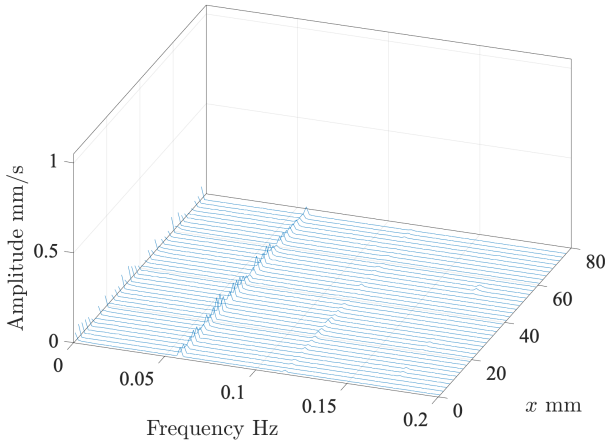
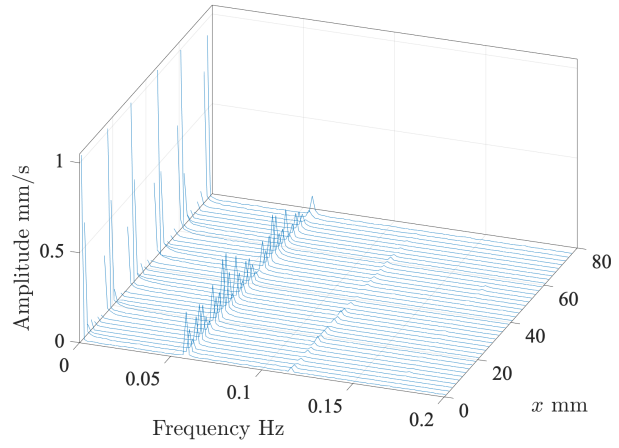
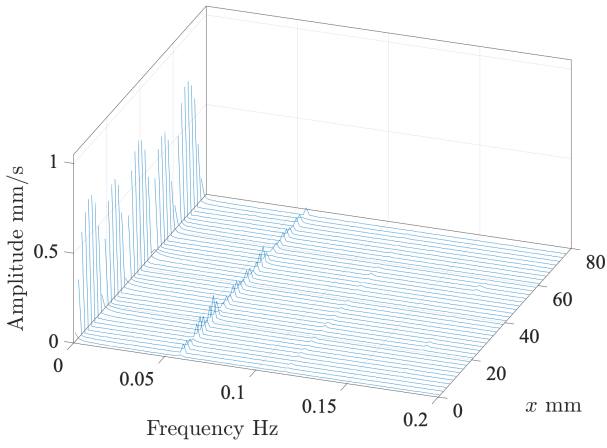
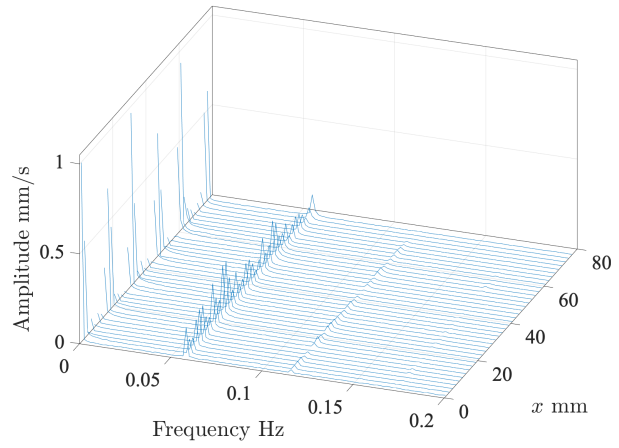
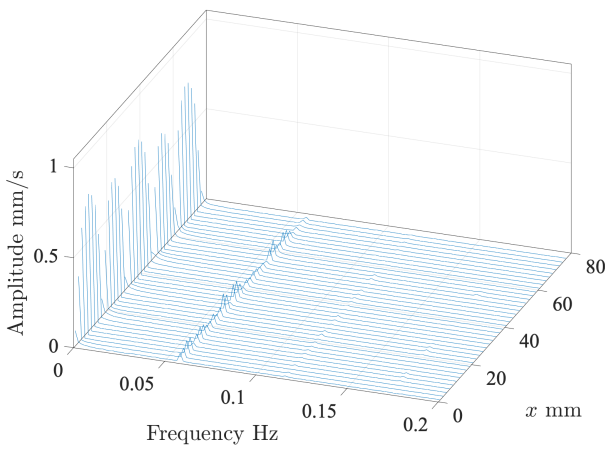
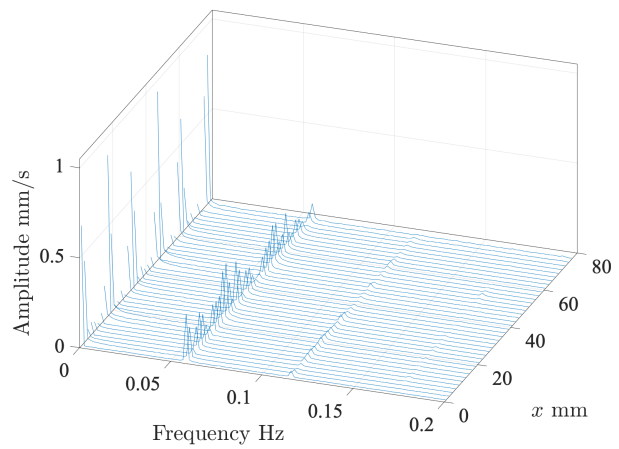
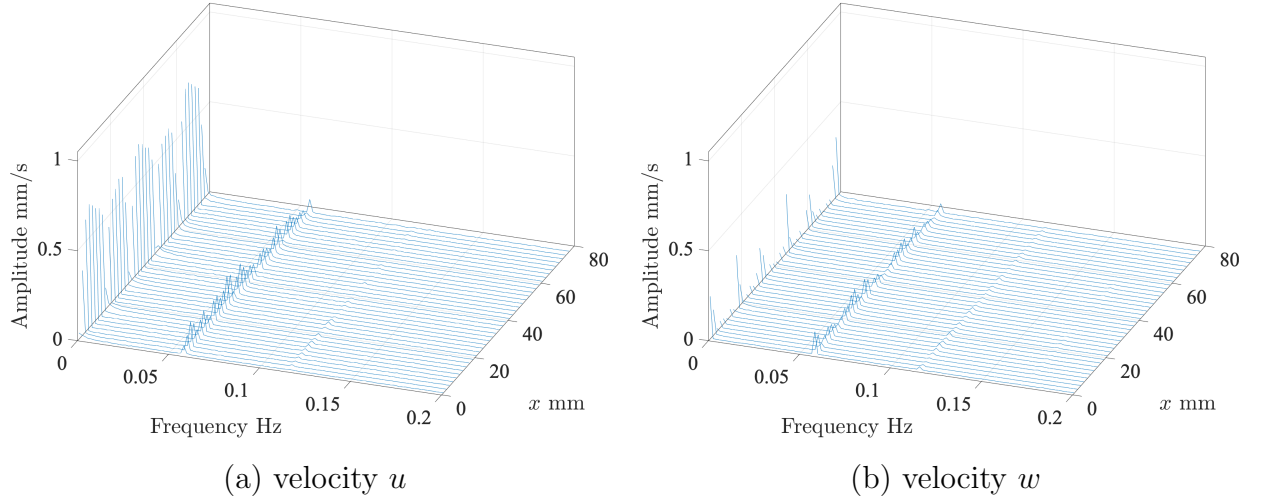
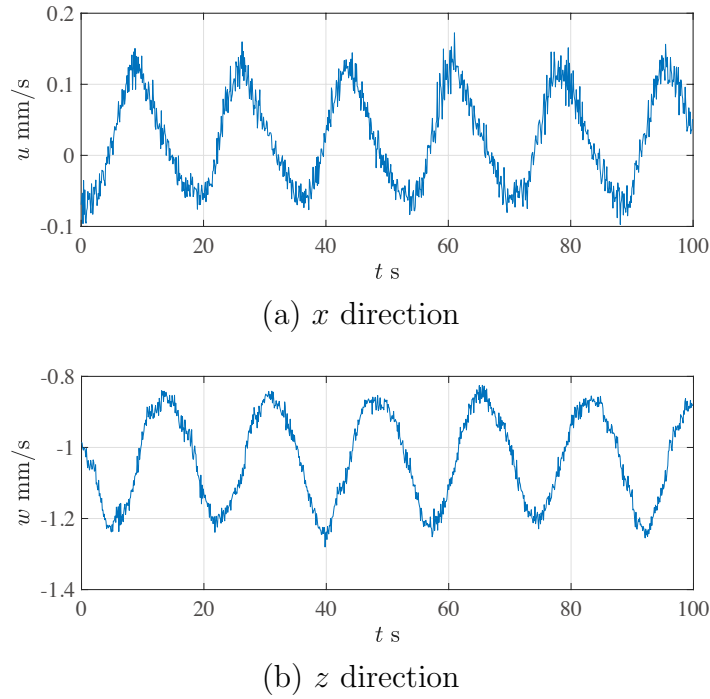


Figure 4.3.4: Spectrum of velocity at points on $z = 1$ mm

(a) velocity u (b) velocity w Figure 4.3.6: Spectrum of velocity at points on $z = 5$ mm(a) velocity u (b) velocity w Figure 4.3.5: Spectrum of velocity at points on $z = 3$ mm(a) velocity u (b) velocity w Figure 4.3.7: Spectrum of velocity at points on $z = 7$ mm

Figure 4.3.8: Spectrum of velocity at points on $z = 9$ mmFigure 4.3.9: Velocity at $(x, z) = (47 \text{ mm}, 5 \text{ mm})$ near a cell boundary

4.4 Hyperbolic LCSs in experiments

FTLE fields and hyperbolic LCSs in experiments. Fig.4.4.1 and Fig.4.4.2 depict the FTLE fields with forward- and backward-time integration. The initial time and integration time is set to $t_0 = 0$ and $T_{\text{int}} = T, 2T, 3T, 5T, 8T, 15T$ respectively, where $T = 17.4$ s is the period of the perturbation. Further, Fig.4.4.3 shows the hyperbolic LCSs detected from the FTLE fields, where

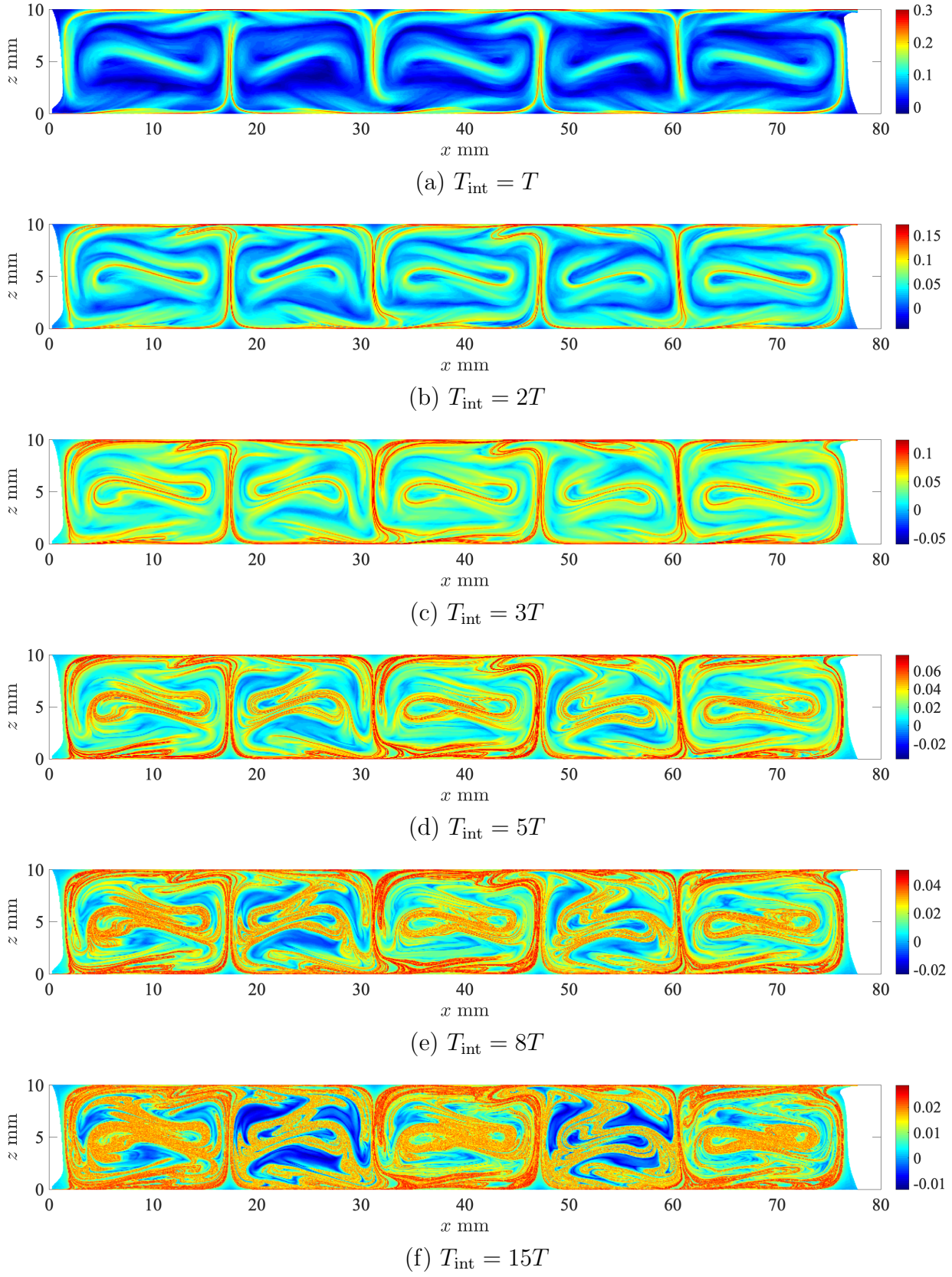


Figure 4.4.1: Forward FTLE fields in experiments

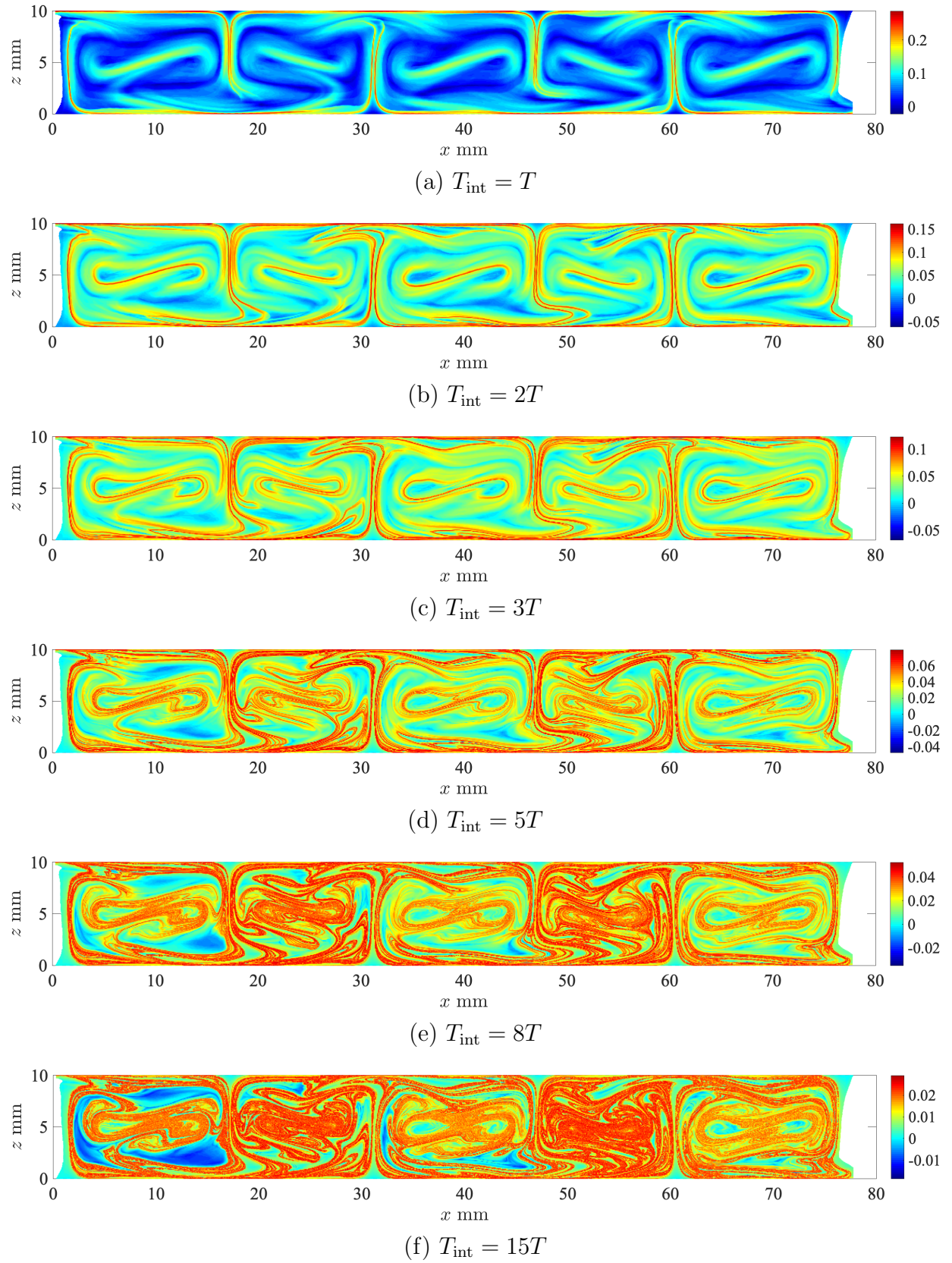


Figure 4.4.2: Backward FTLE fields in experiments

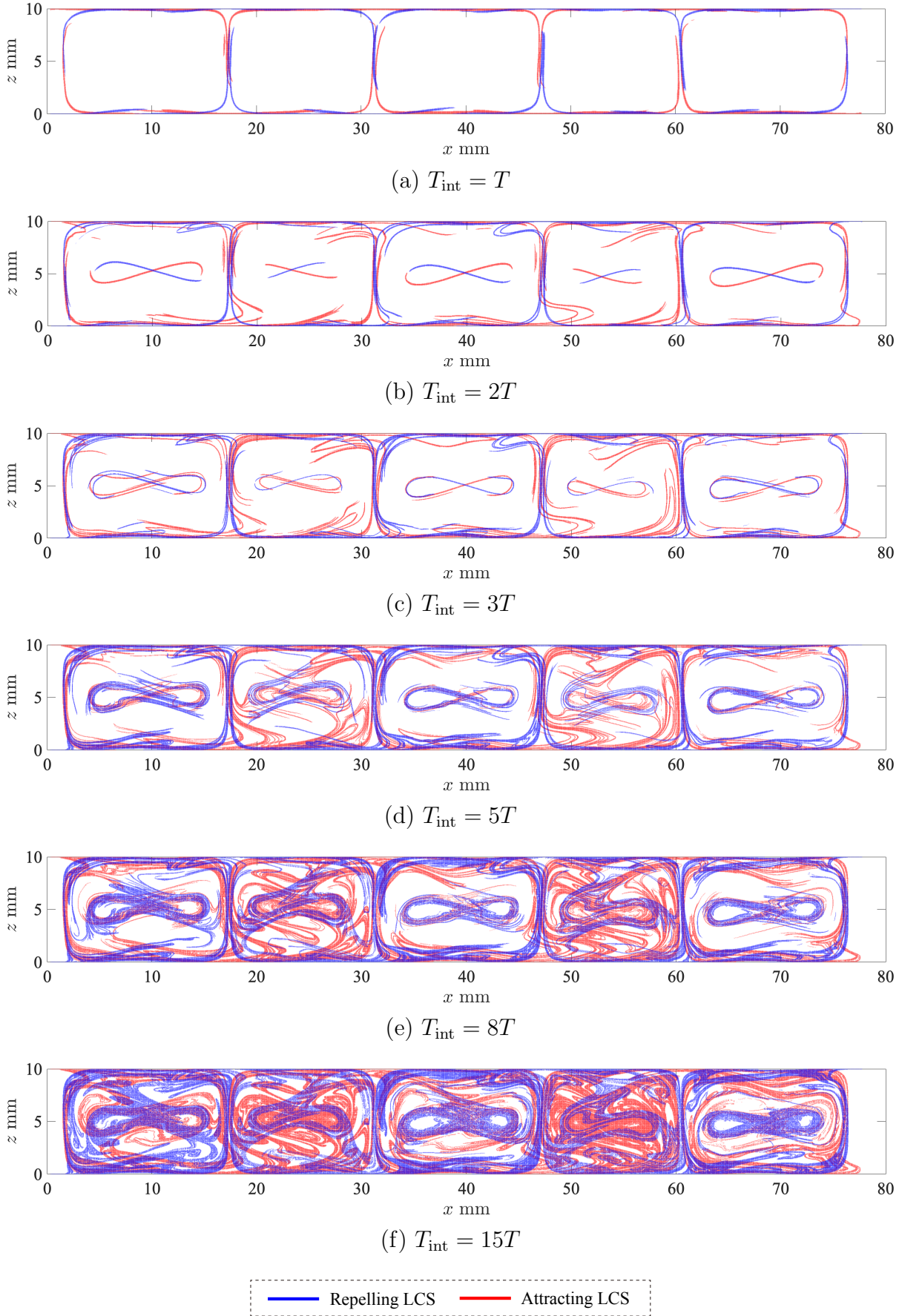


Figure 4.4.3: Hyperbolic LCSs in experiments

the repelling and attracting LCSs are illustrated in blue and red respectively. Let us take a look at the LCSs around $x = 47$ mm in Fig.4.4.3c. The repelling LCS in blue grows from the bottom to the top along the cell boundary and is finally bent from side to side around the upper boundary, while the attracting LCS in red grows from the other side and is similarly bent from side to side around the lower boundary. Hence, the attracting and repelling LCSs around cell boundaries entangle with each other, which indicates that homoclinic tangles are created. It is also observed that they are asymmetric with each other with respect to the horizontal center line $z = 5$ mm. Further, we can see that a figure-eight structure appears in the middle of each cell. Comparing Fig.4.4.3 and Fig.1.1.5, notice that such figure-eight structures do not appear in the simple model originally proposed by Solomon and Gollub [63] and introduced by Camassa and Wiggins [8].

Next, let us take a look at the LCSs with larger integration time. We can see that the LCSs entangle with each other more complicatedly than those with smaller integration time and that two types of cells with different structures appear alternately in the layer. One type are those which figure-eight structures in the middle entangle with the LCSs around cell boundaries, while the other type are those which they do not so much. Such structures do not appear in the simple model proposed by Solomon and Gollub [63] and Camassa and Wiggins [8] too.

Lobe dynamics observed near a cell boundary. As we have seen, the hyperbolic LCSs entangle with each other very complicatedly and create homoclinic tangles. It follows that many lobes appear in the perturbed Rayleigh-Bénard convection. Let us focus on the transport of fluid particles inside lobes. First, we take a look at those inside a lobe near a cell boundary. Fig.4.4.4 shows the transport of fluid particles inside a lobe around $x = 45$ mm in each period of perturbation from $t = 0$ to $t = 4T$. The fluid particles are indicated in green with the repelling and attracting LCSs in blue and red. The fluid transport is computed by numerically integrating the measured velocity fields with 4th-order Runge-Kutta method, where velocity at each point is approximated by linear interpolation. The integration time of the LCSs is $T_{\text{int}} = 5T$. It is observed that fluid particles are transported from one lobe to another in each period of perturbation, which indicates that fluid transport follows the lobe dynamics. It follows that fluid particles inside lobes may be transported chaotically by horseshoe maps, since the LCSs entangle complicatedly when the integration time is large.

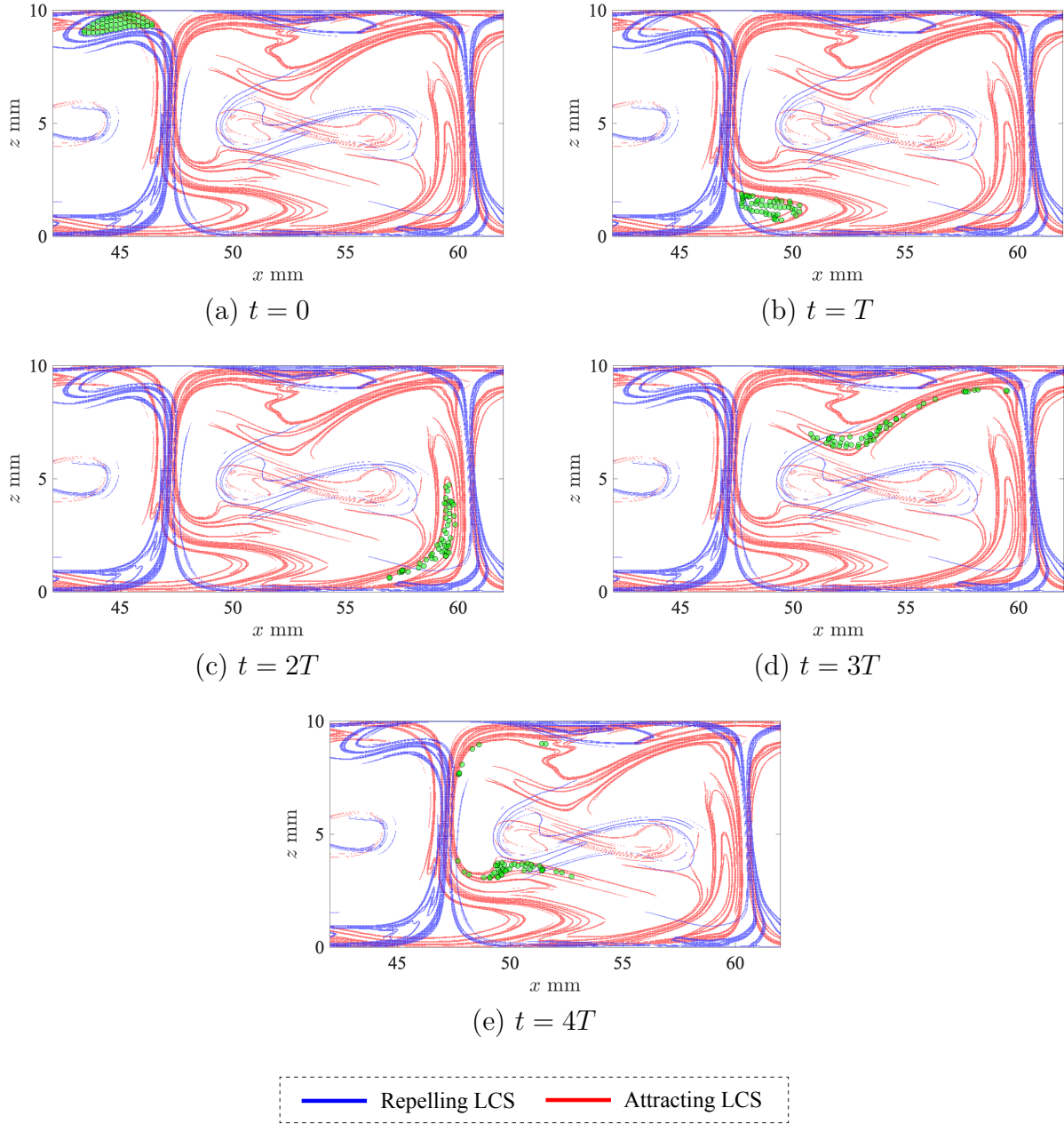


Figure 4.4.4: The transport of fluid inside a lobe near a cell boundary

Lobe dynamics observed near a figure-eight structure. Next, let us take a look at the transport of fluid particles inside a lobe near a figure-eight structure. Fig. 4.4.5 illustrates fluid transport around a figure-eight structure which range from about $x = 34$ mm to $x = 45$ mm. The integration time of the LCSs is $T_{\text{int}} = 5T$. We can see that fluid transport follows the lobe dynamics. Thus, it is implied that fluid particles inside lobes around figure-eight structures may be transported chaotically as well by horseshoe maps.

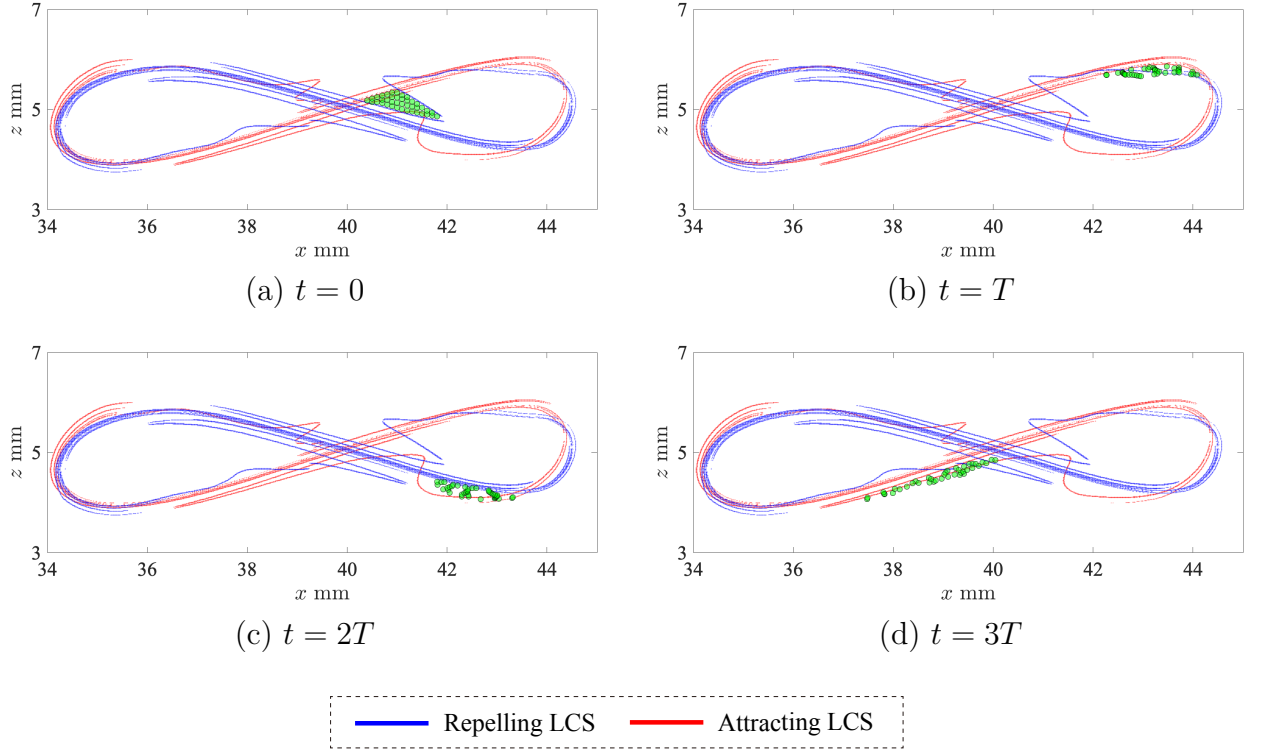


Figure 4.4.5: The transport of fluid inside a lobe near a figure-eight structure

4.5 Periodic points and elliptic LCSs in experiments

Periodic points detected in experiments. Next, we analyze periodic points to investigate periodic fluid transport in experiments. In order to detect the periodic points from the experimental data we cover the domain with a small grid spacing and compute the Poincaré maps of each grid point by numerically integrating the measured velocity fields. Here, the Poincaré map is defined as a flow map from $t = t_0$ to $t = t_0 + T$ similarly as in the model in Chap.2 and Chap.3, where T is the period of the perturbation. Then, recall that periodic points are defined in (2.2.3) by using a Poincaré map $P_\varepsilon^{\theta_0}$ in the perturbed Hamiltonian model. However, since no fluid particles are transported exactly periodically in experiments, we shall consider point $\mathbf{x} \in D \subset \mathbb{R}^2$ to be an m -periodic point, if

$$|P^m(\mathbf{x}) - \mathbf{x}| < \delta, \quad (4.5.1)$$

while

$$|P^\ell(\mathbf{x}) - \mathbf{x}| > \delta \text{ for } \forall \ell \in \{\text{divisor of } m\} \text{ } (m \geq 2), \quad (4.5.2)$$

where D is the domain of the flow and P denotes the Poincaré map. From the physical point of view, (4.5.1) indicates that a fluid particle is transported

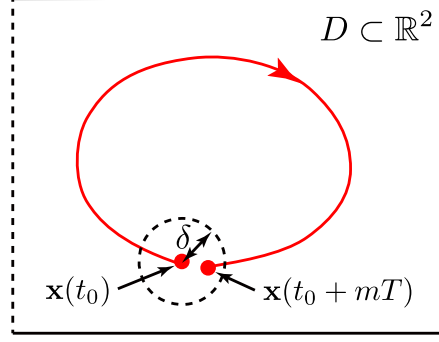


Figure 4.5.1: Conditions for periodic points in experiments

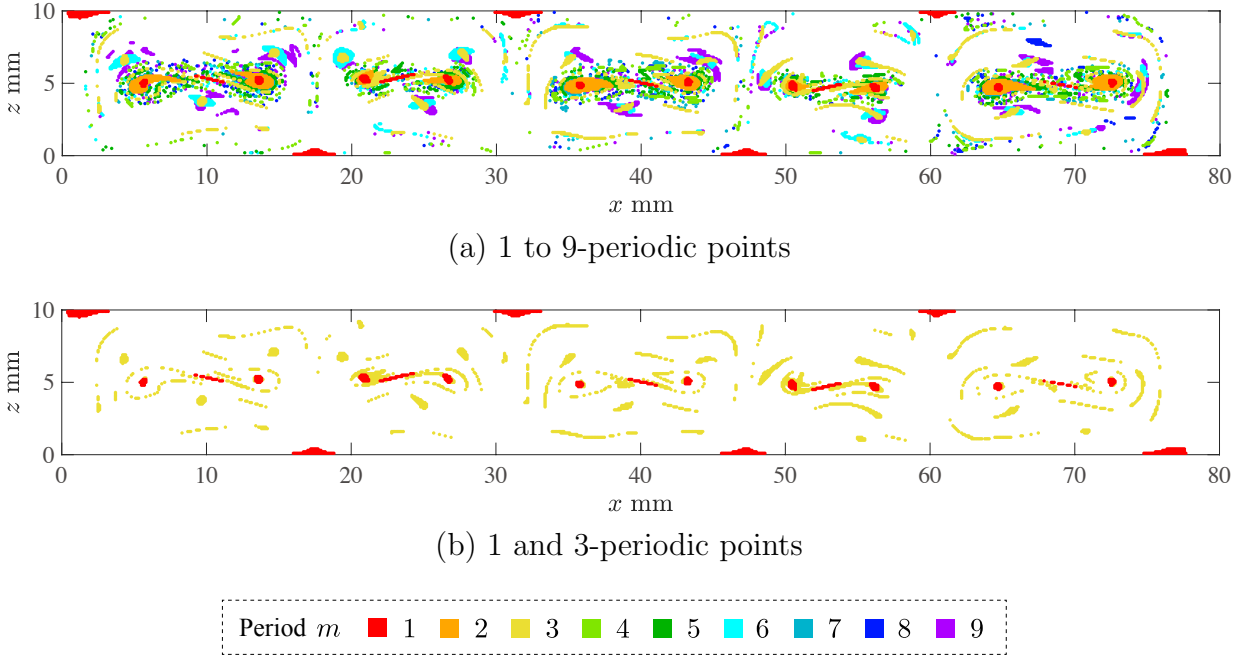


Figure 4.5.2: Periodic points in experiments

to the neighborhood of the initial position after time mT , as is shown in Fig.4.5.1. On the other hand, (4.5.2) is accompanied to distinguish m -periodic points and km -periodic points ($k \in \mathbb{N}$). Fig.4.5.2a depicts the periodic points at $t = 0$ with period $m \leq 9$, where $\delta = 0.5$ mm. The color of the plots indicates the period. Here, we focus on the 1 and 3-periodic points, which is illustrated in Fig.4.5.2b. Taking a look at Fig.4.4.3c and Fig.4.5.2b, it is observed that 1-periodic points appear around the knot and at the center of the loops of the figure-eight structures of hyperbolic LCSs, while 3-periodic points appear in clusters around them.

Elliptic LCSs in experiments. As we have seen in §2.3, the regions of KAM islands around elliptic periodic points seem to be transported stably in the perturbed Hamiltonian model. Thus, such regions may appear around some of the periodic points in experiments. Therefore, we detect elliptic LCSs around 1 and 3-periodic points in a cell which range from $x = 17$ mm to $x = 31$ mm and show them in Fig.4.5.3; see §2.3 for the definitions of elliptic LCSs. Recall that two types of cells with different width appear alternately in the layer. Here, we focus on the cell with smaller width. The initial and integration time of the LCSs are set to $t_0 = 0$ and $T_{\text{int}} = 15T$. The elliptic LCSs are detected in the same methods for the perturbed Hamiltonian model shown in §2.3 except for that flow maps in (2.3.1) are obtained by numerically integrating the measured velocity fields with 4th-order Runge-Kutta method, where the velocity at each point is approximated by linear interpolation. The radius for detecting closed solution curves on vector fields η_λ^\pm is set to $\delta = 0.1$ mm. As can be seen, elliptic LCSs appear around the clusters of 1-periodic points in the right and left in the middle of the cell and also around the three clusters of 3-periodic points. It follows that fluid particles inside them may be transported stably.

Stable transport of fluid particles inside elliptic LCSs. In order to verify that fluid particles inside elliptic LCSs are transported stably we illustrate the transport of fluid particles inside the outermost elliptic LCSs in Fig.4.5.4, where fluid particles inside each LCS is indicated in different colors. Fig.4.5.4a and Fig.4.5.4b respectively show the initial position and the position after one period of perturbation. Note that the rotation of the convection is clockwise in this cell and that the initial time for LCSs in Fig.4.5.4a and Fig.4.5.4b

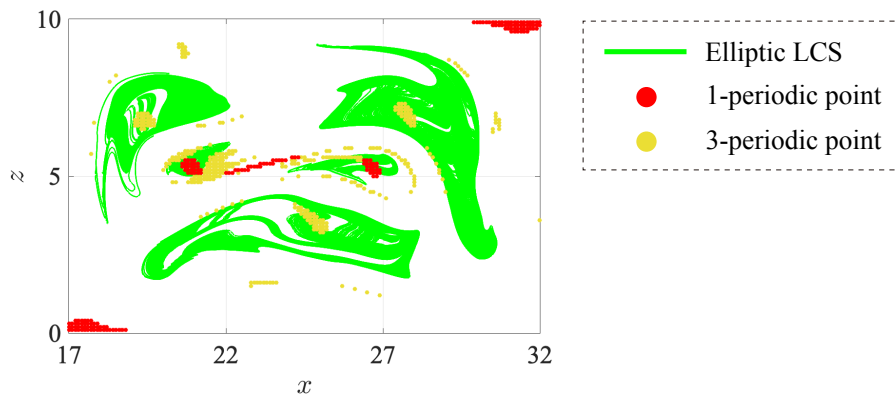


Figure 4.5.3: Elliptic LCSs and 1, 3-periodic points

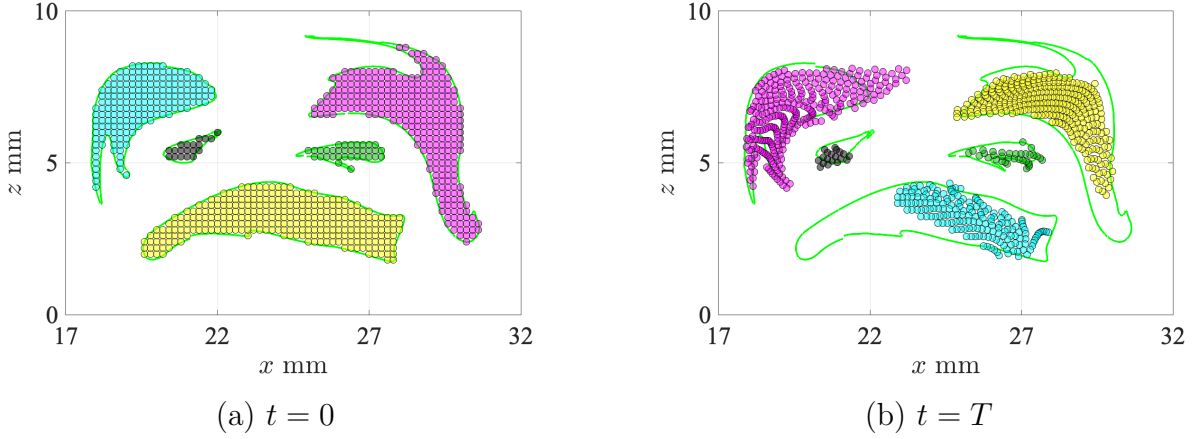


Figure 4.5.4: Transport of fluid particles inside elliptic LCSs

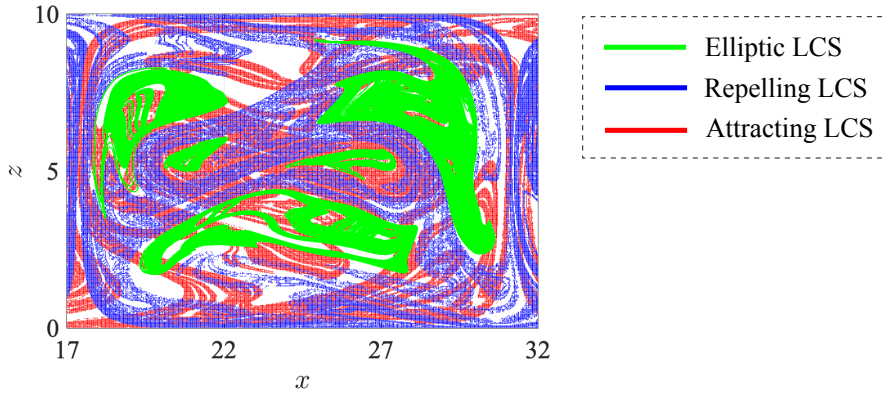


Figure 4.5.5: Elliptic and hyperbolic LCSs

are both set to $t_0 = 0$. It is observed that most of the fluid particles are transported inside elliptic LCSs after one period. In particular, those around 1-periodic points are transported inside the same LCS, while those around 3-periodic points are transported inside another LCS. Thus, fluid particles inside elliptic LCSs may be transported stably as a sort of vortex in the Lagrangian description similarly to those in the KAM islands in the perturbed Hamiltonian model. In other words, stable regions around 1 and 3-periodic points may be transported periodically with period 1 and 3 respectively. Further, since elliptic LCSs appear around elliptic periodic points in the model, we can assume that the clusters of 1-periodic points in the right and left in the middle of the cell may correspond to elliptic periodic points, while the cluster of 1-periodic points at the center corresponds to hyperbolic periodic points. It follows that the figure-eight structures of hyperbolic LCSs may correspond to entangled double homoclinic loops. We will discuss this again in Chap.5 by proposing a perturbed Hamiltonian model for experiments.

Finally, Fig.4.5.5 depicts the elliptic LCSs with hyperbolic LCSs. The integration time of the LCSs is set to $T_{\text{int}} = 15T$. We can see that elliptic LCSs appear where no repelling LCSs exist, as we have observed in the perturbed Hamiltonian model. However, some of the elliptic LCSs cross the attracting LCSs. This is probably because there is some slight flow in the direction perpendicular to the laser sheet in experiments.

4.6 Summary

In this chapter, we experimentally detect Lagrangian coherent structures (LCSs) and periodic points by using two-dimensional velocity fields of perturbed Rayleigh-Bénard convection obtained by PIV analysis, where LCSs correspond to invariant manifolds in non-autonomous systems. It is observed that hyperbolic LCSs entangle very complicatedly as homoclinic tangles around cell boundaries and create some lobes. In addition, a figure-eight structure of hyperbolic LCSs, which may correspond to an entangled double homoclinic loop, appears in the middle of each cell. Further, two types of cells with different structures appear alternately in the layer when the integration time of the LCSs is increased. It is shown that the fluid particles inside lobes are transported from one lobe to another in each period of perturbation in accordance with lobe dynamics. It follows that fluid inside lobes may be transported chaotically by horseshoe maps. In contrast, fluid inside elliptic LCSs around 1 and 3-periodic points may be transported periodically as a sort of vortex in the Lagrangian description with period 1 and 3 respectively, which is similar to the stable transport of KAM islands in the perturbed Hamiltonian model.

Chapter 5

Perturbed Hamiltonian model for experiments

In Chap.2 and Chap.3 we have analyzed the simple Hamiltonian model of perturbed Rayleigh-Bénard convection originally proposed by Solomon and Gollub [63] and introduced by Camassa and Wiggins [8]. However, it was clarified in Chap.4 that invariant structures in such model do not precisely match with those observed in experiments. Therefore, in this chapter, we propose a novel perturbed Hamiltonian model that qualitatively elucidates the experimental results better. Furthermore, we analyze the invariant structures of the proposed model and clarify the global structures of fluid transport in perturbed Rayleigh-Bénard convection.

5.1 Model of perturbed Rayleigh-Bénard convection

Vertical velocity on the horizontal center line in experiments. As we have seen in Chap.4, a figure-eight structure of hyperbolic LCSs appears in the middle of each cell in experiments, but it does not show up in the simple model proposed by Solomon and Gollub [63] and Camassa and Wiggins [8]. This is probably because the center of vortices in each cell oscillates side by side more widely in experiments than in the simple model. Therefore, we aim to make the center of vortices oscillate widely in our model as in experiments. To do this, we focus on velocity w in z direction on the horizontal center line $z = 5$ mm from $x = 1$ mm to $x = 60.5$ mm, which corresponds to the range of four cells. Fig.5.1.1 illustrates the time variation of velocity w on such line. The upper convex peaks around $x = 1, 31, 60$ mm and the downward ones around $x = 17, 47$ mm correspond to the upward and downward flow respectively, while the points with $w = 0$ roughly correspond to the center of vortices in each cell. We can see that such points move side by side with

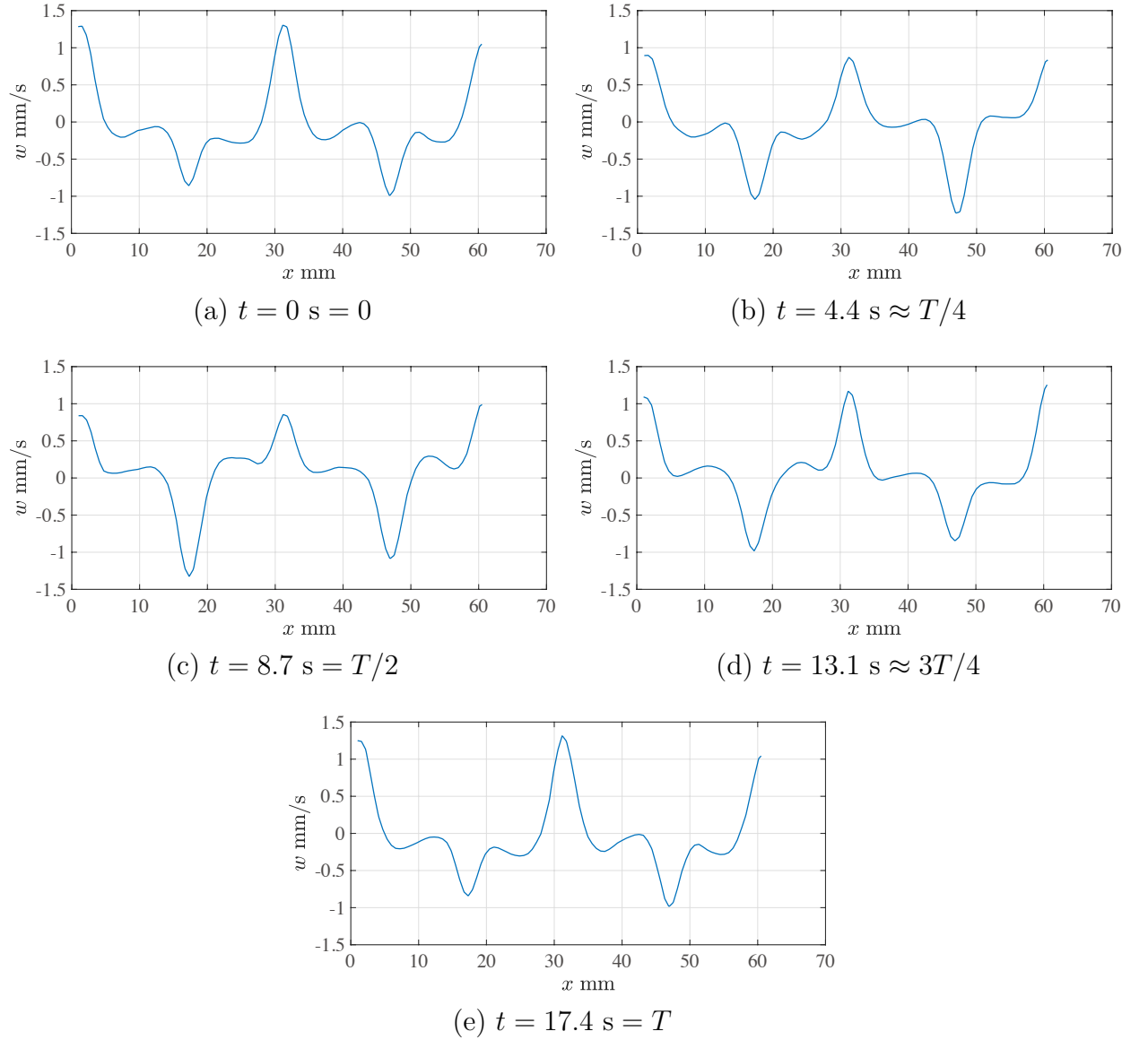


Figure 5.1.1: Velocity w on line $z = 5 \text{ mm}$ in experiments

time t , which corresponds to the oscillation of vortices. Next, Fig. 5.1.2 shows the time-variation of the spectrum of velocity w in Fig. 5.1.1. Note that the horizontal axis of the spectrum is spatial frequency. It is observed that the peaks at $f_1 = 0.0336 \text{ 1/mm}$ and $f_3 = 3f_1 = 0.1008 \text{ 1/mm}$ are almost independent of time t . However, the peak at $f_2 = 2f_1 = 0.0672 \text{ 1/mm}$ depends on t , in other words, the height of the peak decreases at $t = 4.4 \text{ s} \approx T/4$ and $t = 13.1 \text{ s} \approx 3T/4$ compared to that at $t = 0, T/2, T$.

Vertical velocity on the horizontal center line in the model. Now, let us recall the Hamiltonian model of steady Rayleigh-Bénard convection. As already mentioned in Chap. 2, by assuming the stress-free boundary condition, the

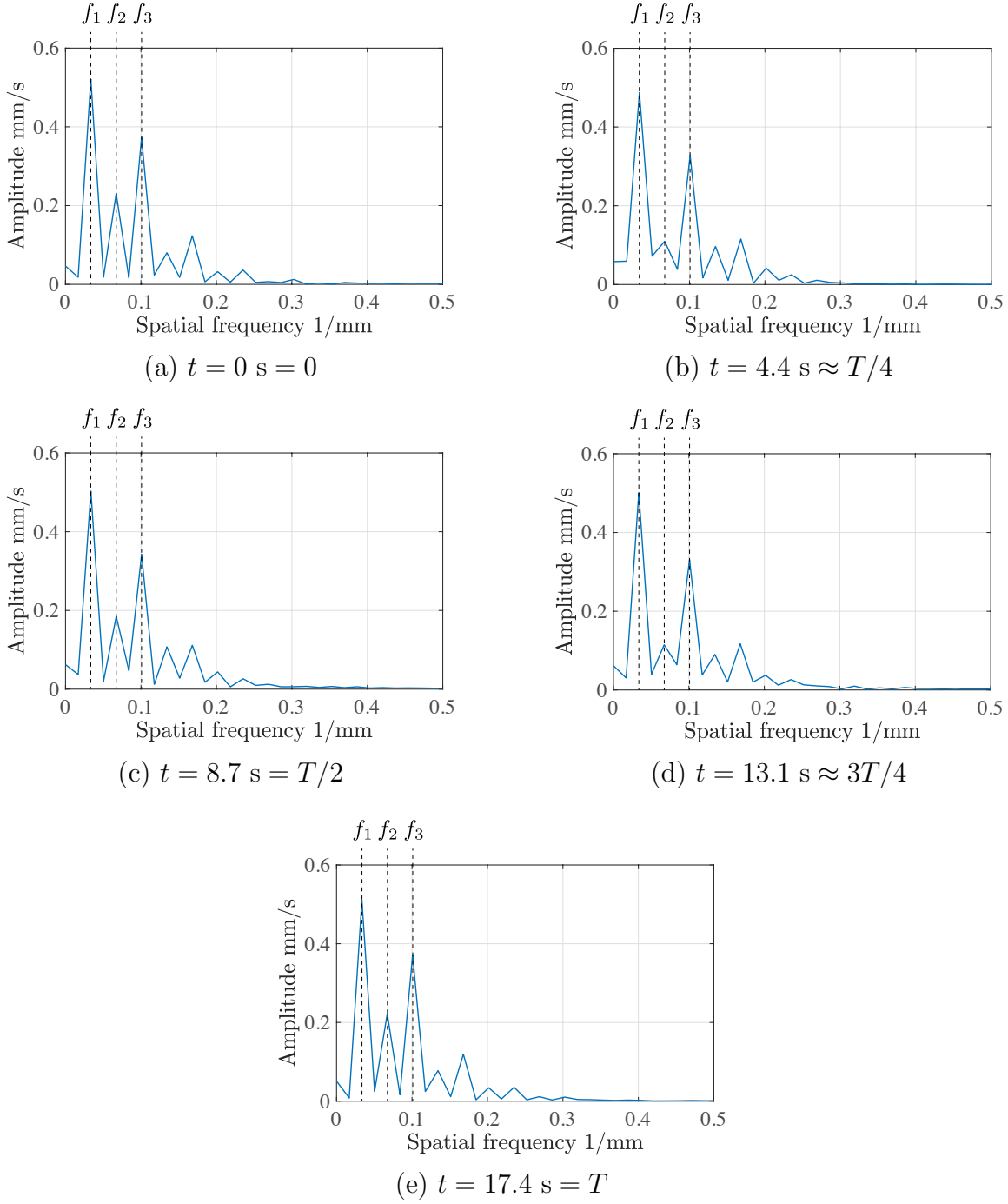


Figure 5.1.2: Spectrum of velocity w on line $z = 5$ mm in experiments

two-dimensional steady Rayleigh-Benard convection can be modeled as a Hamiltonian system

$$\frac{dx}{dt} = -\frac{\partial H_0(x, z)}{\partial z} = -\frac{A\pi}{k} \sin(kx) \cos(\pi z),$$

$$\frac{dz}{dt} = \frac{\partial H_0(x, z)}{\partial x} = A \cos(kx) \sin(\pi z),$$

where the Hamiltonian is given by

$$H_0(x, z) = \frac{A}{k} \sin(kx) \sin(\pi z),$$

and $x \in \mathbb{R}, z \in [0, 1]$. Then, the vertical velocity on the horizontal center line becomes

$$\left. \frac{dz}{dt} \right|_{z=\frac{1}{2}} = A \cos(kx).$$

In the spectrum of velocity w on $z = 5$ mm in experiments the peaks at f_1 and $f_3 = 3f_1$ are independent of time t but the peak at $f_2 = 2f_1$ are dependent. Therefore, we define the vertical velocity on the horizontal center line in our model as

$$\left. \frac{dz}{dt} \right|_{z=\frac{1}{2}} = A \cos(kx) + \varepsilon \{3k \cos(3kx) + 2k \cos(\omega t) \cos(2kx)\}, \quad (5.1.1)$$

where ε indicates the magnitude of perturbations. Notice that (5.1.1) corresponds to the velocity of steady Rayleigh-Bénard convection when $\varepsilon = 0$. The coefficient of $\cos(3kx)$ and $\cos(\omega t) \cos(2kx)$ is set to $3k$ and $2k$ respectively, since the height of the peaks at f_3 and f_2 in the spectrum is roughly the ratio of three to two. Fig. 5.1.3 shows velocity w on $z = 1/2$ in the model for two cells. The parameters are set to $A = 8, k = 2.1, T = 2\pi/\omega = 0.15, \varepsilon = 0.6$ according to the experimental data. It is observed that the model reproduce the experimental results qualitatively.

Construction of the Hamiltonian of the model. Let us construct the perturbed Hamiltonian system from (5.1.1). Now that no fluid can pass through the upper and lower boundaries,

$$\left. \frac{dz}{dt} \right|_{z=0} = \left. \frac{dz}{dt} \right|_{z=1} = 0$$

is necessary. Thus, we multiply $\sin(\pi z)$ to (5.1.1) and let

$$\begin{aligned} \frac{dz}{dt} &= [A \cos(kx) + \varepsilon \{3k \cos(3kx) + 2k \cos(\omega t) \cos(2kx)\}] \sin(\pi z) \\ &:= f(x, z, t). \end{aligned}$$

Then, the Hamiltonian $H(x, z, t)$ can be obtained as

$$\begin{aligned} H(x, z, t) &= \int f(x, z, t) dx \\ &= H_0(x, z) + \varepsilon \{\sin(3kx) + \cos(\omega t) \sin(2kx) + \mu\} \sin(\pi z) + g(z, t), \end{aligned}$$

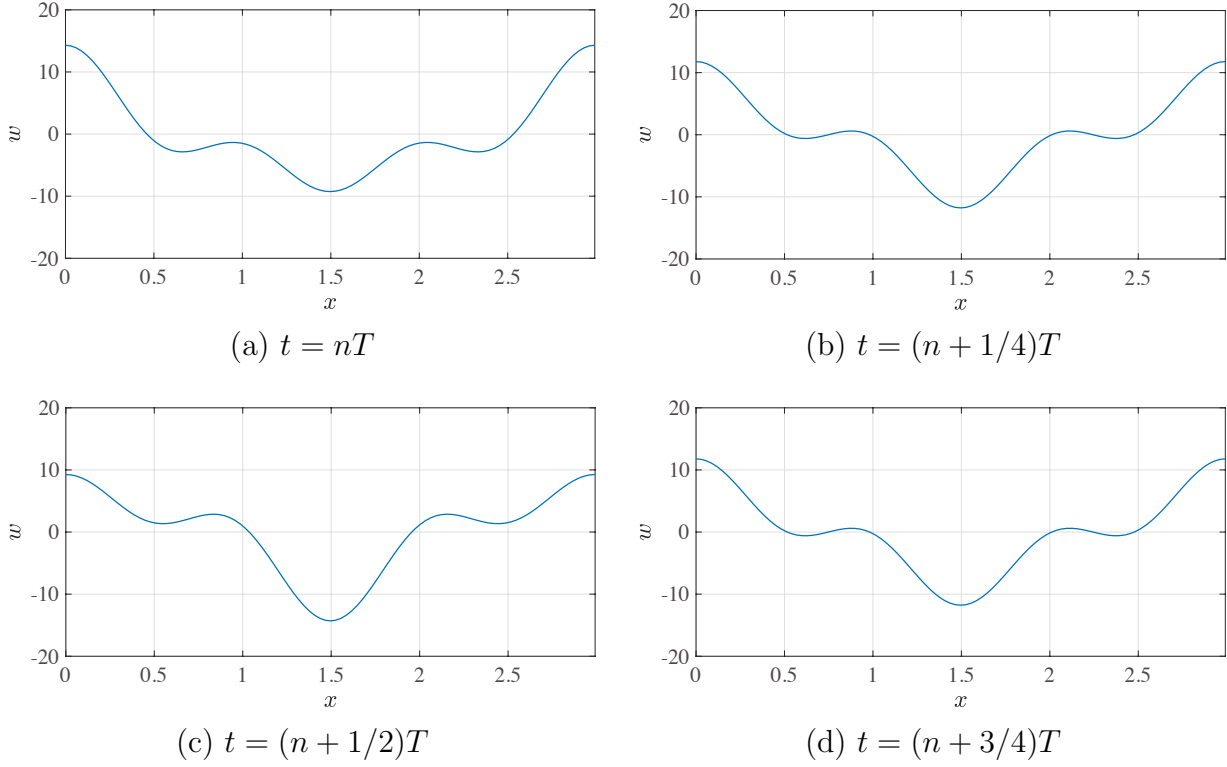


Figure 5.1.3: Velocity w on $z = 1/2$ in the model ($n \in \mathbb{Z}$)

where $g(z, t)$ is some function of z and t , and μ is some constant number associated with the width of cells. When $\mu > 0$ two types of cells with different width appear alternately in the layer, while the width becomes uniform when $\mu = 0$. We let μ variable, since the width of cells sometimes changes between experimental cases. Then, the horizontal velocity can be calculated as

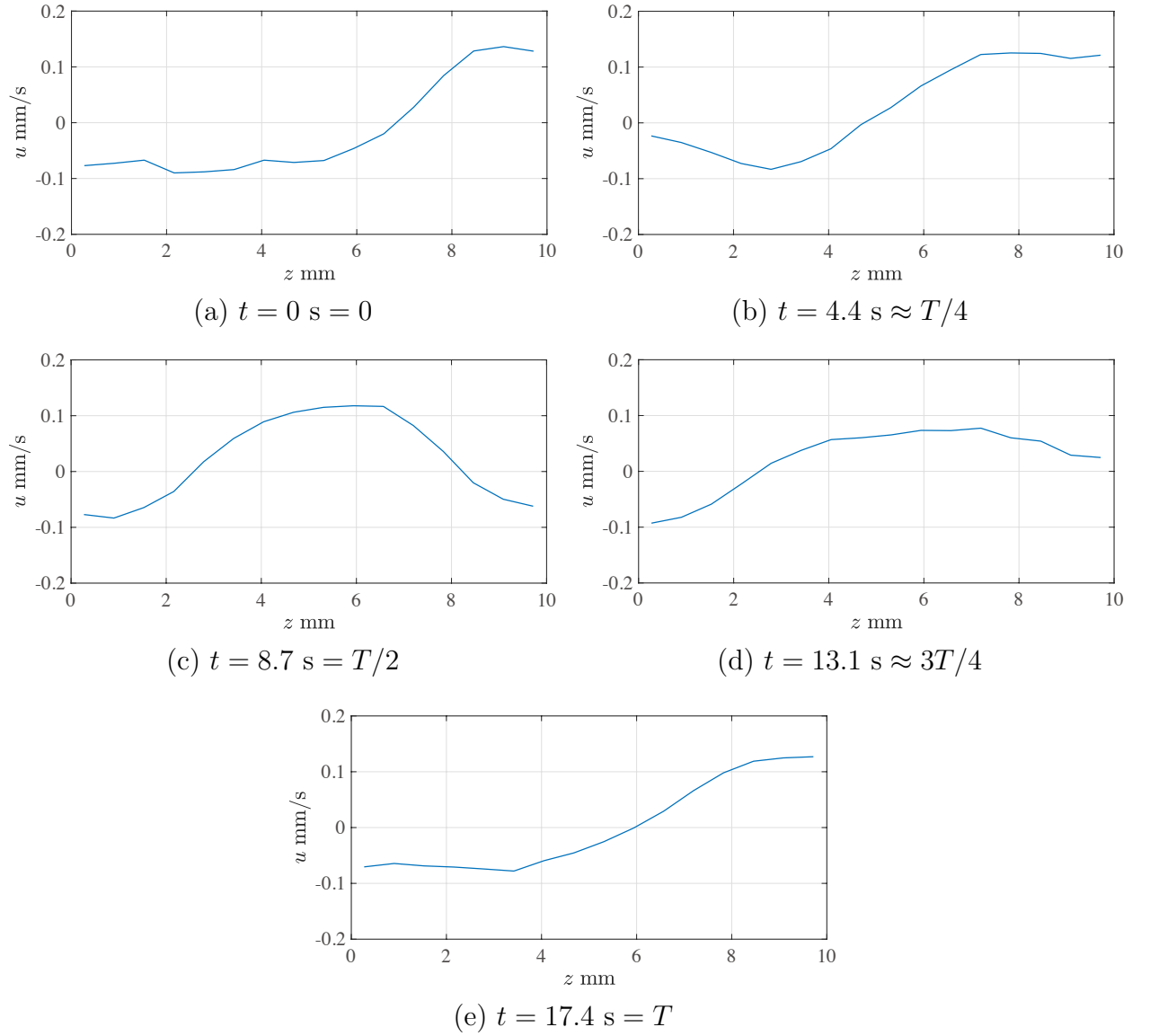
$$\begin{aligned} \frac{dx}{dt} &= -\frac{\partial H(x, z, t)}{\partial z} \\ &= -\frac{A\pi}{k} \sin(kx) \cos(\pi z) \\ &\quad - \varepsilon\pi \{ \sin(3kx) + \cos(\omega t) \sin(2kx) + \mu \} \cos(\pi z) + h(z, t), \end{aligned}$$

where

$$h(z, t) = -\frac{\partial g(z, t)}{\partial z}.$$

Thus, the horizontal velocity on a vertical line $x = n\pi/k$ ($n \in \mathbb{Z}$) near a cell boundary becomes

$$\left. \frac{dx}{dt} \right|_{x=\frac{n\pi}{k}} = -\varepsilon\pi\mu \cos(\pi z) + h(z, t).$$

Figure 5.1.4: Velocity u on line $x = 47 \text{ mm}$ in experiments

Now let us take a look at the horizontal velocity near a cell boundary in experiments, in particular velocity u in x direction on $x = 47 \text{ mm}$, which is shown in Fig. 5.1.4. It is observed that the velocity is perturbed. In order to reproduce such perturbations in the model we define

$$h(z, t) = \varepsilon \pi \cos(\omega t) \cos(2\pi z).$$

Fig. 5.1.5 depicts velocity u on $x = n\pi/k$ ($n \in \mathbb{Z}$) in the model when $h(z, t)$ is defined as above, where the parameters are set to $\varepsilon = 0.6$, $T = 2\pi/\omega = 0.15$. We can see that the model reproduces the perturbations qualitatively. Then, $g(z, t)$ can be calculated as

$$g(z, t) = - \int h(z, t) dz = -\frac{1}{2} \varepsilon \cos(\omega t) \sin(2\pi z).$$

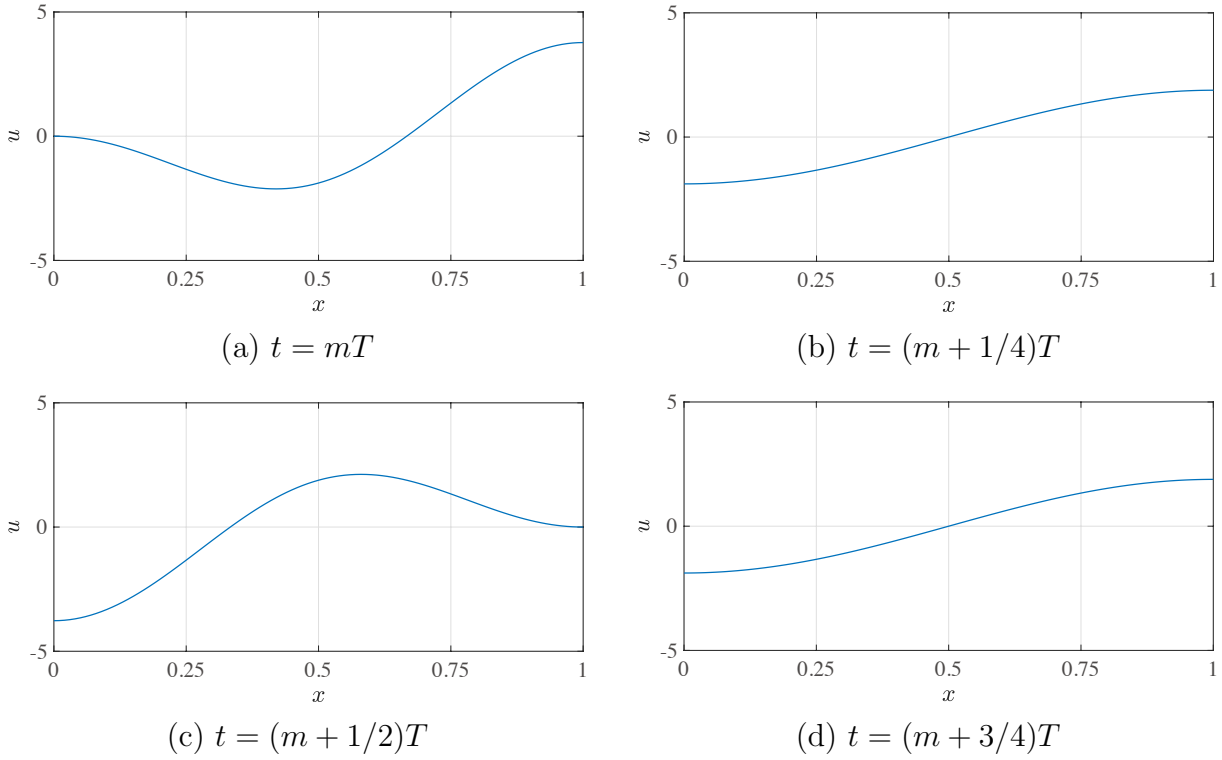


Figure 5.1.5: Velocity u on line $x = n\pi/k$ ($n \in \mathbb{Z}$) in the model ($m \in \mathbb{Z}$)

Perturbed Hamiltonian model for experiments. Hence, perturbed Rayleigh-Bénard convection is modeled as a perturbed Hamiltonian system

$$\begin{aligned}
 \frac{dx}{dt} &= -\frac{\partial H(x, z, t)}{\partial z} = -\frac{A\pi}{k} \sin(kx) \cos(\pi z) \\
 &\quad -\varepsilon\pi \{\sin(3kx) + \cos(\omega t) \sin(2kx) + \mu\} \cos(\pi z) \\
 &\quad +\varepsilon\pi \cos(\omega t) \cos(2\pi z), \\
 \frac{dz}{dt} &= \frac{\partial H(x, z, t)}{\partial x} = A \cos(kx) \sin(\pi z) \\
 &\quad +\varepsilon \{3k \cos(3kx) + 2k \cos(\omega t) \cos(2kx)\} \sin(\pi z),
 \end{aligned} \tag{5.1.2}$$

where the Hamiltonian is given by

$$\begin{aligned}
 H(x, z, t) &= H_0(x, z) \\
 &\quad +\varepsilon [\sin(3kx) + \cos(\omega t) \{\sin(2kx) - \cos(\pi z)\} + \mu] \sin(\pi z),
 \end{aligned} \tag{5.1.3}$$

and $x \in \mathbb{R}$ and $z \in [0, 1]$. Here, the Hamiltonian $H_0(x, z)$ for steady Rayleigh-Bénard convection is given by

$$H_0(x, z) = \frac{A}{k} \sin(kx) \sin(\pi z).$$

In particular, velocity in x direction around cell boundaries and velocity in z direction on the horizontal center line can be obtained from (5.1.2) as

$$\begin{aligned} \left. \frac{dx}{dt} \right|_{x=\frac{n\pi}{k}} &= \varepsilon \pi \{ \cos(\omega t) \cos(2\pi z) - \mu \cos(\pi z) \}, \\ \left. \frac{dz}{dt} \right|_{z=\frac{1}{2}} &= A \cos(kx) + \varepsilon \{ 3k \cos(3kx) + 2k \cos(\omega t) \cos(2kx) \} \end{aligned} \quad (5.1.4)$$

respectively.

Physical meanings of each term in the Hamiltonian. Let us describe the physical meanings of each term in Hamiltonian $H(x, z, t)$ in (5.1.3). To do this we expand (5.1.3) and label each term as I, II, \dots , V as follows:

$$\begin{aligned} H(x, z, t) = & \underbrace{\frac{A}{k} \sin(kx) \sin(\pi z)}_{\text{Term I: Hamiltonian of steady Rayleigh-Bénard convection}} \\ & + \underbrace{\varepsilon \sin(3kx) \sin(\pi z)}_{\text{Term II: Stretch the streamlines in the horizontal direction}} \\ & + \underbrace{\varepsilon \cos(\omega t) \sin(2kx) \sin(\pi z)}_{\text{Term III: Oscillate the center of vortices}} \\ & - \underbrace{\varepsilon \cos(\omega t) \cos(\pi z) \sin(\pi z)}_{\text{Term IV: Perturb the horizontal velocity around cell boundaries}} \\ & + \underbrace{\varepsilon \mu \sin(\pi z)}_{\text{Term V: Determine the width of cells}}. \end{aligned} \quad (5.1.5)$$

We will explain the physical meanings shown in the above later on. Then, we expand (5.1.4) as follows:

$$\left. \frac{dx}{dt} \right|_{x=\frac{n\pi}{k}} = \underbrace{\varepsilon \pi \cos(\omega t) \cos(2\pi z)}_{\text{Originate from IV}} - \underbrace{\varepsilon \pi \mu \cos(\pi z)}_{\text{Originate from V}}, \quad (5.1.6)$$

$$\left. \frac{dz}{dt} \right|_{z=\frac{1}{2}} = \underbrace{A \cos(kx)}_{\text{Originate from I}} + \underbrace{3\varepsilon k \cos(3kx)}_{\text{Originate from II}} + \underbrace{2\varepsilon k \cos(\omega t) \cos(2kx)}_{\text{Originate from III}}. \quad (5.1.7)$$

Each term in (5.1.6) originates from terms IV and V in (5.1.5), while each one in (5.1.7) originates from terms I, II, and III.

Obviously, term I is the Hamiltonian of steady Rayleigh-Bénard convection. Term II stretches the streamlines in each cell in the horizontal direction, since $3\varepsilon k \cos(3kx)$ in (5.1.7), which originates from term II, decreases the vertical velocity on the horizontal center line in the middle of each cell independently of time t . Time-periodic terms III and IV perturb the velocity fields. In particular, term III oscillates the center of vortices side by side. It is because $2\varepsilon k \cos(\omega t) \cos(2kx)$ in (5.1.7), which originates from term III, corresponds to the time-dependent peak at f_2 in the spectrum of velocity w on the horizontal center line. On the other hand, term IV perturbs the horizontal velocity around cell boundaries, since $\varepsilon\pi \cos(\omega t) \cos(2\pi z)$ in (5.1.6), which originates from term IV, is the only time-periodic term in the equation. The last term V determines the width of cells. Two types of cells with different width appear alternately when $\mu > 0$, while the width becomes uniform when $\mu = 0$.

Vector fields and streamlines of the model. Fig.5.1.6 and Fig.5.1.7 depict the time-variation of vector fields and streamlines of the model in (5.1.2), where the horizontal section is limited to $0 \leq x \leq 2\pi/k$, which corresponds to the width of two adjacent cells. Note that there is no loss of generality to investigate only two cells, since there is a topological isomorphism among cells. The parameters are set to $A = 8, k = 2.1, T = 2\pi/\omega = 0.15, \varepsilon = 0.6, \mu = 1$ according to the experimental data, where they are fixed throughout this

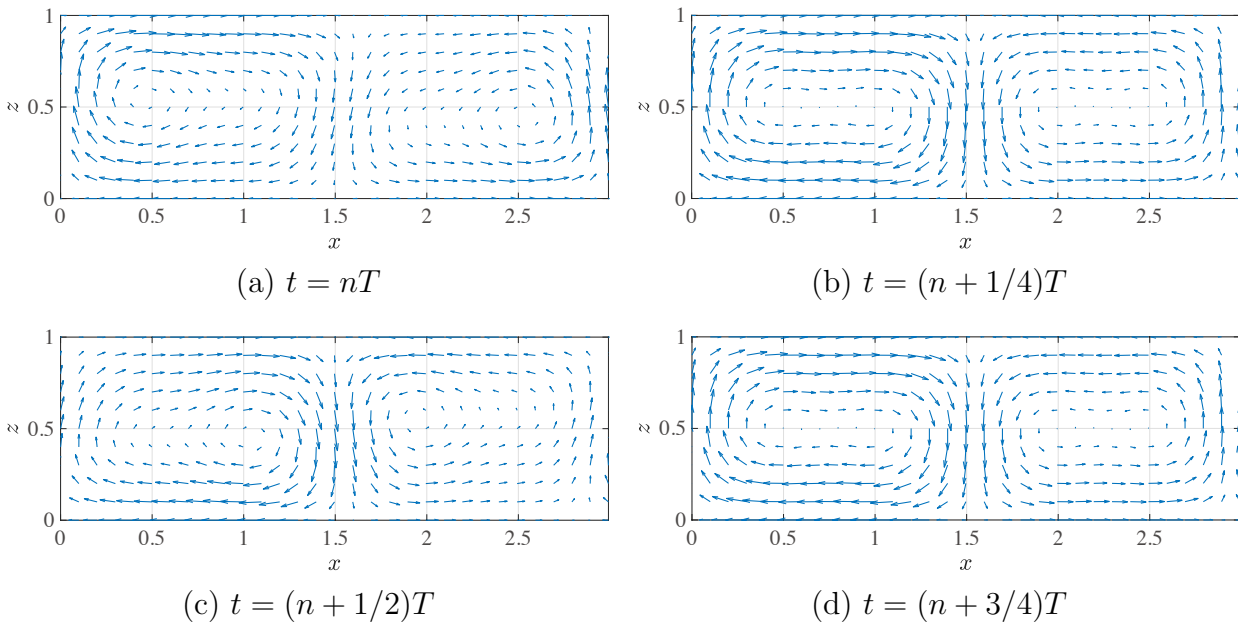
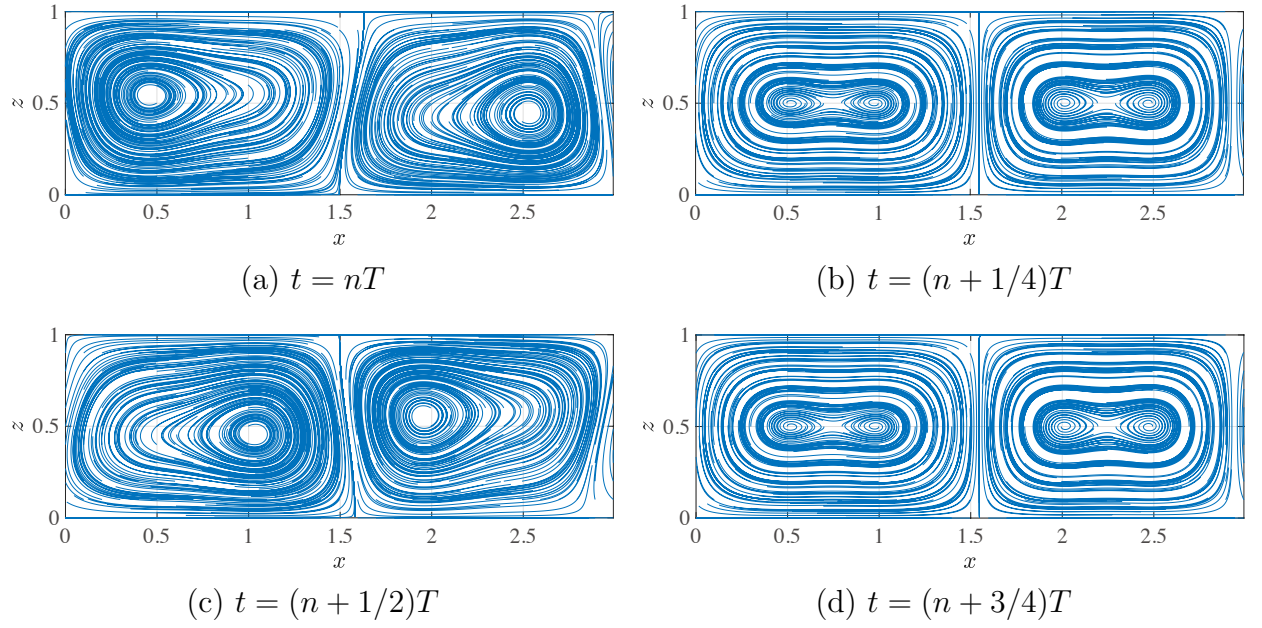


Figure 5.1.6: Velocity fields of the model ($n \in \mathbb{Z}$)

Figure 5.1.7: Streamlines of the model ($n \in \mathbb{Z}$)

thesis for this model. It is observed in accordance with the experimental results that the center of vortices in each cell oscillates side by side widely and that velocity around cell boundaries increases when the center of vortices moves close to the boundaries.

5.2 Invariant structures in the model

FTLE fields and hyperbolic LCSs in perturbed Hamiltonian model. Fig.5.2.1 and Fig.5.2.2 illustrate the FTLE fields of the model in (5.1.2) with forward- and backward-time integration. The horizontal section is limited to $0 \leq x \leq 2\pi/k$, which corresponds to the width of two adjacent cells. The initial and integration time of the FTLE is set to $t_0 = 0$ and $T_{\text{int}} = T, 2T, 3T, 5T, 8T, 15T$ respectively, where $T = 0.15$ is the period of the perturbation. Further, Fig.5.2.3 depicts the hyperbolic LCSs detected from the FTLE fields in Fig.5.2.1 and Fig.5.2.2. The repelling and attracting LCSs are illustrated in blue and red respectively. It is observed in accordance with the experimental results that the hyperbolic LCSs entangle as homoclinic tangles around cell boundaries and that they are asymmetric with each other with respect to the horizontal center line. Further, we can see that a figure-eight structure appears in the middle of each cell and that two types of cells with different structures appear alternately in the layer. Hence, the perturbed Hamiltonian model in (5.1.2) elucidates the experimental results qualitatively.

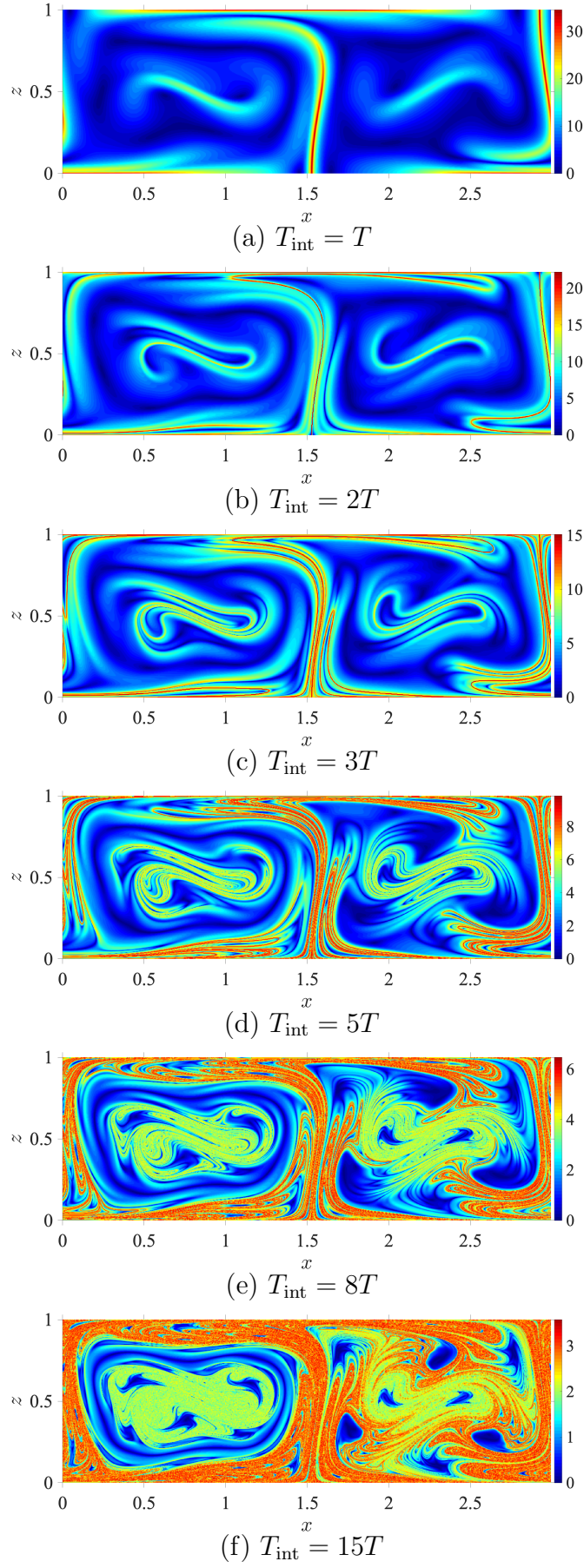


Figure 5.2.1: Forward FTLE fields of the model

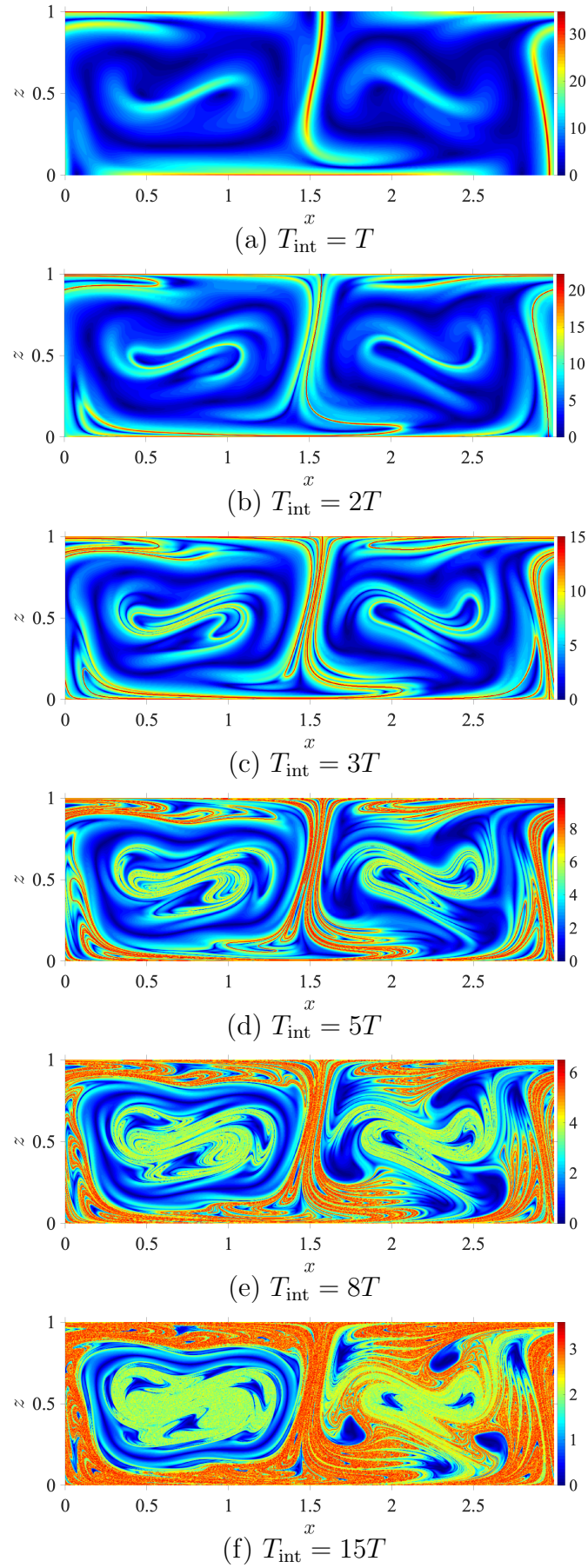


Figure 5.2.2: Backward FTLE fields of the model

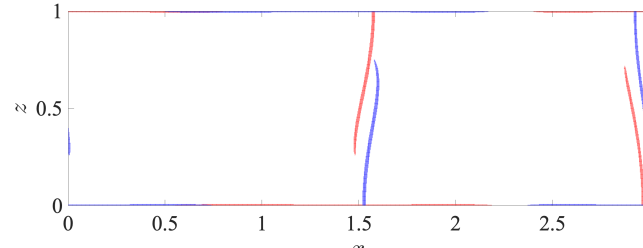
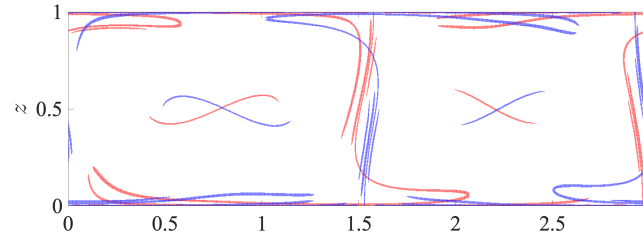
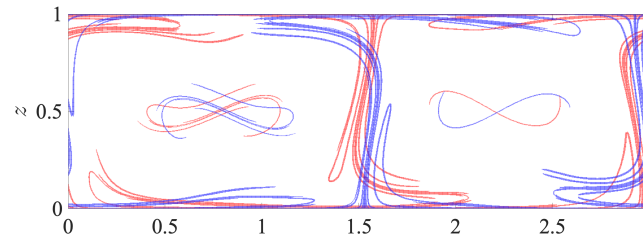
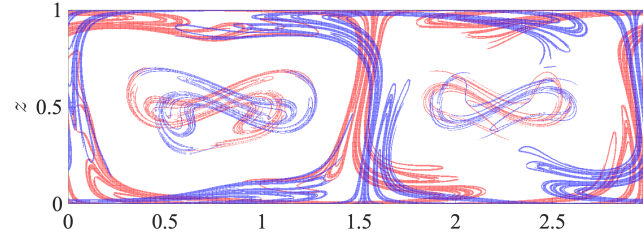
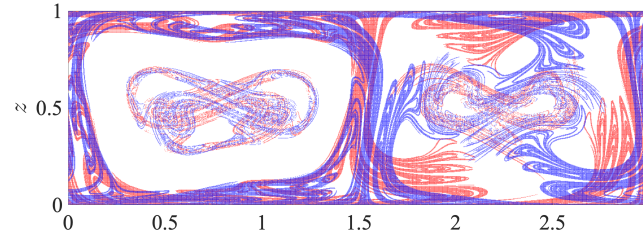
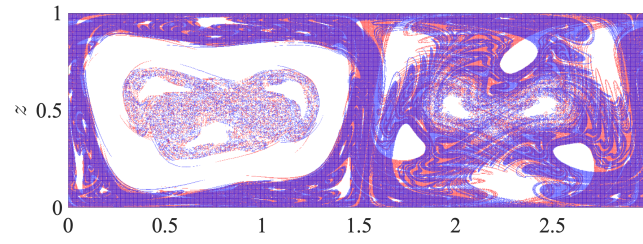
(a) $T_{\text{int}} = T$ (b) $T_{\text{int}} = 2T$ (c) $T_{\text{int}} = 3T$ (d) $T_{\text{int}} = 5T$ (e) $T_{\text{int}} = 8T$ (f) $T_{\text{int}} = 15T$

Figure 5.2.3: Hyperbolic LCSs in the model

Periodic points in perturbed Hamiltonian model. Next, we investigate the periodic fluid transport in the perturbed Hamiltonian model in (5.1.2). Fig.5.2.4 depicts the image of Poincaré section by Poincaré maps and the detected periodic points with period $m \leq 9$, where the color and the symbols of plots denote the period m and the type of periodic points. In particular, we illustrate the 1 and 3-periodic points with the image of Poincaré section in Fig.5.2.4b to show the structures clearly. Here, the Poincaré map is defined as a flow map from $t = t_0$ to $t = t_0 + T$ similarly as in the model in Chap.2 and Chap.3, where T is the period of the perturbation. In addition, the periodic points are numerically detected in the same methods for that model. The initial time and the number of recurrences due to Poincaré maps is set to $t_0 = 0$ and $N = 1000$ respectively. Taking a look at Fig.5.2.3 and Fig.5.2.4b, it is observed that 1-periodic points appear around the knot and at the center

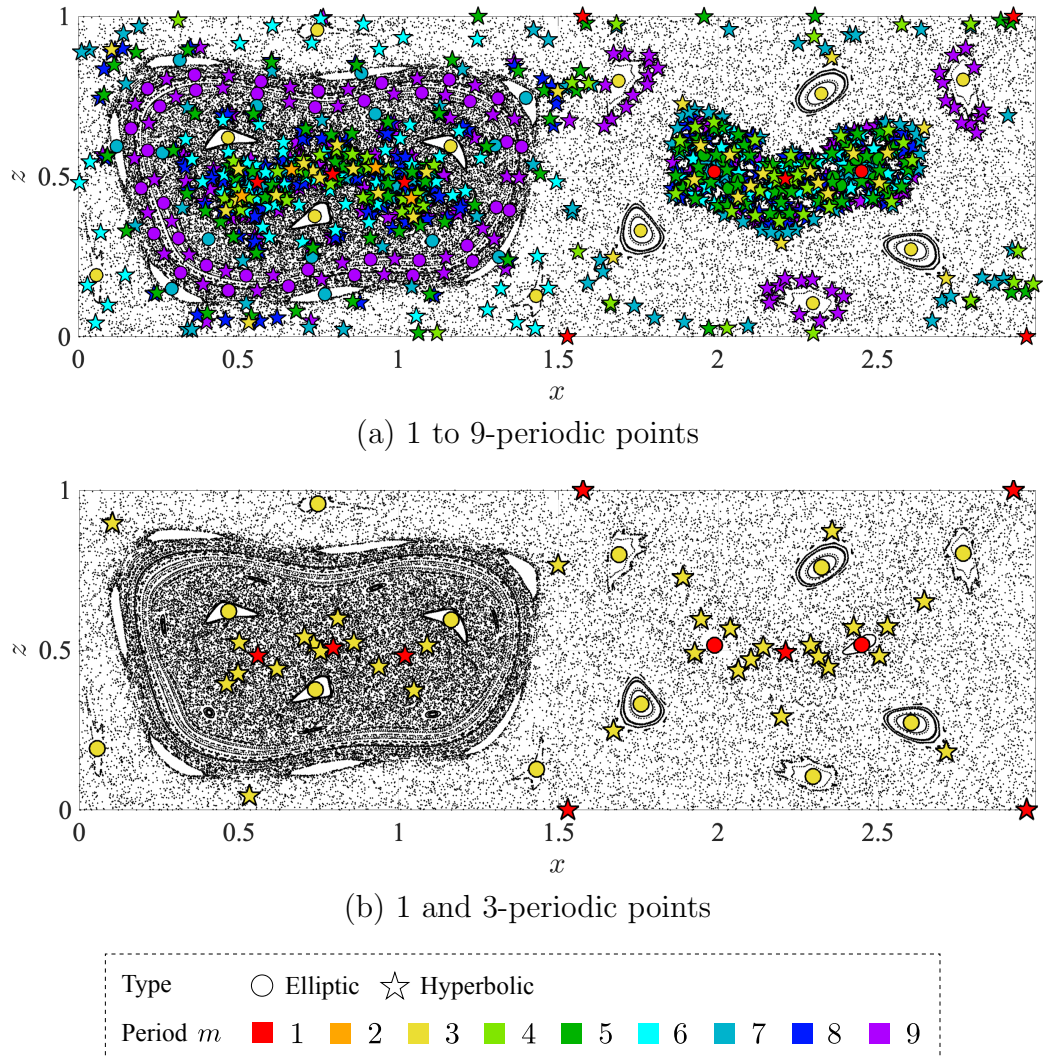


Figure 5.2.4: Periodic points in the model

of the loops of the figure-eight structures of hyperbolic LCSs in accordance with the experimental results. Further, 1-periodic points in the right and left in the middle of the right cell is elliptic, while that in the middle is hyperbolic. This implies that the figure-eight structure in the right cell may correspond to an entangled double homoclinic loop. However, the one in the left cell may not correspond to it, since all the 1-periodic points in the middle of the left cell are hyperbolic. We will seek the figure-eight structures in detail in future works. In Fig.5.2.4b we can see that 3-periodic points exist around the 1-periodic points as in experiments, though the number and the position of the periodic points are partly different from those in experiments.

Elliptic LCSs in perturbed Hamiltonian model. Finally, let us take a look at the elliptic LCSs in the model, which is depicted in Fig.5.2.5. The initial time of the LCSs is $t_0 = 0$ and the integration time is set to $T_{\text{int}} = 100T, 300T$ for those around 1 and 3-periodic points respectively. The elliptic LCSs are numerically detected in the same methods for the model proposed by Solomon and Gollub [63] and Camassa and Wiggins [8] in Chap.2. The radius for detecting closed solution curves on vector fields η_λ^\pm is set to $\delta = 0.001$. It is observed that elliptic LCSs appear around 1-periodic points in the right and left in the middle of the cell in accordance with the experimental results. Further, we can see that they appear around some of the 3-periodic points as in experiments, though the number and the position of stable transport regions are partly different from those in experiments. It follows that regions inside elliptic LCSs may be transported stably as a sort of vortex in the Lagrangian description. Lastly, Fig.5.2.6 illustrates the elliptic LCSs with

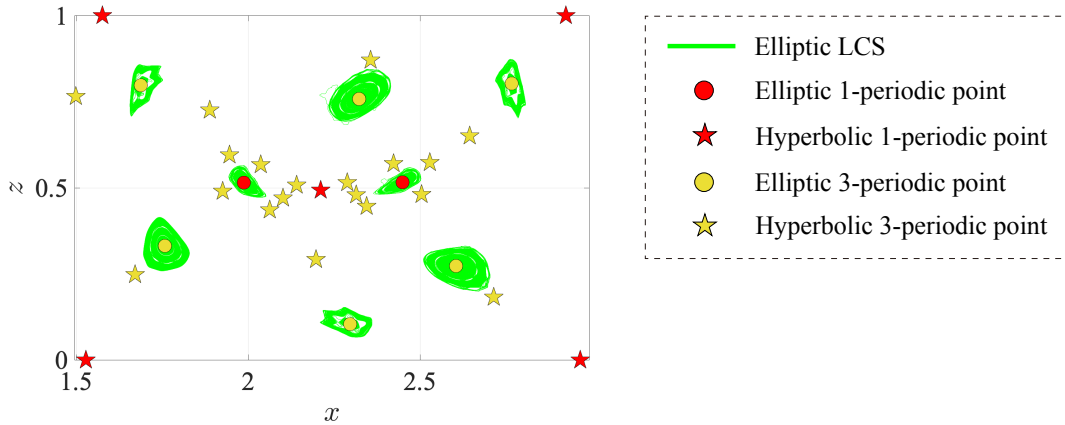


Figure 5.2.5: Elliptic LCSs and 1, 3-periodic points

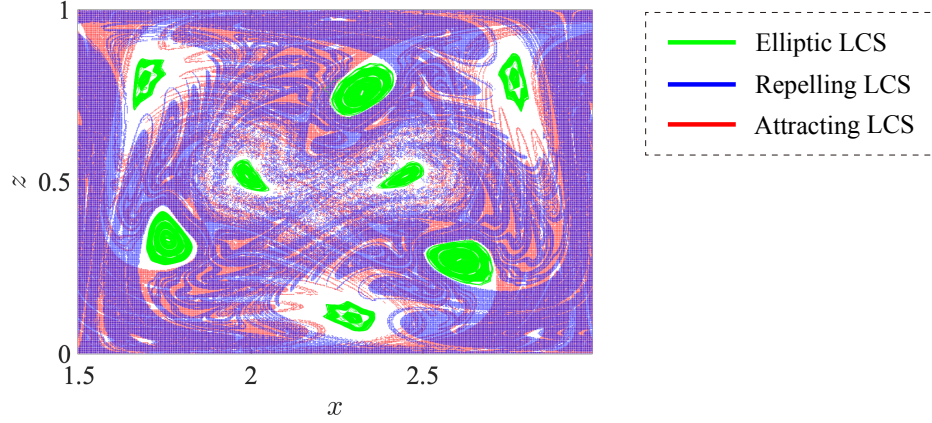


Figure 5.2.6: Elliptic and hyperbolic LCSs

hyperbolic LCSs, where the integration time of the hyperbolic LCSs is set to $T_{\text{int}} = 15T$. It is observed that elliptic LCSs appear where no hyperbolic LCSs exist. This is consistent with the fact that hyperbolic and elliptic LCSs are associated with chaotic and stable fluid transport respectively. Hence, the perturbed Hamiltonian model proposed in this thesis qualitatively elucidates the structures of fluid transport observed in experiments.

5.3 Summary

In this chapter, a novel two-dimensional perturbed Hamiltonian model for Rayleigh-Bénard convection is proposed to elucidate the experimental results, since in experiments we observe some structures which is different from those in the model investigated in Chap.2 and Chap.3. We develop the model by qualitatively representing the velocity fields obtained by PIV analysis and discuss the physical meanings of each term in the Hamiltonian. The proposed model qualitatively elucidates the invariant structures observed in experiments. In particular, figure-eight structures of hyperbolic LCSs and two types of cells with different structures appear in the model. In addition, elliptic LCSs exist around 1 and 3-periodic points similarly in experiments.

Chapter 6

Conclusions and future plans

6.1 Conclusions

In this thesis we have explored the global structures of fluid transport in perturbed Rayleigh-Bénard convection theoretically, numerically, and experimentally by focusing on invariant structures such as periodic orbits and Lagrangian coherent structures.

First in Chap.2 and Chap.3, we investigated the periodic orbits in a two-dimensional perturbed Hamiltonian model originally proposed by Solomon and Gollub [63] and introduced by Camassa and Wiggins [8]. Especially in Chap.2, we detected the periodic points on the Poincaré section and analyzed the associated periodic orbits from the perspectives of resonance and symmetry. We have gained the following results in Chap.2:

- KAM tori associated with elliptic m -periodic points have twisted structures in the extended phase space $\mathcal{M} = M \times S^1$, which denotes that each region of KAM islands are mapped to the same region after m times of Poincaré maps. From a physical point of view, they are transported periodically as a sort of vortex in the Lagrangian description.
- Elliptic LCSs appear similarly as KAM curves in the model. It follows that KAM curves and KAM islands may correspond to elliptic LCSs and Lagrangian vortices respectively.
- We propose a theorem regarding the symmetries of n/m -resonant orbits; namely, if the projection of an m -periodic orbit onto the original phase space M is symmetric with respect to the horizontal and vertical center lines of a cell, the period m and the winding number n of the orbit are both odd. It follows that m -periodic orbits appear in symmetric pairs when either m or n is even.

Then in Chap.3, we clarified the global bifurcations of periodic orbits associated with parameter ε , which is the amplitude of the perturbation. We have gained the following results in Chap.3:

- When the amplitude ε of the perturbation is increased, the m -periodic points associated with the main KAM island I_1 disappear one after another by fold bifurcations and seem to vary to an elliptic 1-periodic point at the center of I_1 .
- When ε is increased, 3ℓ -periodic points ($\ell = 2, 3, 4, 5$) are generated one after another by fold bifurcations around the elliptic 3-periodic points at the center of KAM islands I_2, I_3 , and I_4 , where the 3-periodic points themselves also bifurcate in fold and flip bifurcations after that.
- Periodic points associated with other islands bifurcate one after another by fold and flip bifurcations and most of them vary to unstable ones, when ε is increased. Some of them generate more orbits as in the fold bifurcations of 5-periodic points, while some others generate orbits with larger periods as in the flip bifurcations of 4-periodic points. Hence, the bifurcations of periodic points that may not be associated with I_1 may be the main factor that makes the fluid transport complicated when ε is increased.

Next in Chap.4, we experimentally detected Lagrangian coherent structures and periodic points in perturbed Rayleigh-Bénard convection by using two-dimensional velocity data obtained by PIV analysis in order to clarify the global structures of chaotic and stable fluid transport. We have gained the following results in Chap.4:

- Hyperbolic LCSs which are asymmetric with respect to the horizontal center line entangle with each other as homoclinic tangles around cell boundaries and create some lobes. In addition, a figure-eight structure of hyperbolic LCSs, which may correspond to an entangled double homoclinic loop, appears in the middle of each cell.
- When the integration time is increased, hyperbolic LCSs entangle with each other very complicatedly and two types of cells with different structures appear alternately in the layer. One type are those which figure-eight structure in the middle of each cell entangle with the LCSs around cell boundaries, while the other type are those which they do not so much.

- Fluid particles inside lobes are transported from one lobe to another in each period of perturbation, which indicates that fluid transport follows the lobe dynamics. It follows that fluid particles inside lobes may be transported chaotically by horseshoe maps, since hyperbolic LCSs entangle complicatedly when the integration time is large.
- In contrast, fluid particles inside elliptic LCSs around 1 and 3-periodic points may be transported periodically as a sort of vortex in the Lagrangian description with period 1 and 3 respectively, which is similar to the stable transport of KAM islands in the perturbed Hamiltonian model.

Finally in Chap.5, a novel perturbed Hamiltonian model for Rayleigh-Bénard convection is proposed by qualitatively representing the velocity fields obtained by PIV analysis, since in experiments we have observed some structures different from those in the model proposed by Solomon and Gollub [63] and Camassa and Wiggins [8]. We have gained the following results in Chap.5:

- As in experiments the center of vortices in each cell oscillates side by side widely in the proposed model and velocity around cell boundaries increases when the center of vortices moves close to the boundaries.
- Each term in the Hamiltonian of the proposed model have physical meanings such as the effect of stretching the streamlines in the horizontal direction or the effect of oscillating the center of vortices.
- The proposed model qualitatively elucidates the invariant structures observed in experiments. In particular, figure-eight structures of hyperbolic LCSs and two types of cells with different structures appear in the model. In addition, elliptic LCSs exist around 1 and 3-periodic points similarly in experiments.

6.2 Future plans

As future works, we raise the following topics:

- Clarifying the relationship between KAM tori and elliptic LCSs which are associated with stable fluid transport; We have numerically shown that they may correspond with each other, but more theoretical discussions are necessary to verify it.

- Investigating the figure-eight structures of hyperbolic LCSs in the middle of each cell more in detail; Such structures may correspond to entangled double homoclinic loops. However, we need to seek them further, since all the 1-periodic points in the middle of the cell with larger width in the proposed model are hyperbolic.
- Exploring how the Lagrangian coherent structures and periodic points in perturbed Rayleigh-Bénard convection vary in experiments when Rayleigh number Ra is changed or when a different size of test box is applied; We have investigated the invariant structures of Rayleigh-Bénard convection in one test box with fixed temperature. We may observe some different structures when the experimental setups are changed, which is important for the sake of practical application.
- Analyzing the ε -parameter bifurcations of periodic orbits in the perturbed Hamiltonian model proposed in this thesis; We may obtain ε -parameter bifurcation diagrams that represent the experimental phenomena more accurately. Working on this topic may help exploring the invariant structures of the convection in experiments too.
- Investigating the global structures of fluid transport in three-dimensional perturbed Rayleigh-Bénard convection by developing a three-dimensional dynamical system of the convection or measuring the three-dimensional velocity fields of the convection by experiments or numerical computations of Computational Fluid Dynamics (CFD) models.
- Exploring the global structures of fluid transport in geophysical flow in the atmosphere or ocean; We may predict or control the spread of pollutant in the environment or clarify the structures of meteorological phenomena in the future by such exploration.

References

- [1] Aref, H. [1984], Stirring by chaotic advection, *J. Fluid Mech.*, Vol. 143, pp. 1–21.
- [2] Beron-Vera, F. J., Olascoaga, M. J., Brown, M. G., Koçak, H. and I. Rypina [2010], Invariant-tori-like Lagrangian coherent structures in geophysical flows, *Chaos*, Vol. 20, p. 017514.
- [3] Birkhoff, G. D. [1927], *Dynamical Systems*, Amer. Math. Soc. Colloq. Publ., Vol. 9.
- [4] Blazeovski, D. and G. Haller [2014], Hyperbolic and elliptic transport barriers in three-dimensional unsteady flows, *Physica D*, Vol. 273–274, pp. 46–62.
- [5] Bolton, E. W., Busse, F. H., and R. M. Clever [1986], Oscillatory instabilities of convection rolls at intermediate Prandtl numbers, *J. Fluid Mech.*, Vol. 164, pp. 469–485.
- [6] Busse, F. H. [1972], The oscillatory instability of convection rolls in a low Prandtl number fluid, *J. Fluid Mech.*, Vol. 52, part 1, pp. 97–112.
- [7] Busse, F. H. and J. A. Whitehead [1971], Instabilities of convection rolls in a high Prandtl number fluid, *J. Fluid Mech.*, Vol. 47, part 2, pp. 305–320.
- [8] Camassa, R. and S. Wiggins [1991], Chaotic advection in a Rayleigh-Bénard flow, *Phys. Rev. A*, Vol. 43, No. 2, pp. 774–797.
- [9] Chabreyrie, R., Chandre, C., and N. Aubry [2011], Complete chaotic mixing in an electro-osmotic flow by destabilization of key periodic pathlines, *Phys. Fluids*, Vol. 23, p. 072002.
- [10] Chandrasekhar, S. [1961], *Hydrodynamic and Hydromagnetic Stability*, Oxford University Press.

- [11] Cheng, H., Jiang, H., Chong, K. L., Zhou, Q., Liu, Y., and Z. Lu [2022], The effect of surface roughness on the Lagrangian coherent structures in turbulent Rayleigh-Bénard convection, *Phys. Fluids*, Vol. 34, p. 115134.
- [12] Clever, R. M. and F. H. Busse [1974], Transition to time-dependent convection, *J. Fluid Mech.*, Vol. 65, part 4, pp. 625–645.
- [13] Contreras, P. S., Speetjens, M. F. M., and H. J. H. Clercx [2017], Lagrangian transport in a class of three-dimensional buoyancy-driven flows, *J. Fluid Mech.*, Vol. 832, pp. 5–40.
- [14] Department of Earth System Science and Technology, Kyushu University [2006], *Fluid Dynamics for studying Earth Environment*, Seizando-shoten Publishing (in Japanese).
- [15] Doherty, M. F. and J. M. Ottino [1988], Chaos in deterministic systems: strange attractors, turbulence, and applications in chemical engineering, *Chem. Eng. Sci.*, Vol. 43, No. 2, pp. 139–183.
- [16] Ecke, R. E. and I. G. Kevrekidis [1988], Interactions of resonances and global bifurcations in Rayleigh-Benard convection, *Phys. Lett. A*, Vol. 131, No. 6, pp. 344–352.
- [17] Ecke, R. E., Mainieri, R. and T. S. Sullivan [1991], Universality in quasiperiodic Rayleigh-Bénard convection, *Phys. Rev. A*, Vol. 44, No. 12, pp. 8103–8118.
- [18] Farazmand, M. and G. Haller [2012], Computing Lagrangian coherent structures from their variational theory, *Chaos*, Vol. 22, No. 1, p. 013128.
- [19] Farazmand, M. and G. Haller [2016], Polar rotation angle identifies elliptic islands in unsteady dynamical systems, *Physica D*, Vol. 315, pp. 1–12.
- [20] Flanigan, F. J. [1983], *Complex Variables Harmonic and Analytical Functions*, Dover.
- [21] Gollub, J. P. and S. V. Benson [1980], Many routes to turbulent convection, *J. Fluid. Mech.*, Vol. 100, part 3, pp. 449–470.
- [22] Gollub, J. P. and T. H. Solomon [1989], Complex particle trajectories and transport in stationary and periodic convective flows, *Physica Scripta*, Vol. 40, pp. 430–435.

- [23] Grigoriev, R. [2012], *Transport and Mixing in Laminar Flows: From Microfluidics to Oceanic Currents*, Wiley-VCH.
- [24] Guckenheimer, J. and P. Holmes [1983], *Nonlinear Oscillations, Dynamical Systems, and Bifurcations of Vector Fields*, Springer-Verlag.
- [25] Haller, G. [2001], Distinguished material surfaces and coherent structures in three-dimensional fluid flows, *Physica D*, Vol. 149, pp. 248–277.
- [26] Haller, G. [2002], Lagrangian coherent structures from approximate velocity data, *Physics of Fluids*, Vol. 14, No. 6, pp. 1851–1861.
- [27] Haller, G. [2011], A variational theory of hyperbolic Lagrangian coherent structures, *Physica D*, Vol. 240, No. 7, pp. 574–598.
- [28] Haller, G. [2015], Lagrangian coherent structures, *Annu. Rev. Fluid Mech.*, Vol. 47, No. 1, pp. 137–162.
- [29] Haller, G. and F. J. Beron-Vera [2013], Coherent Lagrangian vortices: the black holes of turbulence, *J. Fluid Mech.*, Vol. 731, R4.
- [30] Haller, G. and F. J. Beron-Vera [2014], Addendum to ‘Coherent Lagrangian vortices: the black holes of turbulence’, *J. Fluid Mech.*, Vol. 755, R3.
- [31] Haller, G. and G. Yuan [2000], Lagrangian coherent structures and mixing in two-dimensional turbulence, *Physica D*, Vol. 147, pp. 352–370.
- [32] Hang, C., Jie, S., YiZhao, Z., Quan, Z., Leong, C. K., YuLu, L., and L. ZhiMing [2022], Lagrangian coherent structures and their heat-transport mechanism in the turbulent Rayleigh-Bénard convection, *Sci. China Tech. Sci.*, Vol. 65, No. 4, pp. 966–976.
- [33] Hidaka, Y., Hashiguchi, M., Oikawa, N., and S. Kai [2015], Lagrangian chaos and particle diffusion in electroconvection of planar nematic liquid crystals, *Phys. Rev. E*, Vol. 92, No. 3, p. 032909.
- [34] Inoue, Y., [2004], Engineering analysis and evaluation of fluid mixing mechanisms, *RIMS Kokyuroku* No. 1368. pp. 160–167 (in Japanese).
- [35] Inoue, Y. and Y. Hirata [1998], Numerical analysis of chaotic mixing in plane cellular flow I: Formation mechanisms of initial mixing pattern and fine mixing pattern, *Kagaku Kougaku Ronbunshu*, Vol. 24, No. 2, pp. 294–302 (in Japanese).

- [36] Inoue, Y. and Y. Hirata [2000], Numerical analysis of chaotic mixing in plane cellular flow II: Mixedness and final mixing pattern, *Kagaku Kougaku Ronbunshu*, Vol. 26, No.1, pp. 31–39 (in Japanese).
- [37] Inoue, Y., Kawazoe, H., Yamada, M. and Y. Hirata [2014], Fluid mixing and golden ratio condition, *Kagaku Kougaku Ronbunshu*, Vol. 40, No. 6, pp. 449–461 (in Japanese).
- [38] Kimura, R. [1983], *Introduction to Geophysical Fluid Dynamics -The mechanism of flow in the atmosphere and ocean- (The promenade of meteorology* Vol. 13), Tokyodo shuppan (in Japanese).
- [39] Krishnamurti, R. [1970], On the transition to turbulent convection. Part 1. The transition from two- to three-dimensional flow, *J. Fluid Mech.*, Vol. 42, Part 2, pp. 295–307.
- [40] Krishnamurti, R. [1970], On the transition to turbulent convection. Part 2. The transition to time-dependent flow, *J. Fluid Mech.*, Vol. 42, Part 2, pp. 309–320.
- [41] Kuznetsov, Y. A. [2004], *Elements of Applied Bifurcation Theory*. Third edition, Springer-Verlag.
- [42] Lekien, F., Shadden, S. C., and J. E. Marsden [2007], Lagrangian coherent structures in n -dimensional systems, *J. Math. Phys.*, Vol. 48, p. 065404.
- [43] Lichtenberg, A. J. and M. A. Lieberman [1991], *Regular and Chaotic Dynamics*, 2nd edition, Applied Mathematical Science, Vol. 38, Springer-Verlag.
- [44] Ma, T. and S. Wang [2004], Dynamic bifurcation and stability in the Rayleigh-Bénard convection, *Comm. Math. Sci.*, Vol. 2, No. 2, pp. 159–183.
- [45] Ma, T. and S. Wang [2007], Rayleigh Benard convection: dynamics and structures in the physical space, *Comm. Math. Sci.*, Vol. 5, No. 3, pp. 553–574.
- [46] Malhotra, N., Mezić, I., and S. Wiggins [1998], Patchiness: A new diagnostic for Lagrangian trajectory analysis in time-dependent fluid flows, *Int. J. Bifurcation and Chaos*, Vol. 8, No. 6, pp. 1053–1093.

- [47] Matveev, L. V. [2016], Impurity transport in developed Rayleigh-Bénard convection, *Int. J. Heat and Mass Transfer*, Vol. 95, pp. 15–21.
- [48] Mukutmoni, D. and K. T. Yang [1993], Rayleigh-Bénard convection in a small aspect ratio enclosure: Part I–bifurcation to oscillatory convection, *J. Heat Transfer*, Vol. 115, No. 2, pp. 360–366.
- [49] Mukutmoni, D. and K. T. Yang [1993], Rayleigh-Bénard convection in a small aspect ratio enclosure: Part II–bifurcation to chaos, *J. Heat Transfer*, Vol. 115, No. 2, pp. 367–376.
- [50] Net, M. and J. S. Umbriá [2017], Periodic orbits in tall laterally heated rectangular cavities, *Phys. Rev. E*, Vol. 95, pp. 023102.
- [51] Onu, K. and G. Haller [2015], *LCS Tool: A computational platform for Lagrangian coherent structures*, *J. Comp. Sci.*, Vol. 7, pp. 26–36.
- [52] Oteski, L., Duguet, Y., and L. R. Pastur [2014], Lagrangian chaos in confined two-dimensional oscillatory convection, *J. Fluid Mech.*, Vol. 759, pp. 489–519.
- [53] Ottino, J. M. [1989], *The Kinematics of Mixing: Stretching, Chaos, and Transport*, Cambridge University Press.
- [54] Ouchi, K. and H. Mori [1992], Anomalous diffusion and mixing in an oscillating Rayleigh-Bénard flow, *Prog. Theor. Phys.*, Vol. 88, No. 3, pp. 467–484.
- [55] Ouchi, K., Mori, N., Horita, T., and H. Mori [1991], Advective diffusion of particles in Rayleigh-Bénard convection, *Prog. Theor. Phys.*, Vol. 85, No. 4, pp. 687–691.
- [56] Paul, S., Wahi, P., and M. K. Verma [2011], Bifurcations and chaos in large-Prandtl number Rayleigh-Bénard convection, *Int. J. Non-Linear Mech.*, Vol. 46, No. 5, pp. 772–781.
- [57] Rom-Kedar, V. and S. Wiggins [1990], Transport in Two-dimensional Maps, *Arch. Rational Mech. and Analysis*, Vol. 109, No. 3, pp. 239–298.
- [58] Schneide, C., Pandey, A., Padberg-Gehle, K., and J. Schumacher [2018], Probing turbulent superstructures in Rayleigh-Bénard convection by Lagrangian trajectory clusters, *Phys. Rev. Fluids*, Vol. 3, No. 11, p. 113501.

- [59] Schneide, C., Vieweg, P. P., Schumacher, J., and K. Padberg-Gehle [2022], Evolutionary clustering of Lagrangian trajectories in turbulent Rayleigh-Bénard convection flows, *Chaos*, Vol. 32, p. 013123.
- [60] Shadden, S. C., Lekien, F. and J. E. Marsden [2005], Definition and properties of Lagrangian coherent structures from finite-time Lyapunov exponents in two-dimensional aperiodic flows, *Physica D*, Vol. 212, pp. 271–304.
- [61] Simó, C., Puigjaner, D., Herrero, J., and F. Giralt [2010], Dynamics of particle trajectories in a Rayleigh-Bénard problem, *Comm. Nonlinear Sci. and Num. Simul.*, Vol. 15, No. 1, pp. 24–39.
- [62] Solomon, T. H. and J. P. Gollub [1988], Passive transport in steady Rayleigh-Bénard convection, *Phys. Fluids*, Vol. 31, pp. 1372–1379.
- [63] Solomon, T. H. and J. P. Gollub [1988], Chaotic particle transport in time-dependent Rayleigh-Bénard convection, *Phys. Rev. A*, Vol. 38, No. 12, pp. 6280–6286.
- [64] Solomon, T. H. and I. Mezić [2003], Uniform resonant chaotic mixing in fluid flows, *Nature*, Vol. 425, pp. 376–380.
- [65] Solomon, T. H., Tomas, S. and J. L. Warner [1996], Role of lobes in chaotic mixing of miscible and immiscible impurities, *Phys. Rev. Lett.*, Vol. 77, No. 13, pp. 2682–2685.
- [66] Solomon, T. H., Tomas, S. and J. L. Warner [1998], Chaotic mixing of immiscible impurities in a two-dimensional flow, *Phys. Fluids*, Vol. 10, No. 2, pp. 342–350.
- [67] The Visualization Society of Japan [2018], *PIV Handbook*, 2nd edition, Morikita Publishing (in Japanese).
- [68] Tsumoto, K., Ueta, T., Yoshinaga, T. and H. Kawakami [2012], Bifurcation analyses of nonlinear dynamical systems: From theory to numerical computations, *Nonlinear Theory and Its App.*, *IEICE*, Vol. 3, No. 4, pp. 458–476.
- [69] Umbriá, J. S. and M. Net [2019], Stationary flows and periodic dynamics of binary mixtures in tall laterally heated slots, *Computational Modelling of Bifurcations and Instabilities in Fluid Dynamics* edited by A. Gelfgat, Springer International Publishing AG.

- [70] Watanabe, M., Kitamura, Y., Hatta, N., and H. Yoshimura [2020], Experimental analysis of Lagrangian coherent structures and chaotic mixing in Rayleigh-Benard convection, *Proc. ASME 2020 Fluids Engineering Division Summer Meeting*, No. 20116, Orlando, USA (Online).
- [71] Watanabe, M. and H. Yoshimura [2021], Experimental investigation of Lagrangian coherent structures and lobe dynamics in perturbed Rayleigh-Benard convection, *Proc. ASME 2021 Fluids Engineering Division Summer Meeting*, No. 64945, Online.
- [72] Watanabe, M. and H. Yoshimura [2021], Experimental observations of Lagrangian coherent structures and fluid transports in perturbed Rayleigh-Bénard Convection, *Proc. Third IFAC Conference on Modelling, Identification and Control of Nonlinear Systems*, Online, pp. 473–478.
- [73] Watanabe, M. and H. Yoshimura [2022], Experimental observation of Lagrangian coherent structures in perturbed Rayleigh-Benard convection, *J. Fluids Eng.*, Vol. 144, No. 4, p. 040902.
- [74] Watanabe, M. and H. Yoshimura [2023], Resonance, symmetry, and bifurcation of periodic orbits in perturbed Rayleigh-Bénard convection, *Nonlinearity*, Vol. 36, No. 2, pp. 955–999.
- [75] Wiggins, S. [1990], *Introduction to Applied Nonlinear Dynamical Systems and Chaos*, Vol. 2, Springer-Verlag.
- [76] Wiggins, S. [1992], *Chaotic Transport in Dynamical Systems*, Interdisciplinary Applied Mathematics, Vol. 2, Springer-Verlag.
- [77] Wiggins, S. and J. M. Ottino [2004], Foundations of chaotic mixing, *Phil. Trans. R. Soc. Lond. A*, Vol. 362, pp. 937–970.
- [78] Willis, G. E. and J. W. Deardorff [1970], The oscillatory motions of Rayleigh convection, *J. Fluid Mech.*, Vol. 44, part 4, pp. 661–672.
- [79] Yamanaka, K., Narumi, T., Hashiguchi, M., Okabe, H., Hara, K., and Y. Hidaka [2018], Time-dependent diffusion coefficients for chaotic advection due to fluctuations of convective rolls, *Fluids*, Vol. 3, No. 4, p. 99.

Acknowledgments

First of all, the author would like to express his sincere gratitude to Professor Hiroaki Yoshimura for his valuable suggestions and continuous support as well as his thoughtful mentorship. The author have learned not only academic knowledge from Professor Yoshimura but also the attitude to study as a researcher. To be honest, it was a big challenge for the author to decide to join his applied mathematical laboratory in the third year of university in 2015, but now the author truly believe that it was the best decision. The author would not forget the fruitful days spent in his laboratory for eight years. The author highly appreciate Professor Yutaka Ohta, Professor Kiyoshi Saito, and Professor Tomohiro Yanao for reviewing this thesis. The author is partially supported by Waseda University (SR 2022C-092 and SR 2022E-016), the MEXT "Top Global University Project", and Sustainable Energy & Environmental Society Open Innovation Research Organization (SEES). The author's supervisor Professor Yoshimura is partially supported by JSPS Grant-in-Aid for Scientific Research (22K03443), JST CREST (JPMJCR1914), Waseda University (SR 2022C-423), the MEXT "Top Global University Project", SEES, and the Organization for University Research Initiatives (Evolution and application of energy conversion theory in collaboration with modern mathematics). The author would like to express his great appreciation to Mr. Takahiro Ushioku in Professor Yoshimura's laboratory for interesting discussions and big supports as well as pleasant memories. The author appreciate all the students in the laboratory. Especially, the author is grateful to the following students in the same research group for useful discussions and technical assistance with experiments: Mr. Tomohiro Miyamoto, Mr. Yusuke Kitamura, Mr. Naoki Hatta, Mr. Ryousuke Kamakura, Mr. Masashi Yamamoto, Mr. Yudai Mouri, Ms. Rena Karube, Mr. Yuta Haga, Mr. Yuta Nakahara, and Mr. Yutaro Otsuka. Finally, the author sincerely appreciate to his family for big warm supports.

Appendix A

Model of Rayleigh-Bénard convection

A.1 Hamiltonian system of steady Rayleigh-Bénard convection

In this section we show how the Hamiltonian system of two-dimensional steady Rayleigh-Bénard convection is derived from the fundamental governing equations of Boussinesq fluid by following Kimura [38]; see also Chandrasekhar [10].

Fundamental governing equations. Consider a layer of Boussinesq fluid with heated bottom and cooled top planes. We assume that the flow is two-dimensional and that there is no viscous force on the lower and upper boundaries between the fluid and planes. Let us denote pressure p , temperature T , and density ρ of the fluid at point $(x, z) \in \mathbb{R} \times [0, 1]$ at time t as

$$\begin{aligned} p(x, z, t) &= p_m + p_0(z) + p'(x, z, t), \\ \rho(x, z, t) &= \rho_m + \rho_0(z) + \rho'(x, z, t), \\ T(x, z, t) &= T_m + T_0(z) + T'(x, z, t) \end{aligned}$$

respectively, where ρ_m, T_m, p_m are constant numbers. Notice that the variables with primes ' are the perturbations added to the variables for hydrostatic equilibrium. Then, the fundamental governing equations of the fluid can be written as follows:

$$u = -\frac{\partial \psi}{\partial z}, \quad w = \frac{\partial \psi}{\partial x}, \quad (\text{A.1.1})$$

$$\frac{\partial u}{\partial t} + u \frac{\partial u}{\partial x} + w \frac{\partial u}{\partial z} = -\frac{1}{\rho_m} \frac{\partial p'}{\partial x} + \frac{\mu}{\rho_m} \nabla^2 u, \quad (\text{A.1.2})$$

$$\frac{\partial w}{\partial t} + u \frac{\partial w}{\partial x} + w \frac{\partial w}{\partial z} = -\frac{1}{\rho_m} \frac{\partial p'}{\partial z} + \alpha g T' + \frac{\mu}{\rho_m} \nabla^2 w, \quad (\text{A.1.3})$$

$$\frac{\partial T'}{\partial t} + u \frac{\partial T'}{\partial x} + w \frac{\partial T'}{\partial z} - w \Gamma = \kappa \nabla^2 T', \quad (\text{A.1.4})$$

where $u(x, z, t)$ and $w(x, z, t)$ indicate the velocity in x and z direction. (A.1.1) corresponds to the equation of continuity, where we introduce a stream function $\psi(x, z)$. (A.1.2) and (A.1.3) are the Navier-Stokes equations, and (A.1.4) is the thermodynamic equation. In the above we define the coefficient of cubic expansion and the decreasing rate of temperature as $\alpha = 1/T_m$ and $\Gamma = -\partial T_0/\partial z > 0$ respectively.

Boundary conditions. Next, we consider the boundary conditions. Since the velocity in z direction on the upper and lower boundaries are zero, let

$$\left. \frac{\partial \psi}{\partial x} \right|_{z=0} = \left. \frac{\partial \psi}{\partial x} \right|_{z=d} = 0. \quad (\text{A.1.5})$$

In addition, now that there is no viscous force on the lower and upper boundaries, let

$$\mu \left. \frac{\partial u}{\partial z} \right|_{z=0} = \mu \left. \frac{\partial u}{\partial z} \right|_{z=d} = 0,$$

where μ indicates the viscosity efficient. These conditions can be rewritten as

$$\left. \frac{\partial^2 \psi}{\partial z^2} \right|_{z=0} = \left. \frac{\partial^2 \psi}{\partial z^2} \right|_{z=d} = 0 \quad (\text{A.1.6})$$

by using (A.1.1). Further, since the temperature on the upper and lower boundaries is uniform, let

$$\left. \frac{\partial T'}{\partial x} \right|_{z=0} = \left. \frac{\partial T'}{\partial x} \right|_{z=d} = 0. \quad (\text{A.1.7})$$

Linear stability analysis. Let us consider the stable solution of partial differential equations (A.1.1), (A.1.2), (A.1.3), (A.1.4) with boundary conditions (A.1.5), (A.1.6), (A.1.7). To do this we consider a perturbation that satisfies the equations and boundary conditions and check whether the perturbation remains stably. Since the perturbation is small, we can ignore the nonlinear terms. Thus, the fundamental governing equations of the fluid can be rewritten as follows:

$$u = -\frac{\partial \psi}{\partial z}, \quad w = \frac{\partial \psi}{\partial x}, \quad (\text{A.1.8})$$

$$\frac{\partial u}{\partial t} = -\frac{1}{\rho_m} \frac{\partial p'}{\partial x} + \frac{\mu}{\rho_m} \nabla^2 u, \quad (\text{A.1.9})$$

$$\frac{\partial w}{\partial t} = -\frac{1}{\rho_m} \frac{\partial p'}{\partial z} + \alpha g T' + \frac{\mu}{\rho_m} \nabla^2 w, \quad (\text{A.1.10})$$

$$\frac{\partial T'}{\partial t} - w\Gamma = \kappa \nabla^2 T'. \quad (\text{A.1.11})$$

By subtracting the partial derivative of (A.1.10) with respect to x from the partial derivative of (A.1.9) with respect to z , and rearranging the equation by using (A.1.8), we obtain

$$\frac{\partial}{\partial t} \nabla^2 \psi = \alpha g \frac{\partial T'}{\partial x} + \nu \nabla^2 \nabla^2 \psi,$$

where the kinematic viscosity coefficient is defined as $\nu = \mu/\rho_m$. Then, we deform the equation as

$$\alpha g \frac{\partial T'}{\partial x} = \left(\frac{\partial}{\partial t} - \nu \nabla^2 \right) \nabla^2 \psi. \quad (\text{A.1.12})$$

Next, we partially differentiate (A.1.11) with respect to x and rearrange it as

$$\left(\frac{\partial}{\partial t} - \kappa \nabla^2 \right) \alpha g \frac{\partial T'}{\partial x} = \alpha g \Gamma \frac{\partial w}{\partial x}. \quad (\text{A.1.13})$$

Then, we obtain

$$\left(\frac{\partial}{\partial t} - \kappa \nabla^2 \right) \left(\frac{\partial}{\partial t} - \nu \nabla^2 \right) \nabla^2 \psi = \alpha g \Gamma \frac{\partial^2 \psi}{\partial x^2} \quad (\text{A.1.14})$$

by substituting (A.1.12) into (A.1.13) and rearranging the equation by using (A.1.8).

Transformation to non-dimensional equations. Next, we describe the equations with non-dimensional variables. To do this we define some non-dimensional variables as

$$\begin{aligned} t_* &= \frac{\nu}{d^2} t, \\ x_* &= \frac{1}{d} x, \\ z_* &= \frac{1}{d} z, \\ \psi_* &= \frac{1}{\nu} \psi, \\ \nabla_*^2 &= d^2 \nabla^2. \end{aligned}$$

Then, (A.1.14) can be written as

$$\left(\frac{\partial}{\partial t_*} - \frac{1}{Pr} \nabla_*^2 \right) \left(\frac{\partial}{\partial t_*} - \nabla_*^2 \right) \nabla_*^2 \psi_* = Gr \frac{\partial^2 \psi_*}{\partial x_*^2}, \quad (\text{A.1.15})$$

where Prandtl number Pr and Grashof number Gr is defined as

$$Pr = \frac{\nu}{\kappa},$$

$$Gr = \frac{\alpha g \Gamma d^4}{\nu^2}.$$

In addition, the boundary conditions (A.1.5) and (A.1.6) can be expressed as

$$\left. \frac{\partial \psi_*}{\partial x_*} \right|_{z_*=0} = \left. \frac{\partial \psi_*}{\partial x_*} \right|_{z_*=1} = 0, \quad (\text{A.1.16})$$

$$\left. \frac{\partial^2 \psi_*}{\partial z_*^2} \right|_{z_*=0} = \left. \frac{\partial^2 \psi_*}{\partial z_*^2} \right|_{z_*=1} = 0. \quad (\text{A.1.17})$$

Further, the boundary condition (A.1.7) becomes

$$\left(\frac{\partial}{\partial t_*} - \nabla_*^2 \right) \nabla_*^2 \psi_* \Big|_{z_*=0} = \left(\frac{\partial}{\partial t_*} - \nabla_*^2 \right) \nabla_*^2 \psi_* \Big|_{z_*=1} = 0 \quad (\text{A.1.18})$$

by using (A.1.12).

Steady solution of governing equations. Now, let us consider the steady solution of (A.1.15) with boundary conditions (A.1.16), (A.1.17), (A.1.18). It is common that the patterns of thermal convection repeats in horizontal direction. Thus, let us assume the stream function of steady Rayleigh-Bénard convection as

$$\psi(x, z) = \Psi(z) \sin(kx), \quad (\text{A.1.19})$$

where $k > 0$ is the wave number of the pattern in x direction. Note that we omit the asterisk $*$ in (A.1.19) and hereafter. Then, by substituting (A.1.19) into (A.1.15), we obtain

$$\left(\frac{\partial^2}{\partial z^2} - k^2 \right)^3 \Psi(z) \sin(kx) = -k^2 Ra \Psi(z) \sin(kx).$$

Since the above equation needs to hold for any arbitrary x , it follows that

$$\left(\frac{d^2}{dz^2} - k^2 \right)^3 \Psi(z) = -k^2 Ra \Psi(z), \quad (\text{A.1.20})$$

where Rayleigh number Ra is defined as

$$Ra = Gr Pr = \frac{\alpha g \Gamma d^4}{\nu \kappa}.$$

Next, we substitute (A.1.19) into the boundary conditions (A.1.16), (A.1.17), and (A.1.18). Then, we obtain

$$\begin{aligned}
k\Psi(0)\cos(kx) &= k\Psi(1)\cos(kx) = 0, \\
\frac{\partial^2\Psi(0)}{\partial z^2}\sin(kx) &= \frac{\partial^2\Psi(1)}{\partial z^2}\sin(kx) = 0, \\
\left(k^4\Psi(0) - 2k^2\frac{\partial^2\Psi(0)}{\partial z^2} + \frac{\partial^4\Psi(0)}{\partial z^4}\right)\sin(kx) \\
&= \left(k^4\Psi(1) - 2k^2\frac{\partial^2\Psi(1)}{\partial z^2} + \frac{\partial^4\Psi(1)}{\partial z^4}\right)\sin(kx) = 0.
\end{aligned}$$

Since the above equations need to hold for any arbitrary x , it follows that

$$\begin{aligned}
\Psi(0) &= \Psi(1) = 0, \\
\frac{\partial^2\Psi(0)}{\partial z^2} &= \frac{\partial^2\Psi(1)}{\partial z^2} = 0, \\
\frac{\partial^4\Psi(0)}{\partial z^4} &= \frac{\partial^4\Psi(1)}{\partial z^4} = 0.
\end{aligned}$$

Thus, let us define

$$\Psi(z) = \Psi_0 \sin(\pi z), \quad (\text{A.1.21})$$

where Ψ_0 is a constant number.

Finally, we consider the condition for which (A.1.20) holds. By using (A.1.21) and (A.1.19), (A.1.20) can be deformed as

$$\left(Ra - \frac{(k^2 + \pi^2)^3}{k^2}\right)\sin(\pi z) = 0. \quad (\text{A.1.22})$$

It is necessary that

$$Ra = \frac{(k^2 + \pi^2)^3}{k^2} \quad (\text{A.1.23})$$

so that (A.1.22) holds for any arbitrary z . Therefore, if we choose some k that satisfies (A.1.23),

$$\psi(x, z) = \Psi_0 \sin(\pi z) \sin(kx)$$

is one of the stable solutions of (A.1.15) with boundary conditions (A.1.16), (A.1.17), (A.1.18). Hence, by replacing $\Psi_0 = A/k$, the stream function of steady Rayleigh-Bénard convection is given by

$$\psi(x, z) = \frac{A}{k} \sin(\pi z) \sin(kx),$$

and its velocity fields is given by

$$\begin{aligned} u(x, z) &= -\frac{\partial \psi}{\partial z} = -\frac{A\pi}{k} \cos(\pi z) \sin(kx), \\ w(x, z) &= \frac{\partial \psi}{\partial x} = A \sin(\pi z) \cos(kx), \end{aligned}$$

where $x \in \mathbb{R}, z \in [0, 1]$. Here, k is the wave number of the pattern in x direction, and A is the maximum velocity in z direction.

Appendix B

Experimental methods

B.1 Particle Image Velocimetry (PIV)

In this section we briefly describe the basic principles of Particle Image Velocimetry (PIV). PIV is an experimental method to measure the global velocity fields of flow by using optical devices as well as numerical computation. Here, we only introduce PIV for two-dimensional velocity fields on two-dimensional space, which is the most common one, but we note that there is some other PIV for three-dimensional velocity fields or space.

As is shown in Fig.B.1.1, small particles, for example nylon particles for liquid flow or oil particles for gas flow, are mixed in the fluid as tracer particles. Then, a laser sheet is irradiated to the flow and the transport of illuminated tracer particles are recorded by a camera. Fig.B.1.2 depicts the schematic illustration of the recorded frames at $t = t_n$ and $t = t_n + \Delta t$. We assume that tracer particles are transported exactly with fluid particles and numerically detect the displacement $\Delta \mathbf{x}$ of a local region in time interval Δt by comparing the two frames. In particular, this method is called image correlation method. On the other hand, there is another method that detect the displacement of one tracer particle. This is sometimes called Particle Tracking Velocimetry (PTV) to distinguish with the image correlation method. Then, the local velocity vector \mathbf{v} is obtained by

$$\mathbf{v} = \frac{\Delta \mathbf{x}}{\Delta t}.$$

The global velocity fields are gained by computing the velocity at each point in the above method. Hence, it is important that tracer particles are transported with fluid particles as exactly as possible. Thus, tracer particles with almost the same density of the fluid are often chosen.

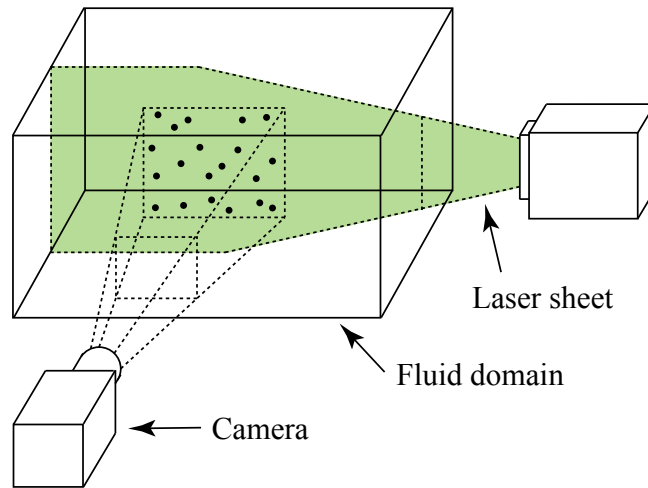


Figure B.1.1: Experimental setup for PIV

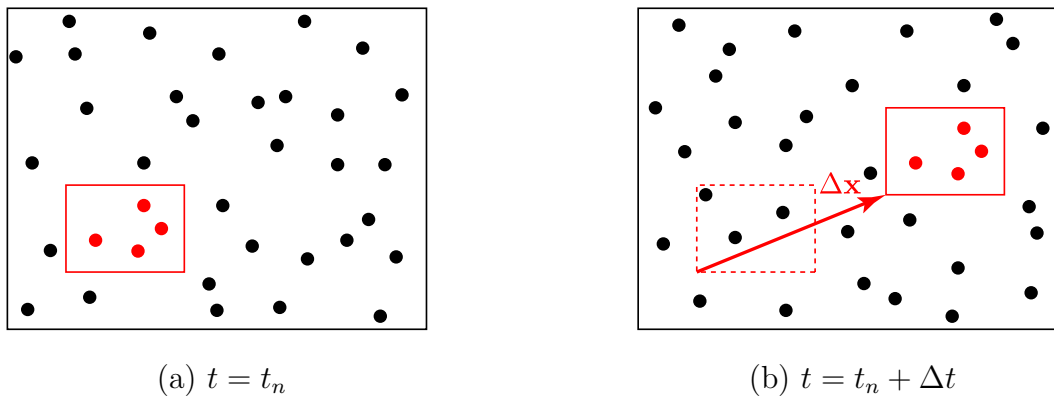


Figure B.1.2: Recorded frames

List of research achievements for application of Doctor of Engineering, Waseda University

Full Name : 渡辺 昌仁

seal or signature

Date Submitted(yyyy/mm/dd): 2023/1/31

種別 (By Type)	題名、発表・発行掲載誌名、発表・発行年月、連名者（申請者含む） (theme, journal name, date & year of publication, name of authors inc. yourself)
論文(査読付)	<p>○ [1] <u>M. Watanabe</u> and H. Yoshimura, "Resonance, symmetry, and bifurcation of periodic orbits in perturbed Rayleigh-Bénard convection", Nonlinearity, Vol. 36, No. 2, pp. 955-999, 2023.</p> <p>○ [2] <u>M. Watanabe</u> and H. Yoshimura, "Experimental Observation of Lagrangian Coherent Structures in Perturbed Rayleigh-Bénard Convection", Journal of Fluids Engineering, Vol. 144, No.4, 040902, 2022. (ASME 2021 Fluids Engineering Division Summer Meeting, Flow Visualization Competitionよりtransferした論文.)</p>
国際会議論文 (査読付)	<p>○ [3] <u>M. Watanabe</u> and H. Yoshimura, "Experimental Observations of Lagrangian Coherent Structures and Fluid Transports in Perturbed Rayleigh-Bénard Convection", Proc. Third IFAC Conference on Modelling, Identification and Control of Nonlinear Systems, pp. 473-478, Online, September, 2021.</p> <p>○ [4] <u>M. Watanabe</u> and H. Yoshimura, "Experimental Investigation of Lagrangian Coherent Structures and Lobe Dynamics in Perturbed Rayleigh-Bénard Convection", Proc. ASME 2021 Fluids Engineering Division Summer Meeting, No. 64945, Online, August, 2021.</p> <p>○ [5] <u>M. Watanabe</u>, Y. Kitamura, N. Hatta, and H. Yoshimura, "Experimental Analysis of Lagrangian Coherent Structures and Chaotic Mixing in Rayleigh-Bénard Convection", Proc. ASME 2020 Fluids Engineering Division Summer Meeting, No. 20116, Orlando, USA (Online), July, 2020.</p>
国際学会発表	<p>[6] <u>M. Watanabe</u> and H. Yoshimura, "Bifurcations of Periodic Orbits in Perturbed Rayleigh-Bénard Convection", Bifurcation Governed by Partial Differential Equations, Waseda University, Tokyo, Japan, December, 2022.</p> <p>[7] <u>M. Watanabe</u> and H. Yoshimura, "Lagrangian Coherent Structures in Rayleigh-Bénard Convection with Perturbations", International Workshop on Multiphase Flows: Analysis, Modelling and Numerics, Waseda University, Tokyo, Japan (Online), December, 2020.</p> <p>[8] <u>M. Watanabe</u> and H. Yoshimura, "Chaotic Mixing in Two-dimensional Rayleigh-Bénard Convection with Periodic Perturbations", Fourth International Conference on Recent Advances in Nonlinear Mechanics, pp. 49-52, Lodz, Poland, May, 2019. (査読付)</p> <p>[9] <u>M. Watanabe</u>, T. Miyamoto, and H. Yoshimura, "Mixing and Lagrangian Coherent Structures in Two-dimensional Rayleigh-Bénard Convection with Periodic Perturbations", 2018 SIAM Conference on Nonlinear Waves and Coherent Structures, CP3, Anaheim, USA, June, 2018.</p>
国内学会発表	<p>[10] <u>渡辺昌仁</u>, 吉村浩明, "摂動を受けるレイリー・ベナール対流の実験的観測とカオス的流体輸送の解析", 日本機械学会 機械力学・計測制御部門 Dynamics and Design Conference 2021, No. 117, 東京大学 (オンライン), 2021年9月.</p> <p>[11] <u>渡辺昌仁</u>, 吉村浩明, "摂動を受けるレイリー・ベナール対流に現れるラグランジュ・コヒーレント構造と流体輸送の実験的解析", 日本応用数学会 2021年度年会, pp. 232-233, 芝浦工業大学 (オンライン), 2021年9月.</p> <p>[12] <u>渡辺昌仁</u>, 喜多村友祐, 八田尚樹, 鎌倉良介, 吉村浩明, "摂動を受けるレイリー・ベナール対流に現れるラグランジュ・コヒーレント構造とローブダイナミクス", 日本応用数学会 2020年度年会, pp. 359-360, 愛媛大学 (オンライン), 2020年9月.</p> <p>[13] <u>渡辺昌仁</u>, 喜多村友祐, 八田尚樹, 鎌倉良介, 吉村浩明, "レイリー・ベナール対流に現れるカオス的な流体輸送とラグランジュ・コヒーレント構造に関する実験的解析", 日本機械学会 2020年度年次大会, S05307, 名古屋大学 (オンライン), 2020年9月.</p> <p>[14] <u>渡辺昌仁</u>, 吉村浩明, "摂動を受けるレイリー・ベナール対流におけるカオスの混合と分岐現象", 日本機械学会関東支部 第26期総会・講演会, 17G13, 早稲田大学, 2020年3月.</p> <p>[15] <u>渡辺昌仁</u>, 吉村浩明, "摂動を受けるレイリー・ベナール対流に現れるカオスの混合と分岐構造", 日本応用数学会 2019年度年会, pp. 198-199, 東京大学, 2019年9月.</p>

List of research achievements for application of Doctor of Engineering, Waseda University

Full Name : 渡辺 昌仁

seal or signature

Date Submitted(yyyy/mm/dd):

2023/1/31

種別 (By Type)	題名、発表・発行掲載誌名、発表・発行年月、連名者（申請者含む） (theme, journal name, date & year of publication, name of authors inc. yourself)
受賞	<p>[16] 渡辺昌仁, 吉村浩明, "摂動を受けるレイリー・ベナール対流に現れるカオスの混合と分岐現象", 日本機械学会 機械力学・計測制御部門 Dynamics and Design Conference 2019, No. 154, 九州大学, 2019年8月.</p> <p>[17] 渡辺昌仁, 吉村浩明, "レイリー・ベナール対流におけるラグランジュ的な流体輸送の解析", 日本応用数理学会 2018年度年会, pp. 87-88, 名古屋大学, 2018年9月.</p> <p>[18] 渡辺昌仁, 宮本知紘, 吉村浩明, "レイリー・ベナール対流における流体混合の大域的構造と混合率", 日本応用数理学会 2017年度年会, pp. 165-166, 武蔵野大学, 2017年9月.</p> <p>[19] 宮本知紘, 渡辺昌仁, 吉村浩明, "レイリー・ベナール対流に現れるラグランジュ・コヒーレント構造とカオスの混合に関する数値解析", 日本応用数理学会 2016年度年会, No. 24, 北九州国際会議場, 2016年9月. (ポスター発表)</p> <p>[20] 早稲田大学 理工学術院総合研究所, 若手研究者奨励賞, 2022年3月.</p> <p>[21] 早稲田大学 理工学術院総合研究所 若手研究者育成・支援事業 第11期アーリーバードプログラム, 成果報告会 個人発表 優秀賞, 2022年3月.</p> <p>[22] 伊波伽奈子, 鈴木貴大, 高桑聖仁, 張天逸, 渡辺昌仁, 早稲田大学 理工学術院総合研究所 若手研究者育成・支援事業 第11期アーリーバードプログラム, 成果報告会 共同研究計画発表 最優秀賞, 2022年3月.</p> <p>[23] M. Watanabe and H. Yoshimura, ASME 2021 Fluids Engineering Division Summer Meeting, Flow Visualization Competition (Images Category), 2nd prize, 2021年8月.</p> <p>[24] ASME Fluids Engineering Division 2020 Graduate Student Scholarship Award, 2021年3月.</p> <p>[25] 文部科学省 次世代研究者育成プログラム HIRAKU 未来博士 3分間コンペティション2020, JSW日本製鋼所動画賞, 2020年11月.</p> <p>[26] 日本機械学会 畠山賞, 2017年3月.</p> <p>[27] 早稲田大学 基幹理工学部賞 最優秀賞, 2017年3月.</p> <p>[28] 早稲田大学 機械科学航空学術賞, 2017年3月.</p> <p>[29] 宮本知紘, 渡辺昌仁, 吉村浩明, 日本応用数理学会2016年度年会 優秀ポスター賞, 2016年9月.</p>